OPTICAL AND ELECTRICAL CHARACTERIZATION OF SEEDED PHYSICAL VAPOR TRANSPORT ZINC SELENIDE

By

HECTOR LUIS COTAL

Bachelor of Science
Oklahoma State University
Stillwater, Oklahoma
1986

Master of Science
Oklahoma State University
Stillwater, Oklahoma
1990

Submitted to the Faculty of the
Graduate College of the
Oklahoma State University
in partial fulfillment of
the requirements for
the Degree of
DOCTOR OF PHILOSOPHY
July, 1993

OKLAHOMA STATE UNIVERSIT

OPTICAL AND ELECTRICAL CHARACTERIZATION

OF SEEDED PHYSICAL VAPOR TRANSPORT

ZINC SELENIDE

Thesis Approved:

Thesis Advisor

Dean of the Graduate College

ACKNOWLEDGMENTS

It is difficult to thank Dr. McKeever because he has played a vital role in molding me to what I am today as far as being a researcher is concerned. However, I would first like to express my sincere gratitude to him for his professional guidance, attention, patience and understanding during my research career. I also would like to thank him for allowing me a chance to work in his labotatory and for the freedom and support to try new research. Much appreciation is conveyed to my thesis committee—Dr. Paul Westhaus, Dr. James Wicksted, Dr. Edward Knobbe and Dr. Robert Hauenstein—for making my thesis defense a memorable experience.

Many thanks are in order for Dr. Joel Martin for loaning me the necessary equipment which made the uniaxial stress and FTIR (results and analysis not included in the thesis) measurements possible, and for the many helpful discussions we had. I also would like to thank Jeff Maxsom (who is currently an outstanding undergraduate student) for his help with the excitation power- and stress-dependent photoluminescence measurements. Furthermore, I am grateful to Dr. Jack Vitek for giving me an opportunity to enter the graduate program and to all the people at Oklahoma State University who helped me during the course of my graduate work.

I would like to give a heartfelt thanks to my wife, Sharon, for typing most of this thesis and for caring for our two sons while I completed the research for this work. Without her continued encouragement and support throughout my graduate studies, my attainment of this degree would not have been possible. A special debt is owed to her for enduring my long hours of study with understanding and patience.

I would also like to thank my wife's parents, Grant and Theresa Isbell, for their support (both verbal and financial) during my college career. Theresa was always willing to babysit the boys so that my wife could help me or so that we could go out for a much-needed break.

Finally, I would like to thank the Defense Advance Research Poject Agency and the National Science Foundation for providing us with the funding, and to all other agencies whose contributions helped make this work a success.

TABLE OF CONTENTS

Chapter		Page
I.	INTRODUCTION	1
	Historical Note and Progress	1
	Background Information	4
	Crystal Structure	9
	Band Structure	12
	Scope of this Study	14
II.	PHOTOLUMINESCENCE AND OPTICAL ABSORPTION	15
	Introduction	15
	Experimental Details	16
	Sample Preparation	16
	Photoluminescence, Thermal Quenching and Excitation Power Dependence Experimental Setup	17
	Uniaxial Stress Experimental Setup	20
	Cryogenics and Stress Apparatus	20
	Optics Layout	22
	Optical Absorption Setup	23
	Experimental Results	25
	Luminescence Spectra	25
	Photoluminescence	25
	Thermal Quenching	29
	Excitation Power Dependence	35
	Stress Dependence	38
	Absorption Spectra	41
	Thermal Queching Discussion	46
	Edge Emission	46
	Exciton Emission	48
	Excitation Power-Dependent Analysis	53
	Model for Edge and Exciton Emission	53
	Discussion	61
	Uniaxial Stress Effects on Exciton Emission	67
	Theory	68

Chapter Page

Discussion . . . 71

II. HALL EFFECT . . . 77

Introduction . . . 77
Experimental Details . . . 77
Sample Preparation . . . 77
Cryogenic Hall Effect Procedure . . . 78
Analysis of Data . . . 79
Electrical Data . . . 79
Results and Discussion . . . 87
Further Discussion . . . 97

IV. SUMMARY AND CONCLUSIONS . . . 105

REFERENCES . . . 111

LIST OF TABLES

Figure Page

1. Material parameters of bulk ZnSe crystals 6

2. Slope values for various PL lines in an Zn-extracted sample 62

3. Deformation potential and pressure coefficients of ZnSe 76

4. Parameters obtained from Hall measurements for three samples 89

LIST OF FIGURES

Figure Page

1. A unit cube of the zincblende structure in ZnSe 11

2. Electronic band structure of a zincblende type material 13

3. Experimental apparatus used in the luminescence studies 18

4. Experimental setup used for stress-dependent PL 21

5. Experimental setup used for optical absorption 24

6. Photoluminescence from melt-grown ZnSe at 12 K 26

7. Photoluminescence from as-grown SPVT ZnSe at 12 K 28

8. 12 K photoluminescence from Zn-extracted SPVT ZnSe 30

9. Plot of the intensity of the Li ABE line with ρ 31

10. Quenching spectra from a Zn-extracted sample
with ρ=30.1 Ω cm 32

11. Temperature dependence of the luminescence intensity 34

12. Excitation power-dependent data from a Zn-extracted
SPVT ZnSe sample 36

13. Plot of the luminescence intensity vs excitation power 37

14. Exciton and edge luminescence from a chemi-mechanically
polished sample 39

15. Stress dependence of the exciton emission in π-polarization 40

16. Stress dependence of the exciton emission in σ-polarization 42

Figure Page

17. Temperature variation of the band edge in optical absorption 43

18. Temperature dependence of important PL lines 45

19. The FWHM change with temperature for PL emission lines 51

20. PL transitions used in the rate equation analysis model 54

21. Energy position of the DAP1 emission line versus power 65

22. Schematic diagram of the band structure 69

23. Splitting of the FE and I_2 lines versus pressure . . . . .72.

24. Free carrier concentration as a function of temperature 88

25. $1/C^2$ versus V plot for a Schottky diode 91

26. The change of carrier mobility with temperature for three crystals 92

27. Theoretical plots of the mobility 94

28. Fit of the mobility using various scattering mechanisms 96

29. Energy level diagram showing the density of states .102

30. Plot of ε_3 as a function of $(N_D)^{1/3}$ for three Zn-dipped samples 104

CHAPTER I

INTRODUCTION

Historical Note and Recent Progress

The historical development of zinc selenide (ZnSe) started with an attempt to understand the effects of impurities as well as to identify their related energy states from optical and electrical studies by use of photoluminescence (PL) and photoconductivity techniques in the late 1940s and 1950s.[1,2] At the time, most II-VI semiconducting compounds were recognized as phosphors, but ZnSe was of interest because of its luminescence characteristics in the blue region of the spectrum when excited with ultraviolet (UV) light. However, the lack of success in growing large single crystals of high quality—a consequence of charge compensation and other types of effect to be discussed below—made the interpretation of experimental results difficult, and impeded the progress of reliably characterizing defect states in this material which in turn made the production of p-n junctions hard to achieve. Several years later (i.e., the 1960s), large semi-insulating single crystals with $\rho < 10^8\ \Omega$ cm became available by Marple *et al.*[3] but identification of defect states still remained a problem despite advances made in crystal purification by Aven *et al.*[4] such as the zinc vapor anneal method. As a result, industrial attempts to grow such crystals decreased drastically in the late 1960s. Although interest in ZnSe had slumped during this time, work on the optical properties of doped CdS and CdSe was already underway by Henry and Nassau.[5] Based on their analysis of the PL spectra, Merz *et al.*[6,7] were able to study the bound exciton and donor-acceptor pair spectra by appropriately doping ZnSe with the same type of donors and acceptors

By this time, identification of many shallow impurities were well established in ZnSe but progress in attaining material purity continued at a slow pace. A resurgence in material characterization emerged with the advent of epitaxial growth techniques originally developed for III-V semiconducting devices in the 1970s. In the II-VI arena for example, Yao *et al.*[8] successfully used molecular beam epitaxy (MBE) to grow ZnSe epilayers for the first time in the late 1970s. This non thermal-equilibrium technique which employed low growth temperatures suppressed contamination due to excessive residual impurities from the crystal growth environment, and almost entirely eliminated native defects (vacancies, interstitials or antisites) which had been a common problem encountered in crystals grown under thermal equilibrium conditions. With refinements in epitaxial techniques in recent years, continued incorporation of various impurities in novel and traditional materials to achieve low-resistivity amphoteric doping (p-n junctions) have been the focus of much work from the 1980s into the 1990s.

Lately however, ZnSe has been extensively studied because of its important technological applications such as blue-light-emitting diodes and laser diodes.[9] Unfortunately, the realization of producing efficient devices has been plagued by the unavailability of high conductivity bulk material of either n- or p-type form. For example, in the strongly polar semiconductors, it is difficult or if not impossible to make ZnSe p-type with low resistivities at room temperature. Until recently, this widely known difficulty in obtaining bipolar conductivity was thought to be due to self-compensation; an effect in which intrinsic (native) defects tend to reduce the electrical activity of the impurity dopant. However, Laks *et al.*[10] showed that native defect concentrations in p-type ZnSe and n-type ZnTe were not high enough to account for compensation although they state that experimental evidence is scarce to either support or contradict the role of native defects in these materials. It has also been shown that charge compensation can take place by amphoteric impurities. Neumark[11] considered a system of a single amphoteric impurity such as Li in ZnSe, and concluded that acceptor species (Li on a Zn site, Li_{Zn}) are

compensated by the donor species (interstitial Li, Li_i) when the concentrations of Li_{Zn} and Li_i are dominant over the total number of both electrons and holes. In addition to these mechanisms, other factors such as low solubility of uncompensated impurities intentionally introduced and high activation energies due to deep donor or acceptor centers are known to decrease the electrical conductivity as well.[12,13] To date, attempts to completely overcome these problems by various bulk crystal growth techniques and post-growth treatment schemes have been fruitless.

In addition to compensation which is still an inherent problem—contrary to what some people believe—in ZnSe-based epitaxial devices, formation of proper ohmic contacts poses another difficulty. Specifically, heating effects at the contacts is a major cause for device failure because of the relatively high contact resistance. In fact, in the first development of the blue-green laser diode from a ZnSe-based single-quantum well structure, Haase *et al.*[14] successfully accomplished lasing under current injection at 77 K, but heating at the contact prevented the device from lasing efficiently. Since then, efforts have been concentrated on quantum well systems based on (Zn,Cd)Se/ZnSe p-n and p-i-n heterostructures.[15-17] From these reports, device operation is achieved for three to four hours for low-temperature pulsed, blue-green lasers. However, pulsed lasers at room temperature and continuous-wave lasers at low temperatures last only a few minutes. Another possibility that is showing interest again is lasing by injection luminescence in metal-insulator-semiconductor (MIS) heterostructures made from ZnSe.[18] The goal has been to develop a room-temperature continuous-wave laser with a practical lifetime. From a basic physics viewpoint, such device structures are now preferred since the lasing mechanism is due to exciton recombination with binding energies (discussed in the next section) reaching up to ~ 40 meV; which is twice as high as that typically encountered in bulk crystals. To this end, efforts have concentrated on making devices primarily from quantum well structures. Once contact problems are resolved, the blue diode laser will move from "potential candidate" status to "actual feasibility" for practical applications.

This in turn means that vast improvements in a host of areas of technology such as xerography, optical readout density and large LED display panels will be a step closer to reality.

The commercial viability of light-emitting diode structures will depend on the type of substrate used for deposition of ZnSe epilayers. Presently, the most commonly used substrate is GaAs because of its small lattice mismatch (0.28%) and its relatively inexpensive cost. Despite the small lattice mismatch, dislocation defects are introduced at the interface due to biaxial strain, which are enough to cause detrimental effects in the optical properties of diode structures. Also, the different thermal expansion coefficients of the two materials and the formation of Ga_2Se_3 at the interface result in devices of low efficiency and short lifetime.[19] To overcome these problems it is necessary to make devices using homoepitaxial growth on a ZnSe Substrate. In the past, efforts to make ZnSe/ZnSe homoepitaxial devices have been hampered by the lack of large area, high crystalline quality, single crystal wafers of ZnSe. Recently, however, such wafers suitable for use as substrates have been grown using the Seeded Physical Vapor Transport (SPVT) method developed at Eagle-Picher laboratories.[20] Here emphasis has been placed on n-type wafers because these can be grown more readily than p-type, and n-type conductivity can be promoted with less difficulty than p-type conductivity. In this way, a p-n junction can be developed consisting of epitaxial p- and n-type layers on an n-type substrate.

Background Information

As is the case with most II-VI semiconductors, the PL spectrum of ZnSe at low temperatures is characteristic of exciton, edge and deep level luminescence. In the purest materials, the PL spectrum is dominated by peaks arising from exciton recombination. Briefly, an exciton is an electron hole pair bound together by the Coulomb interaction and exhibits a binding energy and a Bohr radius, as given from the effective mass

approximation (The analysis in this thesis is almost entirely based on this approximation which is analogous to the problem of solving for the bound state energies of an electron in the hydrogen atom except that the free electron mass is replaced by the effective mass and the free electron charge is modified by screening due to the dielectric constant of the medium.[111]), thus

$$E_x = -\frac{\mu e^4}{2\hbar^2 \varepsilon^2 n^2} + \frac{\hbar^2 K^2}{2M} \qquad \text{(CGS)} \qquad (1)$$

and

$$a_x = \frac{\hbar^2 \varepsilon n^2}{\mu e^2} \quad or \quad \frac{\hbar}{\sqrt{2\mu E_x}} \qquad \text{(CGS)} \quad (2)$$

where μ is the exciton reduced mass, $\hbar$K is the momentum of the center of mass, M=m_e^* +m_h^*, e is the static dielectric constant and n is the exciton orbital quantum number. Table I shows some material properties including the values of μ and e for ZnSe. The kinetic energy term in Eq. (1) is usually neglected because when the crystal is in the ground state (n=1), K = 0. However, an exciton with $K = n_r \omega / c$ (n_r is the index of refraction) can be created directly if the incident photon has energy $\hbar\omega$ (= E_g).[22] In bulk ZnSe, the term $\hbar^2 K^2 / 2M \approx 10^{-4}$ eV can be neglected compared to the binding energy of the free exciton. As a result, the optical transitions giving rise to free excitons are sharp. For bound excitons, the line shape is even sharper due to reduction of the kinetic energy of free excitons when bound to the impurity centers. In the case of excitons created by free electrons and holes with the former excited deep into the conduction band, the optical transitions are also sharp because the kinetic energy of the exciton is negligible, as specified by the momentum and energy conservation relations of the electron-hole pairs. The exciton emission region in bulk material is comprised of free and bound exciton transitions ranging from 2.8040 to 2.7825 eV. The notation that is usually associated with the main emission peaks are: FE, a free exciton; I_2, an exciton bound to a neutral donor; I_x

TABLE I

MATERIAL PROPERTIES OF BULK ZNSE

Property	Symbol	Value
Crystal Structure		Zincblende
Band Gap (direct)	E_g	2.7074 eV, 2.8225 eV (RT, 12 K)[a]
Band Gap Temp. Coeff.	α^*	8.625×10^{-4} eV/K[a]
Lattice Constant	a	5.6710 Å[b]
Dielectric Constant	ε	8.9[c]
High Freq. Dielectric Cons.	ε_∞	5.7
Electron Effective Mass	m_e	$0.17m_o$
Hole Effective Mass	m_h	$0.67m_o$
Light-Hole Mass	m_h^{lh}	$0.38m_o$, $0.37m_o$ ([100], [110])[d]
Heavy-Hole Mass	m_h^{hh}	$1.11m_o$, $1.95m_o$ ([100], [110])[d]
Reduced Mass	μ	$0.105m_o$ [f]
Expansion Coefficient	α	7×10^{-6} /K[b]
Donor Binding Energy	E_d	29.2 meV
Acceptor Binding Energy	E_a	111.6 meV
LO Phonon Energy	$h\omega_{LO}$	31.1 meV[c]
TO Phonon Energy	$h\omega_{TO}$	25.3 meV[c]
Elastic Compliance Const.	S_{11}	2.26×10^{-3}/Kbar[e]
" " "	S_{12}	-8.5×10^{-4}/Kbar[e]

TABLE I (Continued)

Property	Symbol	Value
" " "	S_{44}	2.27 x 10^{-3}/Kbar[e]
Electron Mobility	μ_n	550-700 cm^2/Vs [b]
Density	D	5.85 gm/cm^3 [b]
Deformation Potential	a	-1.8[a]
" "	b	-0.37[a]

[a]This work

[b]Eagle-Picher Laboratories (performed on Zn-extracted samples)

[c]Average from Ref. 23 (8.6) and Ref. 24 (9.1), phonon energy from Ref. 23

[d]Ref. 25

[e]Ref. 26

[f]Ref. 24

(mistakenly confused with I_3, an exciton bound to an ionized donor because of the same energy position as I_x), an exciton bound to a neutral donor; I_1, an exciton bound to a neutral acceptor; and I_1^{deep} (or I_1^d), an exciton bound to a deep acceptor. It should be pointed out that the identification of I_3—first originated from the work of Merz *et al.*[6,7]—is still a subject of some controversy. Complications in the assignment of I_3 arise from the presence of I_x (occurring near the position of I_3) encountered in samples treated by Zn vapor annealing, as first noted by Dean and Merz.[27] They did not know the identity of the defect responsible for I_x, and is still a topic of much confusion to this day. However, they did know that the emission behaves neither like I_1 nor like I_2 in a magnetic field. Since then, mechanisms for I_x have been proposed, including an exciton bound to an ionized

donor. Another controversial PL line is the previously assigned 1LO phonon replica of the free exciton.[27-29] Earlier, it had been suggested that this line is due to the acoustic phonon replica of I_1^d (Ref. 6), but such a notion was dismissed later because of the presence of this peak in the electroabsorption spectrum.[21] PL studies on the so-called 1LO phonon replica of the free exciton show that this line is due to defect luminescence not associated with excitonic transitions.[30] Part of the objective of this thesis is to determine the origin of these lines.

At high impurity concentrations, the edge emission region composed of free-to-bound (e-A^o) and donor-to-acceptor pair (DAP) transitions dominate the PL spectrum and range from 2.71 to 2.68 eV. Typically, a series of DAP emission peaks each with a unique designation according to the position of the peak energy is observed in ZnSe, and range from the P-series (2.677 eV) to the R-series (2.715 eV). Each series is attributed to specific donor and acceptor impurities. When the concentration of defects such as the SA center, for example, or deep level impurities such as the transition or noble metal ions is high, the PL spectra display strong deep level luminescence. This is commonly seen in the 2.3–1.95 eV region of the spectrum.

Phonon-assisted transitions are also observed in the exciton and edge emission regions at low temperatures. Due to the nature of polar semiconductors, longitudinal optical (LO) phonons couple strongly to the excitons since the exciton Bohr radius ($a_x \sim$ 50 Å) is large compared to the lattice spacing which makes the excitons highly polarizable. DAP and e-A^o are also highly polarizable, so they couple strongly to the lattice as well. The PL spectrum show a series of peaks (phonon replicas) separated by the LO phonon energy (Table I) each decreasing in intensity after the zero-phonon line for transitions involving phonon cooperation. Transverse optical (TO) phonon replicas are rarely observed in ZnSe since their effect in the lattice is weak.[29] Acoustical phonons mainly play a role in broadening the zero-phonon line rather than produce a distinct, observable emission line because of their small energies.[31,25]

Application of various optoelectronic devices for commercial use is still limited because control of the electrical and optical properties of bulk ZnSe are not well established. As stated in the previous section, this is mainly a result of charge compensation effects due to native defects which are undesirable entities in the crystal. The dominant native defects in stoichiometric p-type material are claimed to be Zn_{Di}^{2+}, V_{Zn}^{o} and Se_{Zn}^{2+} whereas in stoichiometric, n-type material these are V_{Zn}^{2-} and Zn_{Se}^{-}.[10] In the case of Zn- and Se-rich p-type materials, the major defects are Zn_i and Se_{Zn}, respectively for which both are donors doubly charged. The dominant defects in n-type ZnSe are Zn_{Se} and V_{Zn} for Zn- and Se-rich materials, respectively. These defects act like acceptors. Another type of defect (complex) commonly observed is the "self-activated" (SA) center which is a donor-V_{Zn} pair.[33] This center is typical of ZnSe and ZnS materials and forms a complex in the presence of chlorine, bromine, iodine, aluminum or gallium donors. Problems associated with the stability of impurity dopants in the host crystal also make it difficult to manipulate the electrical and optical properties. An example of this is the technologically important case of Li_{Zn}, with its incorporation in the lattice giving rise to an acceptor in ZnSe. Since Li is a very small atom, its diffusion rate is quite fast and takes place through interstitial sites as suggested by Neumark and Herko.[34] Haase *et al.*[35] tested this by sandwiching a thin Li-doped layer between two undoped layers and found that Li diffused into a uniform distribution throughout the undoped layer as shown by their SIMS profile studies. Alternatively, incorporation of other shallow acceptor impurities (e.g., nitrogen) as stable dopants are currently being investigated by using radical doping techniques.[36]

Crystal Structure

ZnSe consists of a face-centered cubic arrangement of Se atoms which is characteristic of the zincblende structure. Although ZnSe prefers to stay in the more stable form of the cubic structure, it can nevertheless form in the hexagonal (wurtzite)

structure. The hexagonal structure tends to form in semiconductors of high polarity but this is precluded in ZnSe. In zincblende, two face-centered cubic structures may be visualized as being separated from each other by one-fourth of the body diagonal,[37] as shown in Figure 1. There are four atoms per primitive cell. Using the indices [uvw] to represent the direction of a vector in the crystal, the vector displacements of the Se atoms are [000]a, [011]a/2, [101]a/2, and [110]a/2 and those of the Zn atoms are [111]a/4, [133]a/4, [313]a/4, and [331]a/4. Thus the Se atoms represented by their vector displacements form the corners of a regular tetrahedron with a Zn atom at its center. The interatomic distance for ZnSe in the zincblende structure is 2.456 Å.

The crystal structure may take on a slightly distorted form when impurities are introduced in the lattice such as the alkali metals (Li, Na and K) or the transition metals (Cu, Ag, Fe, for example). Calculations have shown that ZnSe has a charge distribution that is mainly ionic; thus it is a polar semiconductor. The ionic radii of Zn^{2+} and Se^{2-} is greater than the interatomic distance, so both radii will be scaled to the ratio of the interatomic distance to the sum, i.e., 2.456 Å/(0.7994 Å +1.98 Å). The scaled ionic radius of Li is 0.57 Å and that of Zn is 0.67 Å. By comparing ionic radii, Li can easily substitute for Zn, thus introducing acceptor species in the lattice since Li has a lower chemical valency than Zn. Because of the small size of Li, it can also incorporate itself interstitially since the triangular space formed between the cation and the two nearest anions has a radius of approximately 0.70 Å. Al on the other hand, has a scaled ionic radius of 0.49 Å and easily substitutes for Zn (Al_{Zn}) which acts like a donor. Despite its small size, however, Al does not tend to fit in the lattice interstitially because of its relatively high electronegativity to attract electrons for bond formation.

The structure may also be altered slightly in the presence of Zn or Se vacancies.[33] A Zn vacancy acts like an acceptor center. This defect can trap a hole into the orbitals of the four surrounding Se neighbors. The degeneracy associated with the Se p orbitals gives rise to a spontaneous distortion where the hole becomes localized at one of the four Se

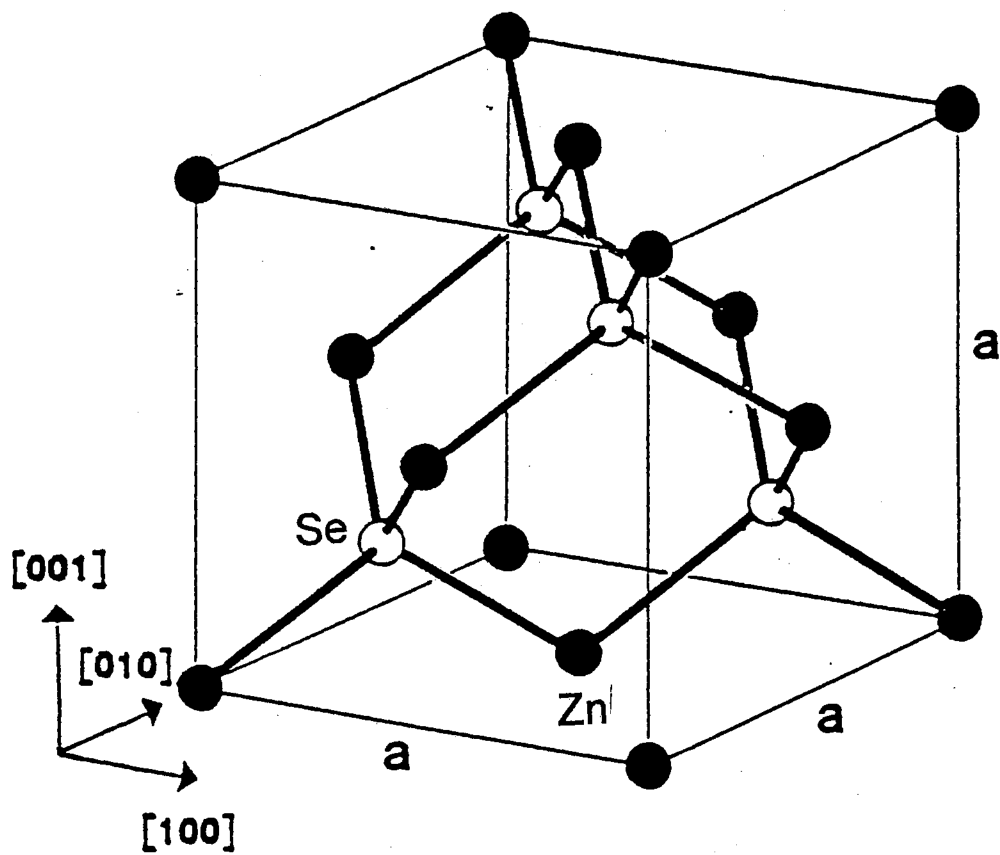

Figure 1. A unit cube of the zincblende structure in ZnSe

atoms. The Se vacancy on the other hand, acts like a donor center. Here the trapped electron is distributed equally over the s orbital of the four Zn neighbors.

Band Structure

Figure 2(a) shows the band structure of ZnSe along with the important symmetry points. In the figure, the L, Γ and X points are along the π/a(111), (000) and 2π/a(100) axes of the Brillouin zone, respectively. The optical absorption edge of ZnSe corresponds to direct transitions from the highest valence band to the lowest conduction band at the Γ point (k = 0). Likewise, the PL emission is represented by direct transitions from the lowest conduction band to the highest valence band. Transitions occurring at the Γ point are of interest here. Absorption transitions occurring at other points are possible but they will not be considered. (Refer to Adachi and Taguchi for a detailed description.[23]) Figure 2(b) shows an expanded version of the band structure at the zone center for a zincblende type material. Without the effects of strain or spin-orbit splitting, the edge of the valence band at k = 0 is composed of the sixfold degenerate p orbitals. The spin-orbit interaction removes the degeneracy associated with the p states and split into a fourfold $P_{3/2}$ multiplet ($J = 3/2$, $m_j = \pm1/2$, $\pm3/2$) and a $P_{1/2}$ multiplet ($J = 1/2$, $m_j = \pm1/2$), as shown in the figure. The conduction-band edge ($J = 1/2$, $m_j = \pm1/2$) which has s-like orbitals does not experience splitting. The $J = 3/2$, $m_j = \pm1/2$ state is the light-hole component of the valence band, the $J = 3/2$, $m_j = \pm3/2$ is the heavy-hole component, and the $J = 1/2$, $m_j = \pm 1/2$ state is the spin-orbit split-off band. After splitting, the light-hole band mixes with the split-off band as shown in the figure. However, the final shape of the valence bands due to mixing take on the form represented by the dashed lines. The type of diagram like the one shown in Figure 2(b) will be adopted in this work since it is commonly used to describe all the optical transitions observed in PL.

Figure 2. Electronic band structure from a zincblende type material. (a) Typical band diagram of ZnSe showing the main symmetry points (Ref. 112). (b) Expanded version of the band structure at the Γ point illustrating the conduction band (C.B., J=±1/2, m_j=±1/2), heavy-hole (J=±3/2, m_j=±3/2), light-hole (J=±3/2, m_j=±1/2) and the spin-orbit split-off (J=±1/2, m_j=±1/2) valence bands (V.B.). The dashed lines indicate the final form of the valence bands after mixing of the light-hole with the spin-orbit states.

Scope of this Study

The objective that we wish to accomplish is twofold. Firstly, it is desired to employ various characterization techniques to SPVT ZnSe prepared in different ways to acquire knowledge of the optical and electrical properties and to eventually establish some way to control them so that a high quality substrate can be developed for homoepitaxy. (Currently, GaAs is the substrate most commonly used because of its near-chemical compatibility with ZnSe and its relatively low cost compared to other exotic substrates. However, despite the small differences in their chemical properties, these differences are large enough to cause adverse effects in device performance.) Secondly, it is the goal of this project to obtain a better understanding of the defects responsible for the emission characteristics at low temperatures in the SPVT samples. By doing so, it should be easier to identify the origin of the room-temperature blue light emission in these materials. Particularly, it is of interest to determine the origin of the so-called I_x emission which remains controversial to this day. Also, the transition mechanism that gives rise to the I_V (usually referred to as FE-ILO) emission is hoped to be clarified. Furthermore, attempts to resolve the interestingly but particularly small activation energies often obtained from Hall measurements will be made. As part of an effort to fully characterize these materials, optical and electrical characterization measurements have been carried out on SPVT ZnSe materials. Results describing measurements of PL and Hall effect characteristics will be the foci of this work.

CHAPTER II

PHOTOLUMINESCENCE AND OPTICAL ABSORPTION

Introduction

Data on PL and optical absorption taken in the temperature range from 4.2 to 300 K are presented in this chapter. Briefly, PL is a non-destructive characterization technique which lends itself as a powerful method for the determination of the energies of exciton states and of certain impurities in semiconductors. Particularly, it can be applied to detect shallow impurity states but can also be suited to find certain deep-level states, as long as the radiative recombination processes dominate the nonradiative ones. Although this technique has been extensively used in the past to characterize bulk materials, it is now an invaluable tool to probe exciton states in quantum-confinement structures. In any event, this chapter will be confined to PL studies of bulk SPVT ZnSe materials. The techniques employed here are thermal quenching, excitation power dependence and stress dependence of PL. These different measurements are applied to a set of samples prepared in various ways in order to draw correlations between the optical properties from specimen to specimen. For example, the dramatic differences in crystal purity as evidenced in the spectra obtained from melt-grown, SPVT as-grown and Zn-extracted materials are illustrated. By combining different PL studies, it is mainly intended in this chapter to determine the nature of the emissions that give rise to PL. Specifically, the thermal and stress-dependent behavior of the exciton emission lines I_3 (or I_x) and I_V (or so-called FE-1LO), are monitored and conclusions are drawn about the nature of these

emissions. In addition, the deformation potential constants are calculated from these results. The optical absorption edge as a function of temperature is examined and some material parameters are determined from the temperature dependence of the free exciton absorption peak. All this information (PL and absorption) is then put together to help identify the origin of the blue light emission from this material.

Experimental Details

Sample Preparation

Large area, untwinnied, high crystalline quality, single crystal wafers of ZnSe used in this study were grown at Eagle-Picher Research Laboratories by the SPVT method. Melt-grown samples obtained from the high-pressure Bridgman method were also used in this work. The details of both growth processes have been described elsewhere.[20] The melt-grown and SPVT as-grown samples were all n-type and highly compensated with room temperature resistivities greater than 10^5 Ω cm. Most samples used in this work received a cleanup etch from 5-10 minutes to remove the original surface. The etchant used was a solution of bromine in methanol with a 0.5% to 3% by volume of bromine. Once the samples were etched, they were immediately immersed in a methanol solution to remove traces of bromine and subsequently, they were cleaned with deionized water. Other samples were first chemically treated with bromine-methanol and then mechanically polished. This process was repeated for several cycles. For crystals cut along the (111) planes, a dull-white thin film was sometimes observed on one of the etched surfaces—perhaps an indication of the oxidized Zn face by air. After the SPVT as-grown specimens were etched, it was noted that the 500 nm PL band (denoted as the S or M band in the literature) had drastically decreased and consequently, the exciton emission increased. This may be an indication that surface states due to polishing are introduced at

the surface of unetched materials. Unless specifically stated, all data reported herein were taken on etched samples. Attempts to promote n-type conductivity were moderately successful by dipping some samples in a molten Zn solution—a process known as the Zn-extraction treatment. The samples were held in the solution from 2 to 6 days at 975 °C with final net room temperature resistivities ranging from 3.8 Ω cm to 30.1 Ω cm. Sample dimensions ranged from 5.5 mm x 5.5 mm x 5.5 mm cubes for the stress measurements to 1 mm x 4 mm x 4 mm plates for other measurements.

Photoluminescence, Thermal Quenching and

Excitation Power Dependence Experimental Setup

The PL spectra were recorded with the experimental setup shown schematically in Figure 3. The cryogenics part of the setup is a CTI-Cryogenics model 22 Cold Head which operates in conjunction with the model 22C Cryodyne Cryocooler system. All samples were mounted on the copper finger of the cryostat with a dab of Si vacuum grease and were allowed to cool to low temperatures (~ 12 K). To reach higher temperatures, power was supplied to the copper cold finger by a TRI Research T-2000 Cryo Controller and the temperature was monitored with a Cryo Cal Diode sensor. A platinum sensor built in the sample holder was also available for temperatures exceeding 300 K; however, its use was not necessary. The temperature ranged between 12 and 300 K for the quenching studies, and each temperature set point was held constant to within ± 0.1 K.

Creation of electron-hole pairs at the sample surface was accomplished by illuminating with the 351.1/363.8 nm lines from a Spectra-Physics, model 2025-4 Argon-Ion Laser. Before excitation, the beam passed through a narrow bandpass filter to block out unwanted fluorescence lines from the lasing medium. The reflected beam from a

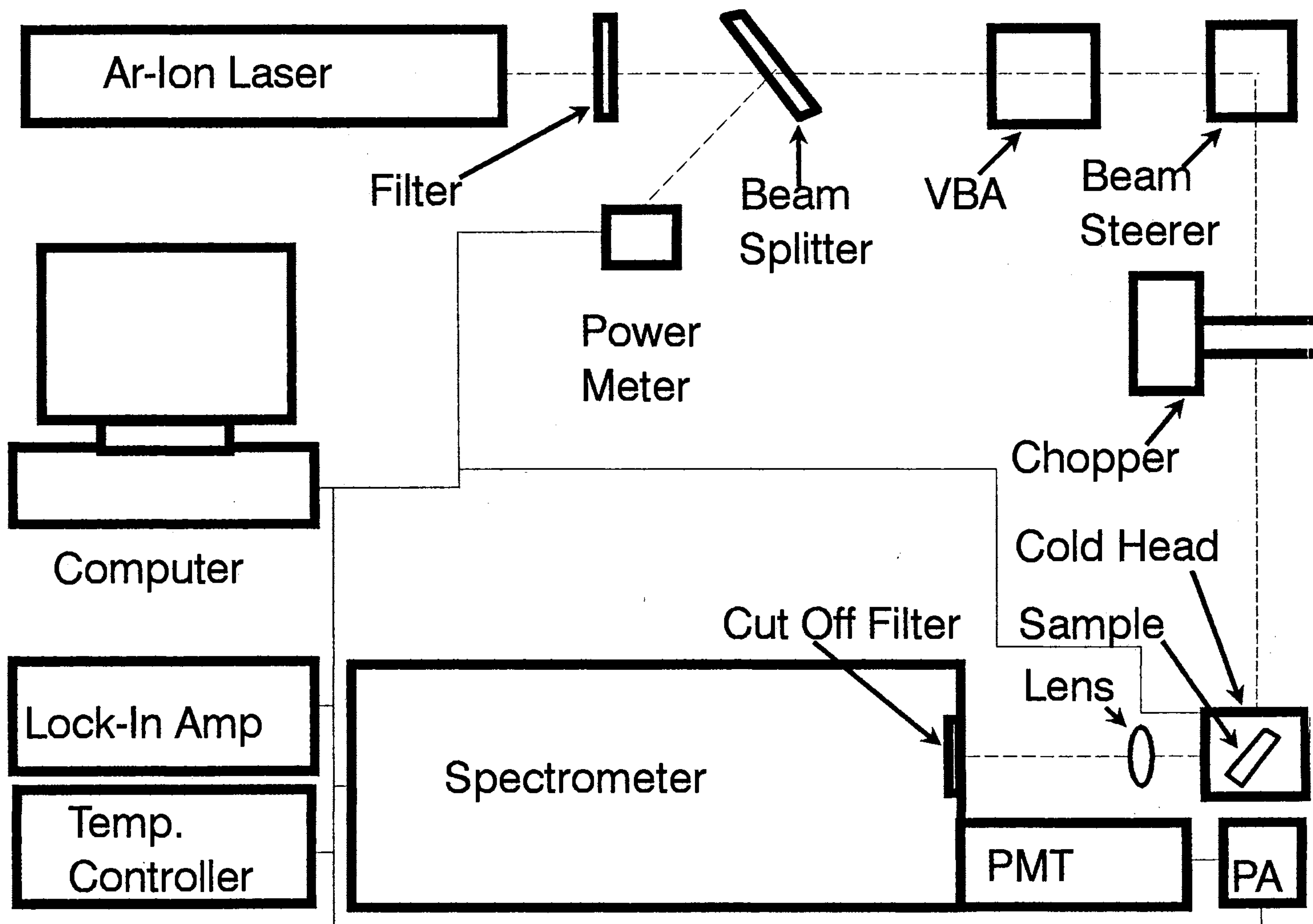

Figure 3. Experimental apparatus used for the PL, quenching and excitation power-dependent measurements.

beamsplitter with 30/70% transmission was monitored with a model 815 Power Meter from Newport Research Corporation to compensate for fluctuations of the PL signal due to minor power instabilities in the beam. All measurements were then multiplied by a correction factor to obtain the final spectra. Illumination took place with the laser beam at an angle between 45° and 60° from a line normal to the sample surface. For standard measurements, the power of the laser beam was maintained at approximately 1 mW to avoid the generation of heat. For the excitation power dependence work, the laser beam power ranged from 3 μW to 80 mW. The power was varied with a Newport Research Corporation, model 935-5 variable beam attenuator (VBA) equipped with a micrometer knob for fine adjustment, as shown in Figure 3. It should be pointed out that a set of Reynard Enterprises, Inc. Metallic-Coated Neutral Density Filters were tested before using the VBA. However, their use was discontinued because of instabilities in the attenuation at high powers. During the initial stage of this experiment , it was noted that the intensity of the PL lines decreased with continued laser illumination at high powers. It was speculated that the intense laser beam heated the sample. In order to reduce heating effects at the surface due to the high laser powers, a heat sink plate was designed comprising a CaF_2 disc and holder, and was place on top of the sample.[38] Indium foil was used between the sample and the CaF_2 disc, and between this disc and the copper plate to provide good thermal contact. With this modification completed and installed, the intensity of the PL peaks was observed to monotonically increase with an increase in laser power. An attempt to use sapphire (which has high thermal conductivity at low temperatures) as a heat sink proved to be unsuccessful because luminescence occurred when the plate was subject to strain. Basically, this experiment consisted of incrementing the laser beam power and recording the corresponding change of the PL spectrum.

The emission spectra were measured by using a SPEX model 1702/04 Spectrometer with focal length of 0.75 m and first order dispersion of 11 Å/mm, corresponding to a ruled grating of 1200 lines/mm blazed at 500 Å. A cutoff filter was

placed at the entrance slit to eliminate stray light from the surroundings and scattered light from the laser beam. Since the exciton emission is characterized by sharp lines, high resolution was achieved with the entrance slit typically set to 10 μm provided the luminescence signal is strong. The resolution attained for this slit setting was 0.1 Å. The exit slit was twice the entrance slit in order to get good light throughput. An Oriel Corporation, model 6047 Hg-Ne lamp was frequently used to calibrate the spectrometer to the nearest 0.05 Å. The luminescence signal was detected with a Thorn EMI Gencom Inc., model 9684 Photomultiplier Tube (PMT) with S-20 spectral response. A chopper and an Ithaco model 3962 Single Phase Lock-In Amplifier served to synchronously detect the signal output from the PMT. Between the PMT and the lock-in amplifier was a model 566 Preamplifier (PA) from Ithaco. This device prevented draining of large signals from poor electrical grounding of the PMT. When signals were too large for the preamplifier, they were first directed to a box with a variable resistor to avoid overflow of the preamplifier. Equipment automation and interfacing were performed with an HP-86B Microcomputer from Hewlett Packard for data acquisition and analysis. (For details of the operation of the computer code, refer to Cotal[38]). All measurements were carried out in a vacuum better than 10^{-5} torr.

Uniaxial Stress Experimental Setup

Cryogenics and Stress Apparatus. The experimental arrangement for the uniaxial stress measurements is shown in Figure 4. The setup is the same as that depicted Fig. 3 except that the cryogenic system used here is composed of two concentric, Pyrex glass dewars with the inner one measuring 28" (L) x 2" (DIA) and the outer one 27" (L) x 3" (DIA) capable of supporting liquid Helium (LHe) at 4.2 K and liquid Nitrogen (LN_2) at 77 K. For details on the operation of the other equipment in the figure, refer to the previous section. Both dewars were made in the glass shop at Oklahoma State University. Each

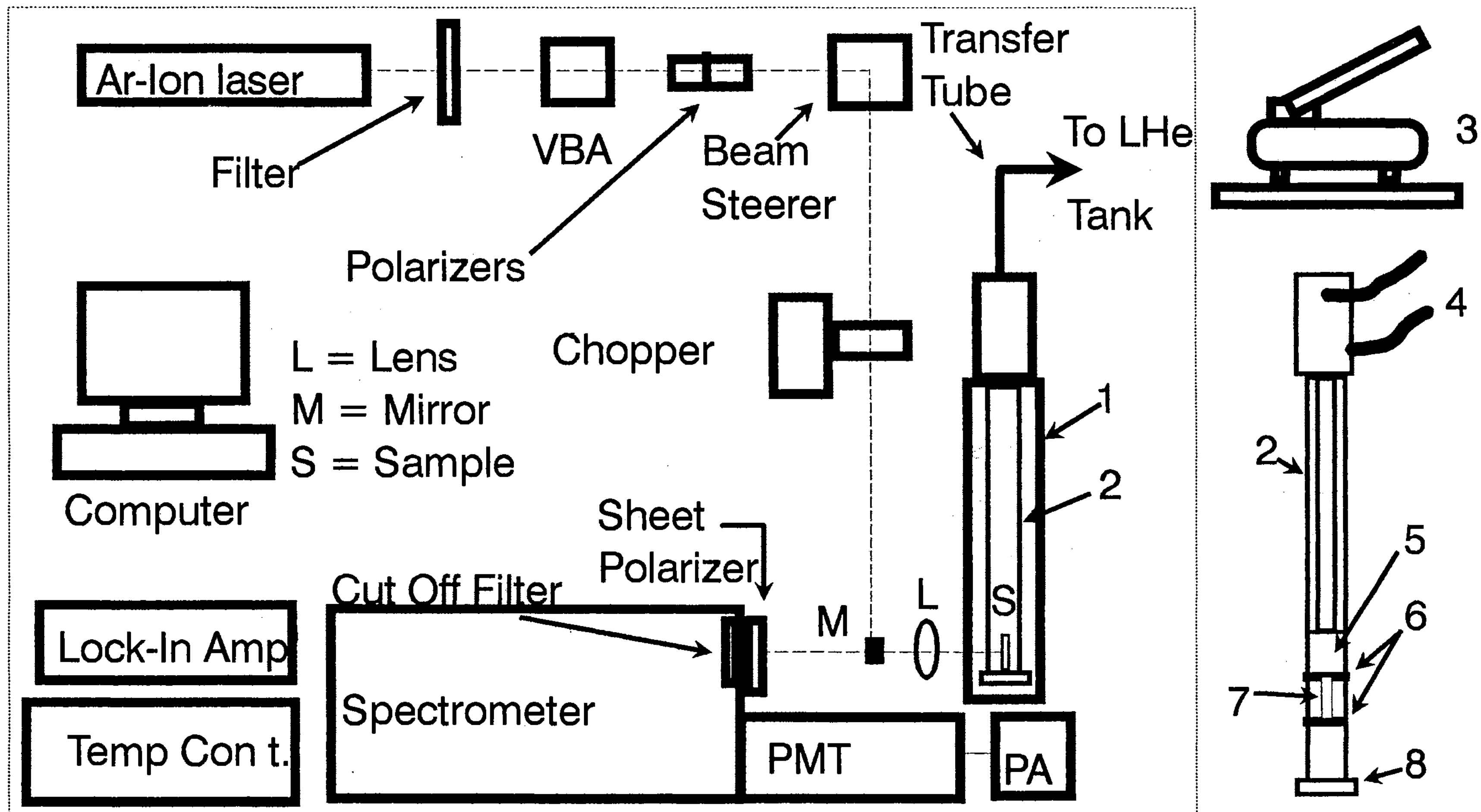

Figure 4. Experimental setup for the stress-dependent PL measurements (1) Stress apparatus, (2) stainless steel rod and piston, (3) hydraulic pump, (4) hydraulic hoses, (5) piston, (6) cardboard discs, (7) sample and (8) plug.

dewar is vacuum-sealed and coated with silver for thermal radiation shielding. The inner dewar holds LHe while the outer one is filled with LN_2 which acts like a shroud to prolong the use of LHe to about 4 hours. Before the cryogens are poured in the dewars, the dewars were first purged with He gas to prevent ice from forming on the walls. The LHe came from a 100 liter tank supplied by the Texas Bureau of Mines. The transfer tube is from Andonian Cryogenics Inc., and was borrowed from Dr. Martin. In brief, after the dewars were placed on the translation stage and the transfer tube inserted first in the tank and then in the inner dewar followed by purging, the dewars were then filled with LN_2 and subsequently with LHe. A model H-311-SM-1x1 long stainless-steel piston from Airoyal MFG Co. capable of exerting a force of 2000 lb on a 0.785 in^2 bore area of the piston head, and hydraulic system (from Enerpac) are also shown in the figure. Usually, the pressure on the samples did not exceed 10^5 psi, and the formula to convert pressure from the gauge reading (GR) of the stress apparatus to the sample pressure (SP) was SP = (GR)(0.785 in^2)(1.01325 bar)/(14.7 lb/in^2)(A_s) where A_s is the sample area. Two cardboard discs about 1 mm thick were placed at the top and bottom of the sample to eliminate, or at least reduce, the non uniform distribution of stress. Nitrogen bubbles originating from the piece of foam separating the two dewars were unavoidable. The bubbles interrupted the light beam resulting in noisy data. As a result, the spectra were averaged during the experiments when time allowed. An attempt was made to use an EG&G Princeton Applied Research model 1460 Optical Multichannel Analyzer (OMA) and model 1420 Solid State Detector to accelerate the data-taking process. Unfortunately, serious alignment problems with the instrument were encountered, along with a critical lack of high resolution.

Optics Layout. The ZnSe crystals were excited at near-normal incidence to the sample surface with the UV lines from the Ar-ion laser. A very small rectangular mirror was placed in front of the lens (L) to achieve near-normal incidence, and the k vector of

the incident light was always perpendicular to the direction of applied stress (P) as shown in Fig. 4. The stress-dependent PL spectra were measured with the laser beam polarized parallel (π-polarization) and perpendicular (σ-polarization) to the stress direction. In this work, terminology such as π- and σ-excitation, and π- and σ-emission (or luminescence) will always refer to a particular polarization component that is either parallel or perpendicular to P. Two Glan-Thompson prisms were employed to accomplish the polarized excitation. Since the laser beam is only π-polarized, the first prism was used to rotate the π-polarization vector to 45° while the second prism was used to single out its x- and y-components. The luminescence signal was also polarized parallel and perpendicular to the stress direction with use of a sheet polarizer from Melles Griot. For one specific sample the excitation and emission were polarized giving four permutations of polarization. The laser power was kept at $\sim$ 0.5 mW for π- and σ-polarization to avoid heat generation. Stress measurements were performed with the direction of applied stress parallel to the (100), (110) and (111) faces while the laser beam was incident perpendicular to these faces. In this thesis, work on the (100) plane will be presented only. The unit of stress in the literature is normally expressed in kbar (=14,507.8 lb/in^2), so likewise, this unit will be adhered to throughout the thesis.

Optical Absorption Setup

The spectrometer used for the absorption measurements was a Varian model CARY5. The samples were housed inside the same cryostat as that used for the PL studies and this in turn was positioned inside the sample compartment of the CARY5. Figure 5 shows the layout of this experiment. For the most part, the rear beam attenuator had to be used to improve signal-to-noise statistics and each scan had to be averaged over 10 hours for further noise reduction. Most of the noise was a result of application of a narrow spectral bandwidth (SBW) and data interval to these measurements which are both

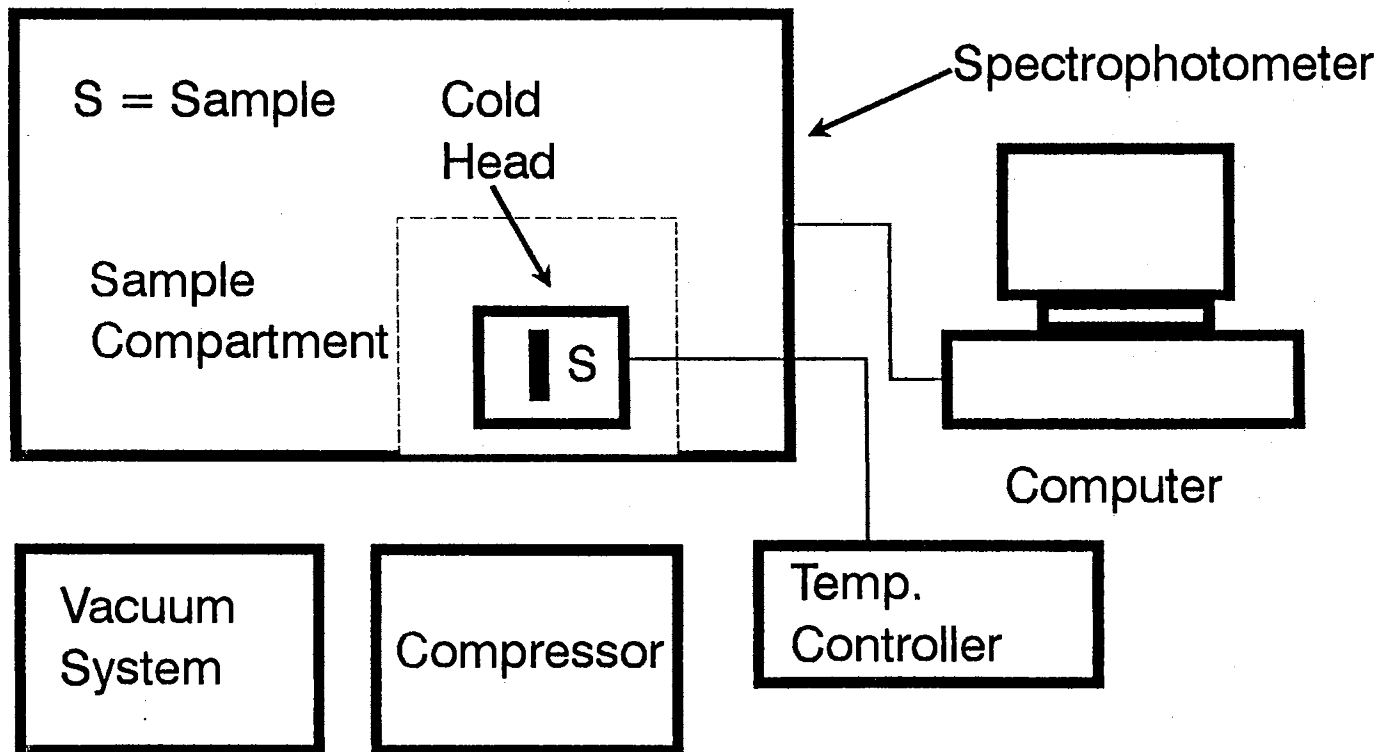

Figure 5. Experimental setup used for the optical absorption measurements.

necessary to obtain a high resolution at low temperatures. The former parameter had a value between 0.5 and 0.7 nm whereas the latter was set up to its lowest limit (high resolution), 0.02 nm/data point. At higher temperatures where the absorption peaks of interest are no longer discernible, the SBW was 2 nm. A Hewlett Packard Vectra microcomputer served as the work station for data acquisition and analysis. The temperature-dependent absorption spectra were monitored over the range from 13 K to 290 K.

Experimental Results

Luminescence Spectra

Photoluminescence. Figure 6 shows a typical PL spectrum from melt-grown ZnSe. The main feature is the strong DAP emission with a zero-phonon line at 2.6813 eV and is characteristic of all the melt-grown samples studied. This emission is part of the so-called P-series associated with a Na_{Zn} acceptor and a donor, believed to be Al_{Zn}, as suggested by Merz *et al.*[39] from PL studies. Weak exciton emission (Ex) is observed. On an expanded energy scale a weaker Q-series DAP can be seen with a zero-phonon line at 2.6953 eV. Acceptor-bound exciton (ABE) lines are observed at 2.7937 eV (I_1^{Na}) and at 2.7827 eV (I_1^d, along with its phonon replicas) with the latter line due to deep Cu_{Zn} acceptors, or V_{Zn}.[40] The acceptor ionization energy can be calculated with application of Haynes' rule: $E_A = (E_{FE} - E_{ABE})/0.1$ where E_{FE} is the free exciton emission energy and E_{ABE} is the acceptor bound exciton energy. For I_1^{Na} in this expression gives a Na_{Zn} acceptor at Ev + 93 meV. Other melt-grown samples showed a weak donor-bound exciton (DBE) line (I_2 at 2.7975 eV). The transition energy for DAP emission is given by

$$E = E_g - (E_A + E_D) + E_{coul} \tag{3}$$

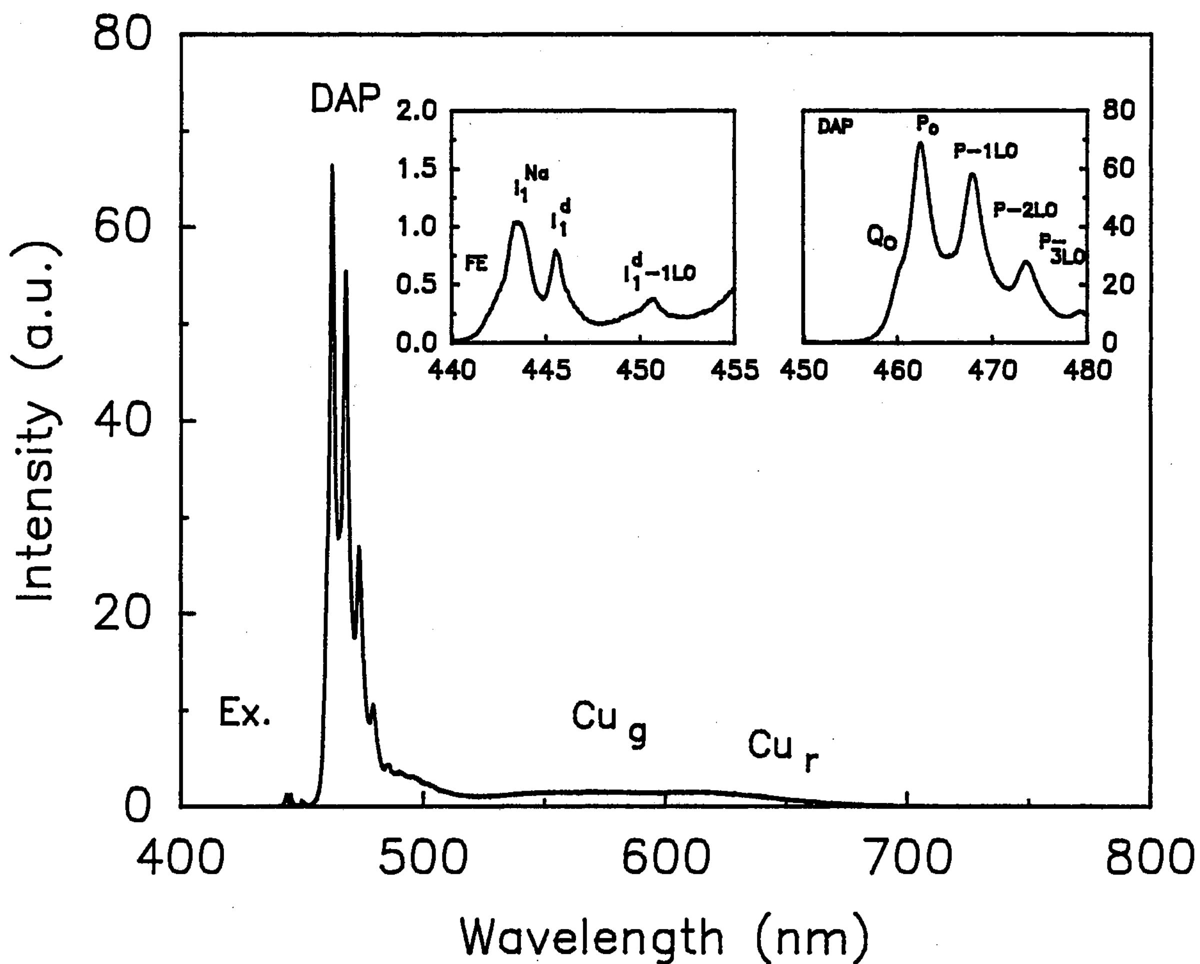

Figure 6. Photoluminescence from melt-grown ZnSe at 12 K. On an expanded wavelength scale, the insets show the exciton emission region (left inset) and DAP emission with a Q-series at higher energy.

where E_A and E_D are the acceptor and donor ionization energies, respectively; and E_{Coul} (= $e^2/\varepsilon r_{DA}$) is the Coulomb interaction between the donor and acceptor ions separated by a distance r_{DA}. The remaining terms are defined in Table I. From both the P-series DAP (using E_A = 93 meV for the Na_{Zn} acceptor, E_{Coul} = 10 meV (Ref. 41)) and from the DBE line (using Haynes' rule) we find a donor state at E_c - 27 meV, consistent with the value expected for Al_{Zn} donors. Another feature prominent from melt-grown materials are the strong deep-level copper-green (Cu_g, at 2.5 eV) and copper-red (Cu_r, at 1.98 eV) emissions, with the latter possibly involving contribution from the SA emission band (2.14-1.97 eV).

In Fig. 7, similar data are illustrated for as-grown SPVT material. Here the Cu-related I_1^d line and its LO-phonon replicas dominate the entire spectrum. Also observed is the I_x line at 2.7945 eV and a DBE line (I_2) at 2.7991 eV. (Some authors claim that I_x is due to an exciton bound to an ionized donor and call it I_3. We believe (see discussion later) that the line is due to a deep neutral DBE and prefer to use the designation I_x.) Haynes' rule for this latter emission gives a donor state at E_C - 18.5 meV. The inset also shows a shoulder on the high-energy side of I_2, possibly a FE. Weak Cu_g and Cu_r emissions are present, along with SA emission and an unidentified broad emission (typically denoted as I_S or I_M) near 500 nm. As stated in the sample section, this band disappears after etching—perhaps an indication that it is surface-related. The lineshape of the I_S band has been observed with a series of phonon replicas, and is thought to be due to DAP transitions from close pairs with the acceptor deep in the bandgap.[42] Its origin, however, is still debatable. Y-emission (2.602 eV) which is characteristic of ZnSe/GaAs heteroepitaxial layers was observed in some as-grown crystals but also disappeared after etching. No outstanding DAP features are observed. The presence of strong I_1^d implies that the concentration of Cu centers (or V_{Zn}) is quite high. It is worthwhile to mention that Zn-dip treatment studies performed by Isshiki *et al.*[43] suggest that I_1^d is due to V_{Zn}. Analysis of Zn-dip treatment data from this work in conjunction with thermally stimulated

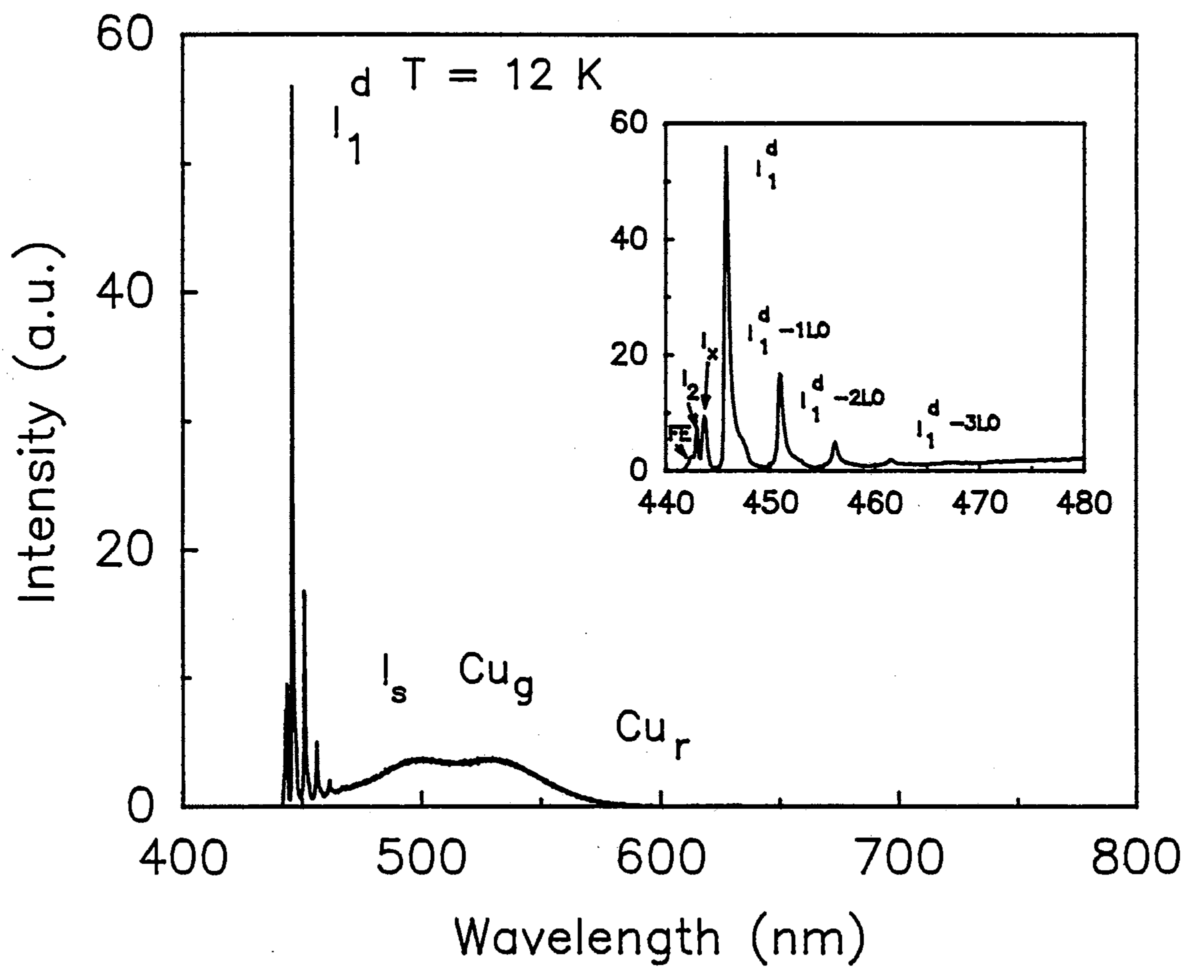

Figure 7. Photoluminescence emission spectrum at 12 K for an as-grown sample of SPVT ZnSe.

conductivity data imply that this line could be due to Cu impurities however, the possibility of V_{Zn} should not be dismissed.[40]

All as-grown SPVT samples are semi-insulating with high resistivities at room temperature. After Zn-extraction, the samples exhibit spectra similar to the one shown in Fig. 8. The I_1^d lines have now been removed, along with the Cu_g and Cu_r emissions, as anticipated. The I_x emission is now the dominant signal with the I_2 line at 2.7991 eV line also observed. The Zn-extracted samples display n-type conductivities with resistivities ranging from 3.8 Ω cm to 30.1 Ω cm. This difference in the resistivities is reflected in the emission spectra in that the higher resistivity samples display both an ABE line at 2.7912 eV due to Li_{Zn} acceptors at Ev + 114 meV as calculated from Haynes' rule and a Q-series DAP emission, with a zero-phonon line at 2.6900 eV. These features increase in size with the resistivity of the sample as shown in the inset of Fig. 8. Depicted in Fig. 9 is the variation of the intensity of I_1^{Li} as a function of resistivity for all the Zn-extracted samples studied and shows how the intensity increases as ρ increases.

Thermal Quenching. The temperature-dependencies of the exciton and edge emission lines for a Zn-extracted sample is depicted in Figure 10. Two sets of quenching data were taken, one in the range from 12 to 80 K with a typical excitation power of 1 mW and the other from 60 to 300 K at 4 mW. The data in the latter range were obtained at 4 mW so that the luminescence signal would be strong at higher temperatures since the signal is barely noticeable above 80 K for 1 mW. All lines have their usual meaning, however, a new line (~ 2.700 eV) with its phonon replicas begins to emerge at about 28 K and disappears at around 120 K, and the first excited state of FE (i.e., n = 2 of FE (2.8141 eV) at 40 K) becomes visible above 40 K in other samples. Furthermore, exciton recombination dominates near both extremes of the temperature range and all lines appear to combine into a single band above 150 K. These data are of particular interest because it may provide valuable insight on the origin of the elusive blue-light emission in ZnSe.

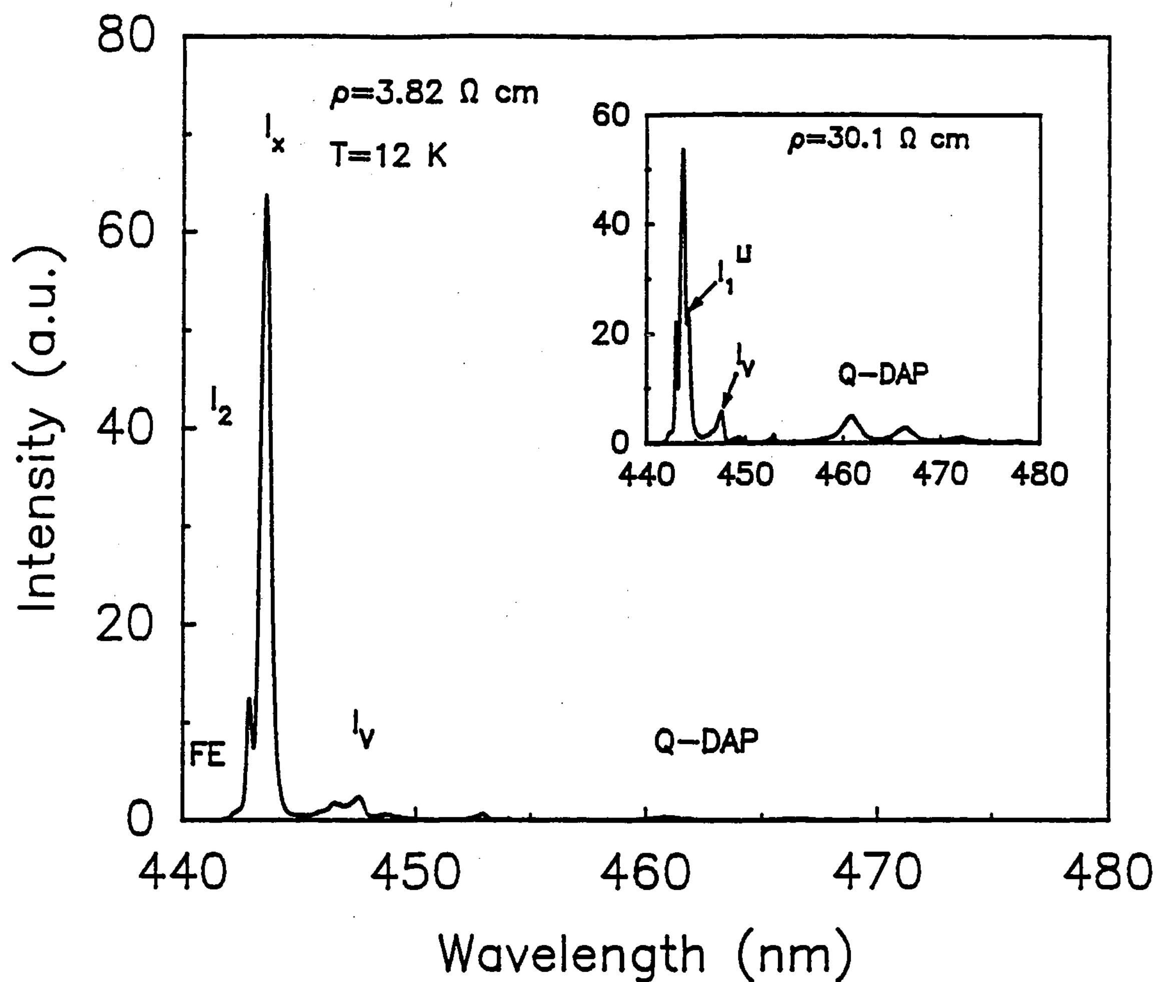

Figure 8. 12 K photoluminescence emission spectrum from a sample of Zn-extracted SPVT ZnSe. The sample resistivity is 3.82 Ω cm. The inset shows the spectrum from a similar sample, but with a resistivity of 30.1 Ω cm. In this spectrum the I_1^{Li} line and Q-series DAP emissions can be clearly seen.

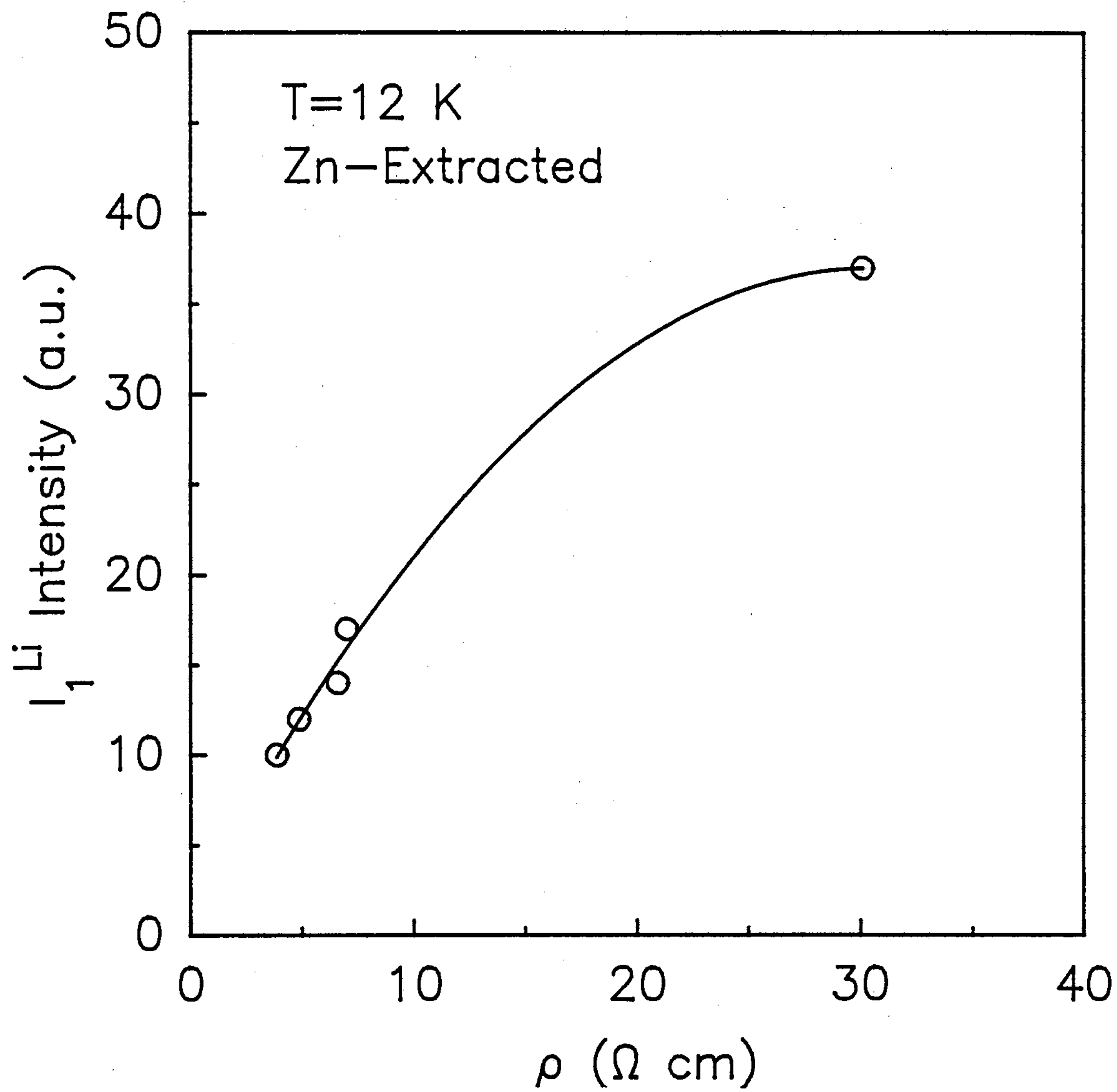

Figure 9. Plot of the intensity of the I_1^{Li} line as a function of resistivity for a Zn-extracted SPVT ZnSe crystal. The solid line is not a fit to a theoretical expression. It only shows how the points may vary with ρ.

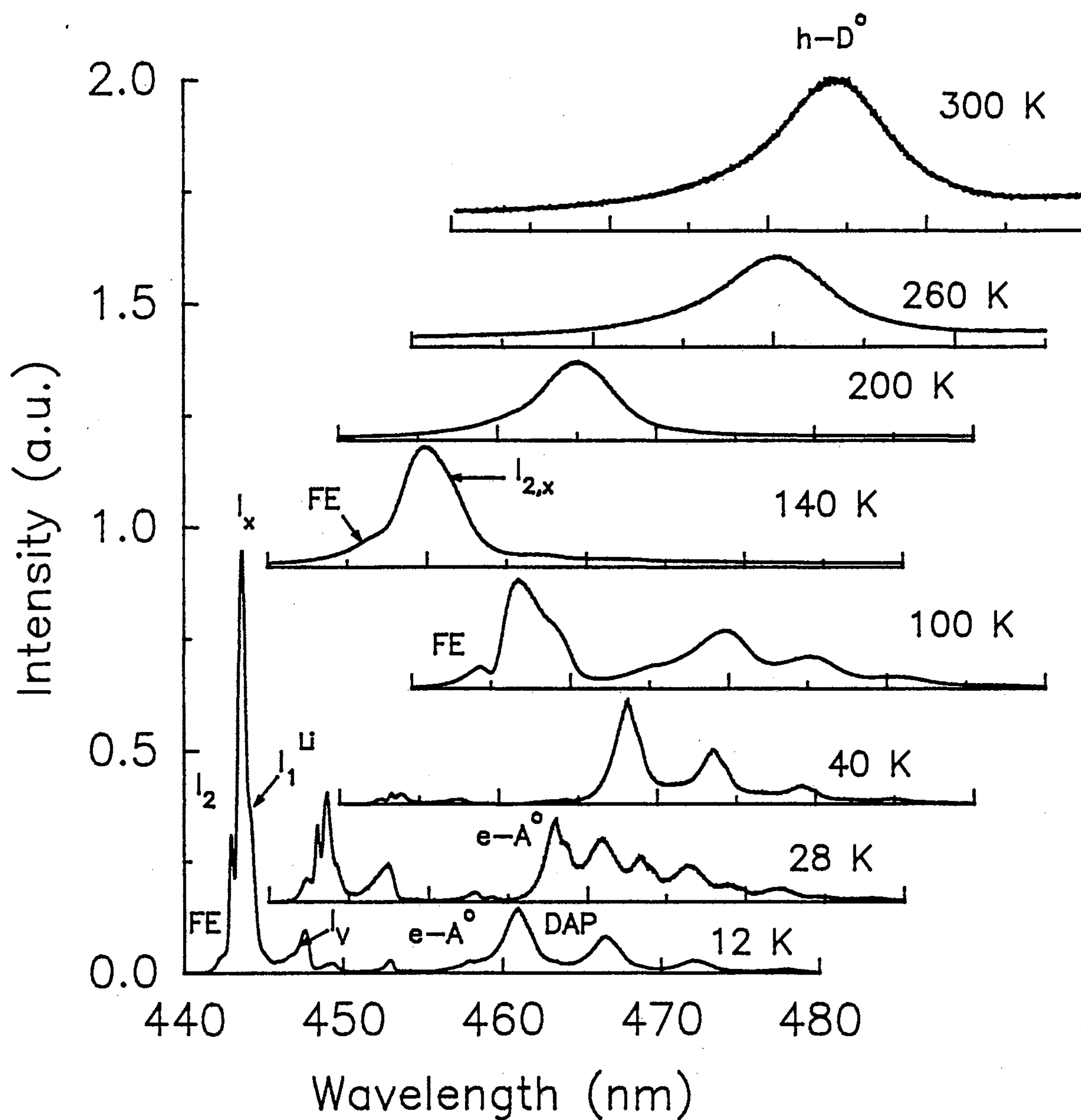

Figure 10. Quenching spectra from the sample with ρ = 30.1 Ω cm shown in the inset of Fig. 8. $I_{2,x}$ represents the combination of I_x and I_2 at higher temperatures and h-D° the room temperature emission. h-D° is believed to start near 200 K.

Similar measurements on as-grown SPVT material were also performed at 4 mW and the end results illustrate that the exciton emission becomes a single band after 150 K.

The data in Fig. 11 demonstrate the temperature dependence of the emission peaks of interest to this work. Quenching of the exciton luminescence is shown in Fig. 10(a) for FE, I_2, I_x, I_1^d and the so-called FE-1LO (or I_V), as obtained from a Zn-extracted and an SPVT sample. Also observed are the lines $I_{2,x}$ (denoted as so for convenience) which is a single line mainly composed of the overlap I_2, I_x and I_V emissions; and h-D^o which is a hole from the valence band recombining with an electron from a donor level occurring at higher temperatures. It is interesting to note that all lines with the exception of h-D^o appear to have a slope equal to that of the FE at high temperatures. This should be expected since dissociation of bound excitons from their defects leave FEs behind as shown by the following reactions

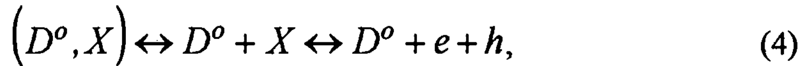

$$\left(D^o, X\right) \leftrightarrow D^o + X \leftrightarrow D^o + e + h, \tag{4}$$

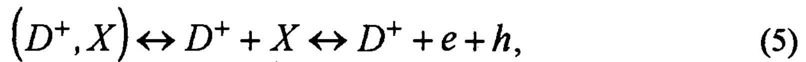

$$\left(D^+, X\right) \leftrightarrow D^+ + X \leftrightarrow D^+ + e + h, \tag{5}$$

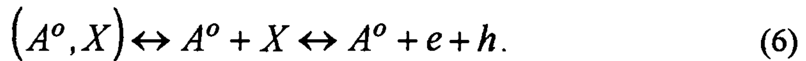

$$\left(A^o, X\right) \leftrightarrow A^o + X \leftrightarrow A^o + e + h. \tag{6}$$

Here D^o, D$^+$ and A^o denote a neutral donor, an ionized donor and a neutral acceptor, respectively; X is the FE, e is a free electron and h is a free hole. At even higher temperatures, X dissociates into free electrons and holes as described by the rightmost reaction in the above expressions. If the FE density is increasing with temperature, then its intensity should increase as well since excitons are formed when they dissociate from impurities. However, the absence of this feature in Fig. 11(a) is a result of the instability of the FE at elevated temperatures, that is, both reactions from each expression are occurring simultaneously, with the rightmost process more dominant. Above 140 K, $I_{2,x}$ and FE begin to merge into a single peak for a while with no clear distinction between them, and

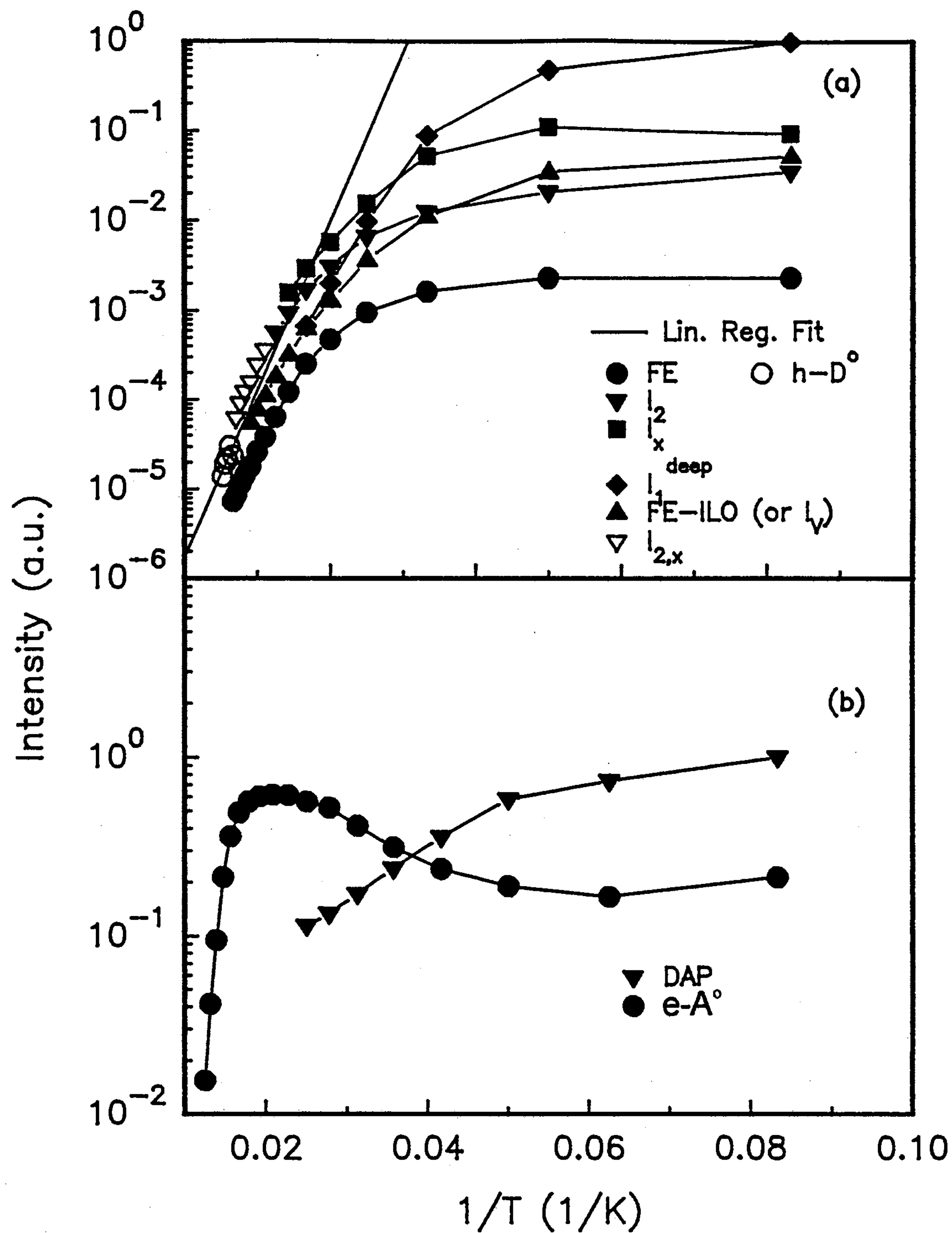

Figure 11. Temperature dependence of the luminescence intensity. (a) Quenching of the exciton emission, and (b) quenching of the edge emission.

then h-D^{o} appears to eventually become predominant above 200 K. Nevertheless, if I_2 is truly an exciton bound to a shallow impurity it would seem likely that h-D^{o} has a contribution that is mostly due to the I_x component. In any case, a peculiar point to be noted here is that h-D^{o} does not follow the FE curve which may indicate that a peak with a higher activation process is present at high temperatures. In Fig. 11(b) are shown quenching of the e-A^{o} and DAP lines characteristic of a Zn-extracted sample. Of interest here is the relationship between the intensities of these emissions as a function of temperature which will be explained in detail later in the Thermal Quenching Discussion section. As the DAP intensity begins to quench more rapidly (at ~ 20 K), the e-A^{o} intensity starts to increase and then quenches near 50 K. The slope of this portion of the curve gives an activation energy of 114 meV, in agreement with Haynes' rule for I_1^{Li}.

Excitation Power Dependence. Figure 12 shows the results of an excitation power-dependent experiment on an SPVT, Zn-extracted ZnSe crystal taken at 12 K. These data are common for each of the Zn-extracted specimens examined in this work and the figure shows the variation in the intensity of the emission as a function of excitation power from the laser beam. Several features are to be noted from the spectra. At very low powers (i.e., 3-10 μW), the DAP and exciton emission intensities are comparable with each other. As the power increases the DAP emission increases along with the exciton emission and with further increase in beam intensity the exciton emission begins to dominate the entire spectrum and becomes strong at high powers. At this point, some broadening is seen in the emission lines which may be a result of heating at the sample surface.

From the spectra in Fig. 12, the intensity of the important peaks are plotted as a function of laser beam power and these are shown in Fig. 13. All slopes were calculated using linear regression. Not shown in the figure are the data for I_V the slope of which is 1.28, which is dramatically different from that for the FE line. It can be seen that all lines

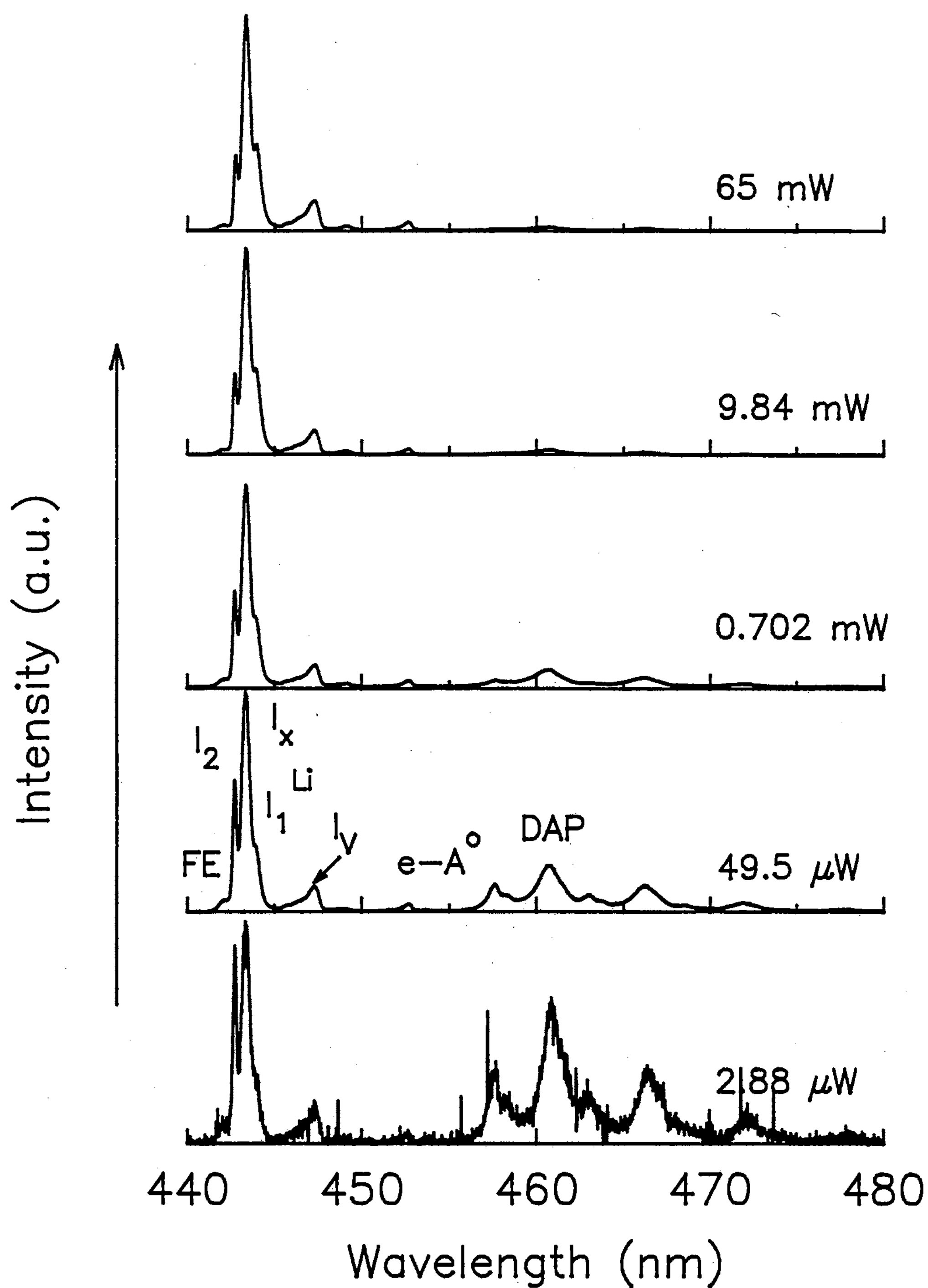

Figure 12. Excitation power-dependent data from a sample of Zn-extracted SPVT ZnSe at 12 K. The intensity arrow indicates the increase in luminescence intensity as a function of laser beam power.

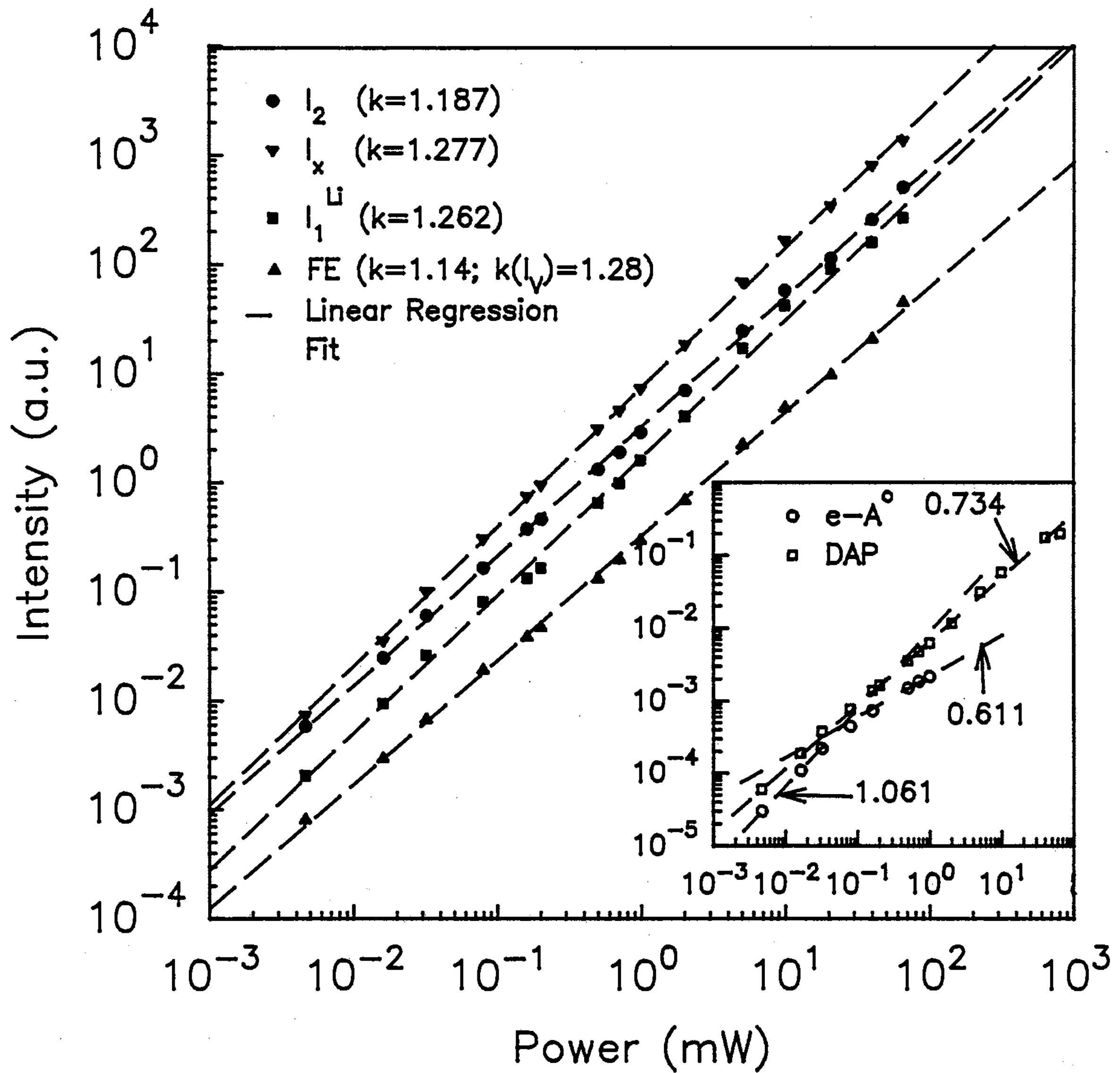

Figure 13. Plot of the luminescence intensity vs excitation power for the main lines of interest to this work. The inset shows the power dependence on the edge emission region. All slopes were calculated using linear regression. The slope of I_V (so-called FE-1LO) is given in the figure without the data.

except the DAP and part of the e-A^o emission have slopes greater than one whereas these two emissions have slopes less than one (refer to the inset). Strong e-A^o emission is necessary in order to reliably monitor its power dependence. This emission is possible to attain by holding the sample temperature at 45 K. Unlike the other lines presented in the figure, the e-A^o emission has two power-dependent regions—one at low powers with a slope near 1.061 and the other at higher powers with a slope of 0.611. This type of behavior in e-A^o and DAP emission have been observed for CdTe crystals studied in our laboratory, and from studies reported elsewhere.[44] Some Zn-extracted samples showed excitonic-emission slopes slightly greater than the values calculated in Fig. 13. Other samples prepared in different ways displayed a variation in slope values for the exciton emission.

Stress Dependence. More PL studies were necessary to further establish the nature of the transitions giving rise to I_x and I_V. The effects of strain on the exciton emission can yield much insight on band structure-related parameters such as deformation potential constants and the identity of radiative recombination mechanisms. Uniaxial stress measurements were carried out to obtain this information. Figure 14 illustrates the spectrum of a chemi-mechanically polished, thin SPVT sample of thickness 0.0123 in (310 μm) which was mounted with a film of Si grease. Besides the slight built-in strain typical of these materials is an additional undeliberate strain resulting from the contraction of the grease upon cooling. The overall effect is to cause splitting of the exciton emission into heavy- and light-hole components of FE as denoted by FE^{hh} and FE^{lh}, respectively. The lines at 2.7965 and 2.7949 eV are labeled as I_2^{Ga} and I_x, and are not the heavy- and light-hole components of I_2 as frequently noted.[45] (The assignments of these lines will be explained later.) Emissions due to the usual I_1^d, e-A^o and DAP are also shown in the figure. For the first time (as far as the author is aware), in Figure 15 are shown spectra obtained from a stress-dependent experiment on an SPVT, Zn-extracted sample. The figure

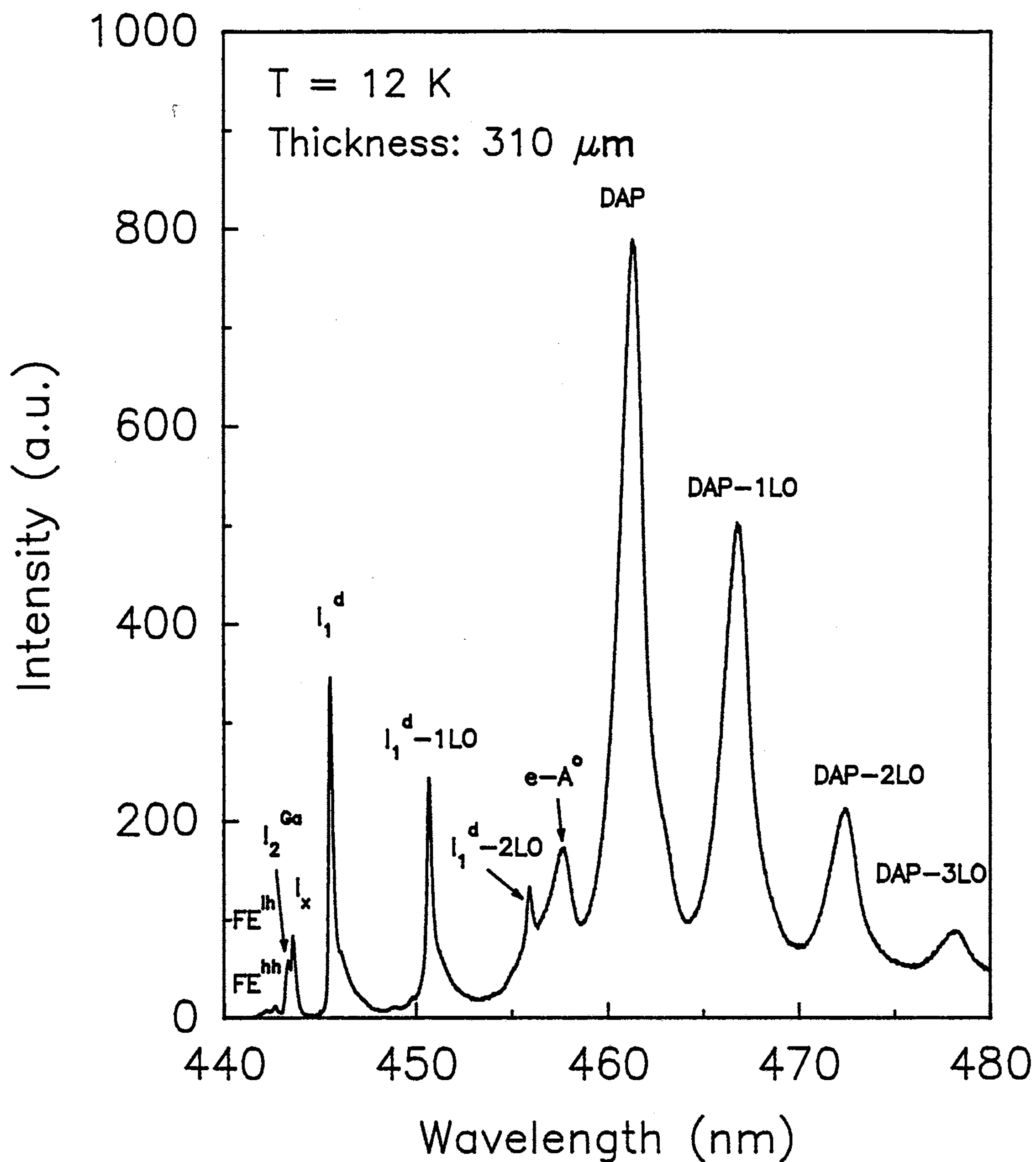

Figure 14. Exciton and edge luminescence from a chemi-mechanically treated SPVT sample. FE splitting is observed due to the manner in which the specimen was mounted and due to the undeliberate built-in strain.

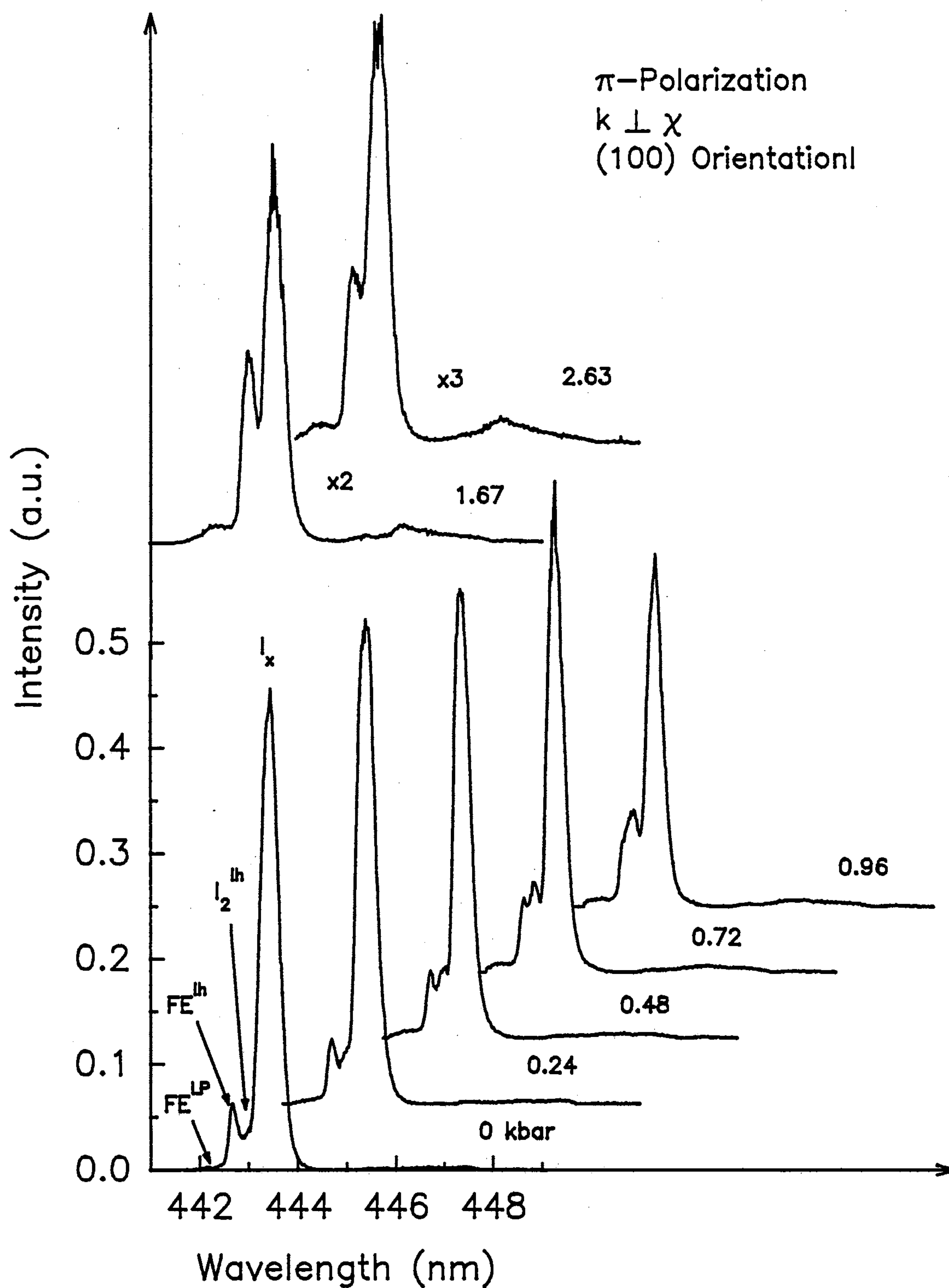

Figure 15. Plot of the stress dependence of the exciton emission with the luminescence signal polarized parallel to the direction of applied stress. The k-vector of the laser beam was perpendicular to the direction of applied stress ($k \perp \chi$).

illustrates the change in energy and intensity of the emission lines as a function of applied stress along the [100] crystal direction. The results were acquired with the luminescence signal π- and σ-polarized to the direction of applied stress. First of all, it should be noted that at zero stress, the π- and σ-luminescence spectra show identical structure with the latter weaker in intensity and with the exclusion of FE^{LP} (the lower polariton branch of FE to be explained later). Fitting of the "stress-free" (i.e., unintentional stress) spectra reveal the following energy assignments: FE^{LP} at 2.8032 eV, FE^{lh} at 2.8008 eV, I_2^{lh} at 2.7991 eV and I_x at 2.7955 eV. Upon the application of a stress field, the weak components (i.e., FE^{LP} and I_2^{lh}) begin to grow in intensity and become quite visible at 0.72 kbar, as shown in Fig. 15 for π-polarization. In addition, a broad component near 2.778 eV starts to increase in intensity as well. For π-polarization, further increase in stress makes I_2^{hh} and I_2^{lh} merge with FE^{lh}, and form a single peak. For the σ-emission case in Fig. 16, the introduction of two new lines are seen with an increase in applied stress, FE^{hh} and I_2^{hh}. (Assignments of all peaks are discussed in a later section.) Again, an initial growth of the emission intensities is also observed with increasing stress for σ-polarization. Other samples were studied with π and σ-excitation, and with different permutations of π- and σ-excitation and π- and σ-emission, and demonstrated similar features. All samples collapsed in the stress apparatus at stresses near 4 kbar, consistent with values reported in the literature.[43]

Absorption Spectra

Figure 17 shows temperature-dependent spectra of the absorption peaks near the band edge for a Zn-extracted specimen. A scaling factor has been used on the vertical axes to separate the curves for illustrative purposes. These are 1.5 for 45 and 100 K, 1.7 for 150 K, 1.8 for 250 K and 2 for 290 K. As with the PL thermal quenching case, these data were recorded between 12 and 300 K and show the thermal behavior of FE (2.8015 eV at

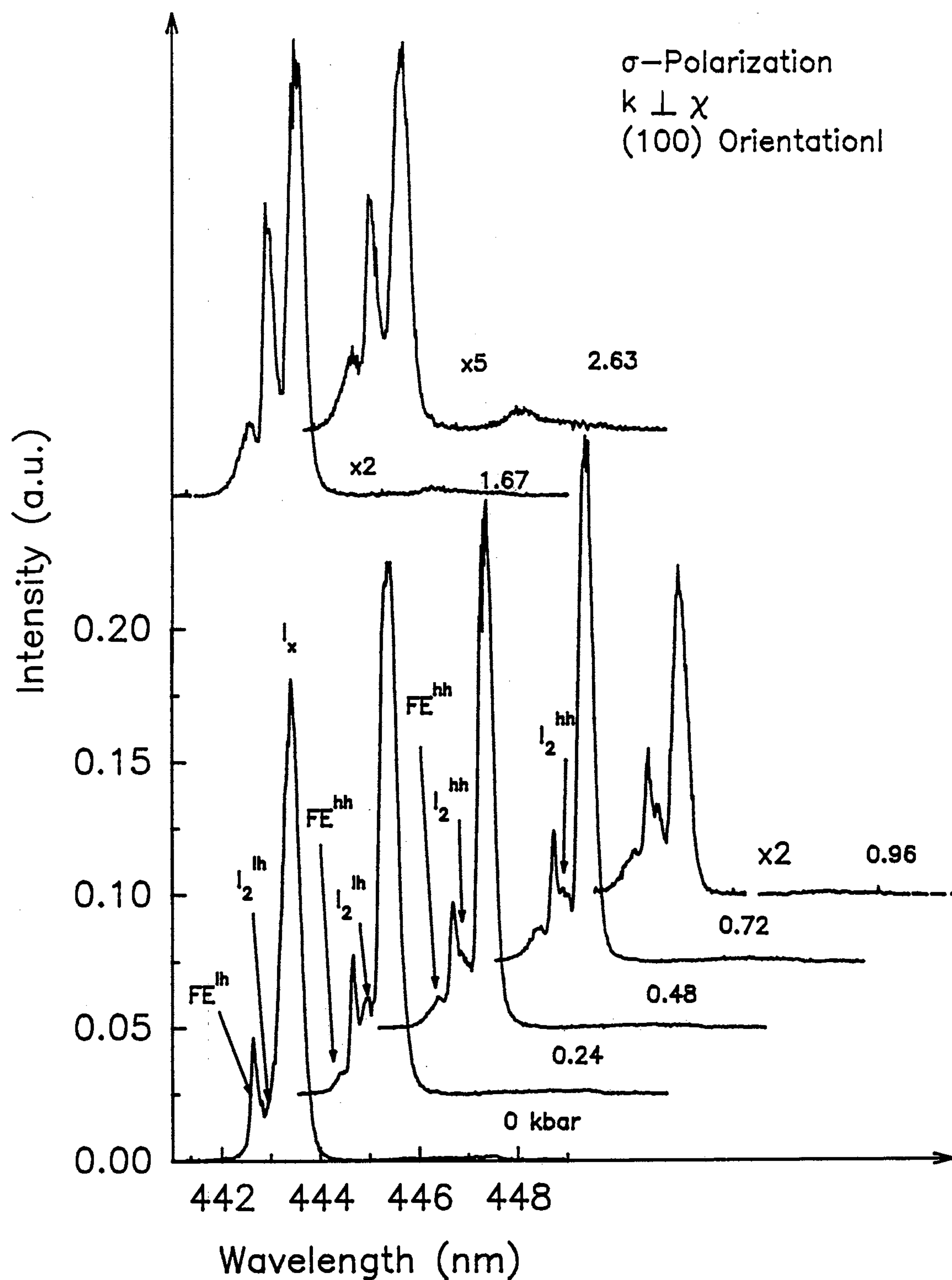

Figure 16. Plot of the stress dependence of the exciton emission with the luminescence signal polarized perpendicular to the direction of applied stress. The FE^{hh} and I_2^{hh} lines are introduced due to σ-polarization.

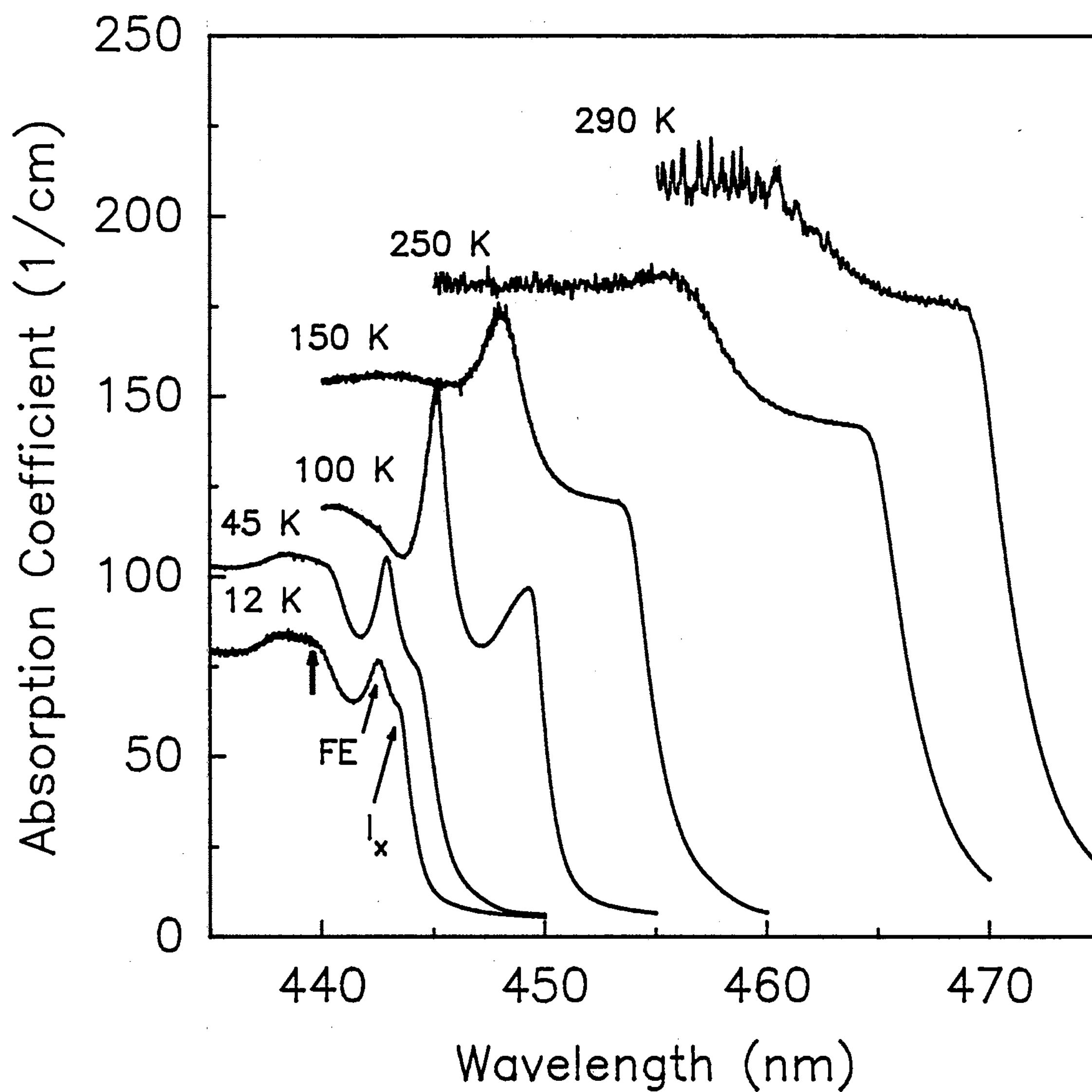

Figure 17. Temperature variation of the band edge (vertical arrow)and free exciton absorption peak for SPVT ZnSe with $\rho = 30.1$ Ω cm. Each absorption curve has been multiplied by a scaling factor for clarity (see text).

12 K) and DBE (i.e., I_x at 2.7962 eV). Most notably, the FE absorption peak increases attaining a maximum at about 90 K, but then decreases as the temperature is raised further. This is due to the increase in FE density from the dissociation of bound excitons followed by the dissociation of FEs since the binding energy of the latter process is comparable to the Fröhlich interaction with LO phonons at high temperatures. Similar observations have been reported for MOCVD-ZnSe in a strain-free environment with a FE energy at 2.7923 eV at 80 K(2.7917 eV from this work at 80 K).[46] However, their results did not show a shoulder (denoted here as I_x) on the lower energy side of the FE as observed in the present work. A broad band starting at 2.8182 eV (n = 2 of FE) at 12 K and extending to 2.8344 eV is seen in the figure. It is worth emphasizing that although the band edge is at E_g(12 K) = 2.8225 eV (the vertical arrow in the figure), this broad band occurs below and above E_g. The origin of this feature is unclear at present but could be due to strain-related effects from the valence band that might have been induced by the Si grease holding the sample, or to transitions from bands other than those at the Γ point. The structure at and near the absorption edge was similar for other Zn-dip treated materials, the difference being that the higher resistivity samples displayed a gradual decrease (as opposed to abrupt seen in the lower resistivity samples) in absorption at the band edge—possibly due to the presence of an ABE. A band due to I_1^d was evident as a small shoulder at the onset of the absorption edge in the SPVT as-grown specimens.

Illustrated in Fig. 18 is the temperature dependence of the position of the FE absorption line, and this is accompanied by some of the PL transitions observed in the Zn-extracted sample from Fig. 8. The position of all emission lines seem to track the FE absorption peak except for h-D^o. Also shown is the temperature dependence of the bandgap as obtained by Shirakawa and Kukimoto[47] for comparison. The agreement between both results is good.

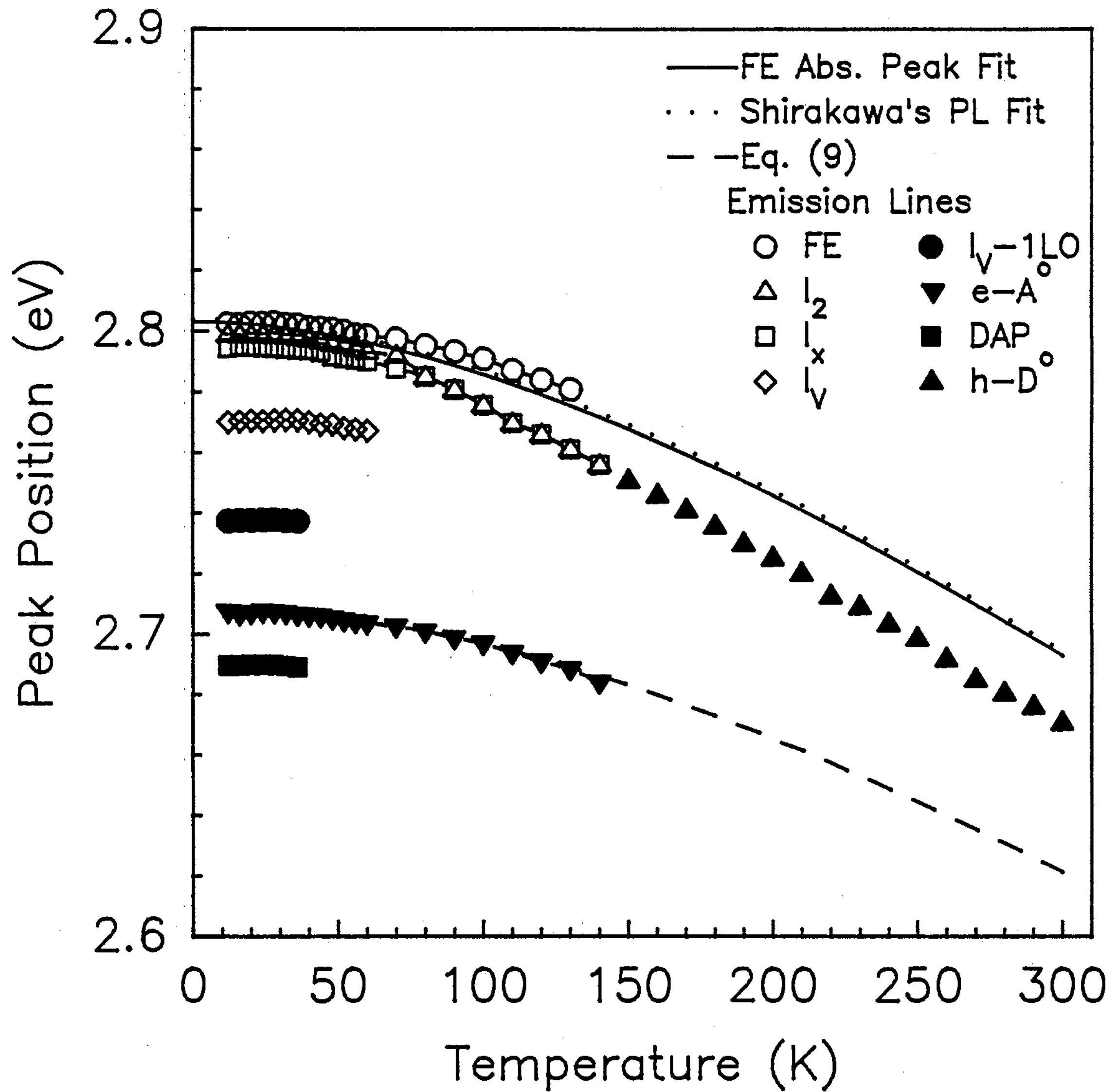

Figure 18. Temperature dependence of the FE absorption line and various PL lines for a Zn-extracted SPVT ZnSe sample. The data points of I_2 and I_x overlap begining at about 70 K and the overlap has been labeled as $I_{2,x}$ in the text.

Thermal Quenching Discussion

The temperature dependence of the bandgap (E_g) is often an important material parameter to know in device fabrication. It critically determines the variation of the photon energy of the laser emission with temperature.[48] It is also important in determining the ionization energies of localized defect states which can either severely degrade or enhance device performance depending upon whether it is a deep level or shallow state. The typical expression used to describe the bandgap variation with temperature has the general form[49]

$$E_g(T) = E_g(0) - \frac{\alpha^* T^2}{(T+\beta)} \tag{7}$$

where $E_g(0)$ is the bandgap energy at 0 K, α^* (asterisk used to differentiate from α, the expansion coefficient) is an empirical parameter and β is an empirical parameter often near the Debye temperature. Fitting the temperature dependence of the FE absorption peak position (Fig. 17) to Eq. (7) gives $\alpha^* = 8.625 \times 10^{-4}$ eV/K and $\beta = 374.7$ K. The value of β is very near the Debye temperature, $\theta = \hbar\omega/k_B = 360$ K, which supports the credibility of these parameters. This result is unlike the value of β (= 405 K) obtained from Shirakawa and Kukimoto[47] for crystals heat-treated in a Zn vapor atmosphere. However, their value of α^* ($=8.59 \times 10^{-4}$eV/K) is in good agreement with the result from this work. Eq. (7) was applied in a temperature range between 12 and 290 K. In the case of temperatures higher than θ_D, β should be approximately $3/8\theta_D$.[50]

Edge Emission. The mechanism responsible for quenching the e-A^o transition is due to the thermal release of holes from the Li acceptor state into the valence band with an activation energy of E_v + 114 meV as calculated from the Arrhenius plot (i.e., taking the slope of e-A^o at high temperatures and setting it equal to E_A/k_B) in Fig. 11 (b). Sometimes using the Arrhenius plot can lead to errors in obtaining the activation energy since the

intensity of each e-A^o peak is easily influenced by the smallest fluctuation in the excitation source. Another more reliable way to determine E_A is to monitor the variation in the position of the e-A^o emission peak as a function of temperature since the change in position is not as strongly dependent as the change in intensity for small power fluctuations, as shown in Fig. 18. Ignoring the electron-phonon coupling and any other type of lattice interaction that may produce broadening, E_A is obtained with help from Eagle's formula describing the line shape of e-A^o transitions[51]

$$G(\hbar\omega) = C(\hbar\omega - E_g - E_A)^{1/2} e^{-(\hbar\omega - E_g - E_A)/k_B T} \quad (8)$$

where C is a constant, E_A is the acceptor binding energy and $\hbar\omega$ is the photon energy. The square root term represents the density of states for parabolic bands and the exponential describes Maxwell-Boltzmann statistics. This equation is applicable for effective-mass impurity states and was derived in the low temperature approximation. Differentiating Eq. (8) with respect to $\hbar\omega$ gives

$$E_{e\text{-}A^o} = \hbar\omega = E_g(T) - E_A + \frac{kT}{2} \quad (9)$$

where $E_g(T)$ is given by Eq. (7) and $k_BT/2$ is the kinetic energy of the electron in the conduction band before recombining with the hole from the Li acceptor state. Fitting the temperature dependence of the e-A^o emission gives a value of 114.4 meV for the Li acceptor level, in excellent agreement with the value of 114 meV from the Arrhenius plot. The variation in emission energy of e-A^o as a function of temperature indicates that the edge emission follows the bandgap which is consistent with shallow donors and acceptors since the impurity wavefunctions are highly localized in k-space. This is because the near-free electrons and holes will each have properties characteristic of the conduction and valence bands, respectively and should therefore follow them.

The mechanism describing the interplay between the temperature dependence of the Q-series DAP (here called DAP1 from now on) and e-A^{o} emission intensities (refer to Fig. 11) is as follow. As the temperature is raised, the donors start to ionize and the DAP1 emission intensity begins to decrease. At the same time, the e-A^{o} peak shows initially an unexpected decrease in intensity. This anomalous quenching behavior has been interpreted as the temperature dependence of competing nonradiative recombination rates, and other radiative recombination mechanisms not associated with the DAP1 and e-A^{o} luminescence transitions.[52] When electrons are donated to the conduction band, the e-A^{o} transition becomes more probable as a result of the increased density of donated electrons. With further temperature increase, the thermal ionization of the acceptors begins to occur thus giving an abrupt drop in the e-A^{o} emission intensity. Since the DAP1 emission intensity decreases due to thermal ionization of the donors, then one should be able to calculate the activation energy by taking the slope of the straight line portion (higher temperature region of the curve) from the DAP1 quenching curve. This yields a value of 6 meV which does not conform to the effective-mass value of 29.2 meV (Table I). Such a low value has been noted before and it has been suggested that it is due to the temperature dependence of the capture cross section for an excited state of the donor,[27] as has been used to describe similar phenomena of DAP1 luminescence in GaP.[53]

Exciton Emission. The quenching spectra show some interesting features, as depicted in Fig. 11(a). All lines appear to follow the quenching of the FE emission intensity (i.e., the slope of each bound exciton line is the same as that of FE) at high temperatures since the bound excitons are simultaneously loosing FEs because of FE dissociation and because of the dissociation of the FE from the defects. Errors in calculating the binding energy of FE comes from setting the slope from the Arrhenius plot to E/k_B. FEs are free electron-hole pairs bound by the coulombic interaction so the expression to calculate the binding energy should contain terms that are characteristic of

the effective density of states from the conduction and valence bands, i.e., a $T^{3/2}$ dependence. Thus, such an expression to fit free or bound excitons is given by[54]

$$\frac{I(T)}{I(0)} = \frac{1}{1+CT^{3/2}e^{-E_i/k_BT}} \tag{10}$$

where $E_i = E_x + E_b$ is the sum of the binding energies of the free exciton (E_x) and bound exciton (E_b), and C is a constant containing the effective mass parameter. Fitting Eq. (10) to the FE quenching curve gives E_x = 20.23 meV. This value is in very good agreement with 20 ± 1 meV found in the published literature.[55] Adding the FE emission energy to E_x yields a value for the bandgap of 2.8225 eV (Table I) at 12 K for SPVT ZnSe.

Of interest to this work is the mechanism responsible for the blue-light emission at room temperature (refer to Fig. 10). The temperature dependence of the exciton emission illustrates that I_2 and I_x with binding energies of 3.7 and 7.8 meV, respectively, merge to form a single band above 100 K. Above 150 K, the entire spectrum shows only one band which has been labeled h-D^o. At this temperature all exciton emission (except for an apparently small contribution from the FE and I_v lines) are annihilated and the weak, although still visible h-D^o band at 2.67 eV persists at room temperature. The high energy tail of the broad peak is due to electrons following a Maxwell-Boltzmann distribution law of the form $\exp(-E/k_BT)$ and is characteristic of FEs. Based solely on this, one would be tempted to assign the band to recombination of FEs. However, close examination reveals that the room-temperature bandgap is 2.7080 eV, which gives a FE emission energy of 2.6877 eV after subtracting a binding energy of 20.23 meV. This emission is 17.7 meV higher than the observed h-D^o peak, so recombination due to FE is not a reasonable assignment. Following Zheng and Allen,[56] and Shirakawa and Kukimoto[47] regarding possible (but unlikely) mechanisms for the room-temperature blue emission, the results from this work also suggest that the emission is due to recombination of a donor electron

with a free hole from the valence band (thus h-D^{o} for bound-to-free recombination) where the donor is at E_c - 38 meV. The validity of the donor ionization energy is supported by the value of 38.2 meV obtained from the slope of the temperature variation of the h-D^{o} luminescence intensity depicted in Fig. 11. Further credence of this value is obtained from application of Haynes' rule to the bound exciton line I_x which yields 38.5 meV. It is worth emphasizing that the donor giving rise to the h-D^{o} transition is deeper than typical effective-mass donors of 28 ± 2 meV observed at low temperatures, and is deeper than the calculated value of 27 meV obtained from Shirakawa and Kukimoto. An interesting point to be made is that the temperature dependence of the h-D^{o} peak position does not change at the same rate as that of the bandgap which is expected for deep levels. Another interesting point is that the h-D^{o} emission begins to quench at about 200 K which seems appropriate for deep donor centers. These points support even further the idea of a relatively deep level state involved in recombination. It is conceivable that the donor taking part in the h-D^{o} transition is the same donor giving rise to I_x, which is an exciton bound to a deep neutral donor (discussed below in the next section). Interestingly, Taguchi and Yao[57] did a study on the effects of Se vapor pressure on I_x for MBE-grown, ZnSe/GaAs heteroepitaxial layers and find that the intensity increases with increasing Se vapor pressure. They also studied the temperature dependence and calculated a value for the activation energy of 35.7 meV at high temperatures. Although no definite explanation is presented regarding the chemical identity of I_x, Taguchi and Yao[57] reference a paper on pressure effects which indicate that it is related to a defect complex comprising a Se vacancy (V_{Se}), perhaps in its singly charged state (V_{Se}^{+}).

Eq. (8) implies that the full width at half maximum (FWHM) is in order of k_BT which follows a linear relationship. Fig. 19 shows the temperature dependence of FWHM which is measured from the position of the peak height for each emission. The results clearly illustrate the presence of two processes taking place with increasing temperature. The line labeled exciton has a slope of 0.084 meV/K which is close to the value of k_B

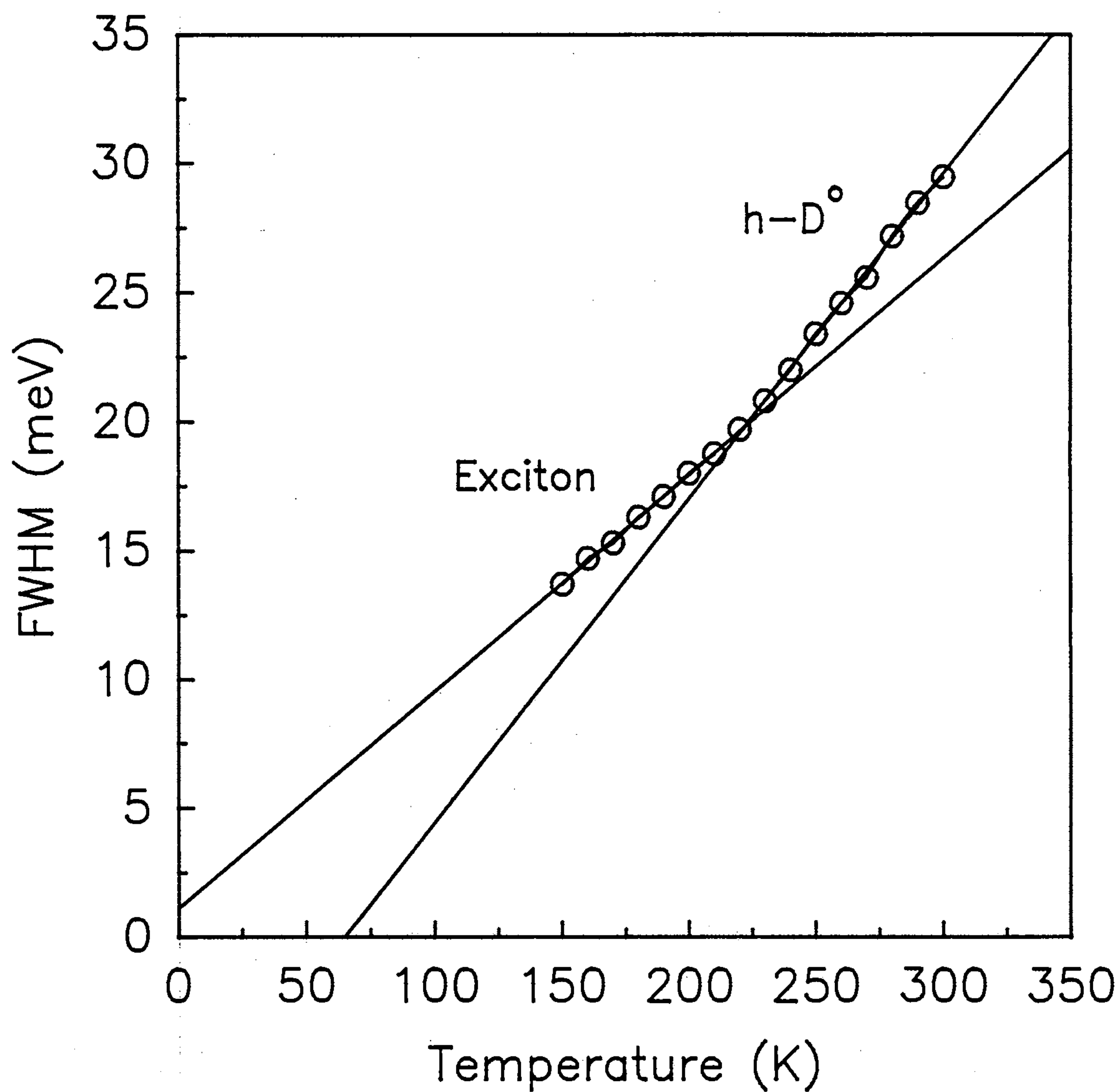

Figure 19. The FWHM change with temperature for the exciton-related band and the h-D° peak for a Zn-extracted, SPVT crystal. The slope for the former peak is 0.084 meV/K whereas for the latter emission line is 0.126 meV/K.

(0.086 meV/K), and the FWHM from this broad peak occurring above 140 K in Fig. 10 is believed to have a substantial contribution from exciton emission. At higher temperatures, the FWHM begins to increase faster with a slope of 0.126 meV/K which may correspond to h-D^o transitions setting in, and is approximately 1.47 times larger (i.e., 3/2k_B) than the exciton slope. The estimated theoretical value for the slope of FWHM from Eq. (8) is near 1.4 k_B. This is in satisfactory agreement with our value of 1.47k_B and it may be due to the gain in kinetic energy of the hole in the band caused by acoustic phonon-assisted (or due to scattering) transitions that become significant at elevated temperatures. The main point to note is that these results verify the existence of the h-D^o line.

In passing, it was stated above that the strongly overlapping I_v line appeared to play a small role in contributing to the intensity of h-D^o at approximately 200 K. At present, I_v is a mystery line and has been claimed to be due to the FE-ILO in the past.[28,29] The identification of such a line is based on the energy separation between FE and I_v which is approximately equal to the LO phonon energy (31.1 meV). Despite this, other factors indicate that it is not the FE-1LO. For example, the usual height of the I_v line is at least twice as high as the FE line with a Huang-Rhys coupling constant between the latter and former lines of 0.1, as previously noted.[30] Moreover, the FWHM of FEs is of the order of k_BT (~ 4 meV) which is much broader than I_v (~ 2 meV).[30] Results from this work show that the origin of I_v is believed to be otherwise and is worthy of mention here. It has been suggested that this line is not the FE-1LO but a defect luminescence band independent of exciton transitions.[30] Quenching results from this study point out that I_v quenches at exactly the same rate as FE at high temperatures although at low temperatures they quench quite differently. This implies that I_v is exciton-related which is inconsistent with the suggestion of defect emission, and is perhaps a bound exciton. The possible assignment of this line as an exciton bound to a deep acceptor has to be treated with caution because then the energy to bind the exciton to the defect would exceed the binding energy of FE (~ 20 meV). This could make the complex unstable and lead to the

"breakup" of FE because of the strong binding by the center. Excitation power-dependent measurements suggest that I_v is also exciton-related and is not the FE-1LO (discussed below). From the data of the peak position versus temperature, I_v and I_v-1LO have the same temperature dependence. However, the low temperature dependence of the FE line barely shifts to low energy faster than these lines, indicating that the mechanisms giving rise to recombination are different for FE and I_v.

Excitation Power-Dependent Analysis

Model for Edge and Exciton Transitions

Since the work of Taguchi *et al.*,[58] who were among the first to develop a rate equation analysis on the exciton and edge emission regions in CdTe, little interest has been generated with the use of this type of analysis to other II-VI semiconductors for identification of radiative recombination processes. Use of a recent study by Schmidt *et al.*[44] encompassing a more complete approach is adopted here and a model is developed to describe the exciton and edge emissions. This will help determine the transitions giving rise to I_x and I_v.

The recombination transitions considered in the model are shown in Fig. 20, and these are free excitons (FE), two donor-bound excitons ($D1^oX$ and $D2^oX$), an acceptor-bound exciton (A^oX), a free-to-bound (e-A^o), a donor-acceptor pair (DAP1) and a bound-to-free (h-D^o). There is no evidence of this latter transition occuring at low temperatures so it will be ignored. Trapping of free carriers by $D1^o$ (ground and first excited state), A^o and $D2^o$ are also considered in the diagram. Φ denotes the generation rate of free electron-hole pairs and is directly proportional to the laser power and a, b, c, d, e, f, g, h, h', i, i', j, and k are the transition rates for each process. The set of coupled differential equations representing the traffic of charge is

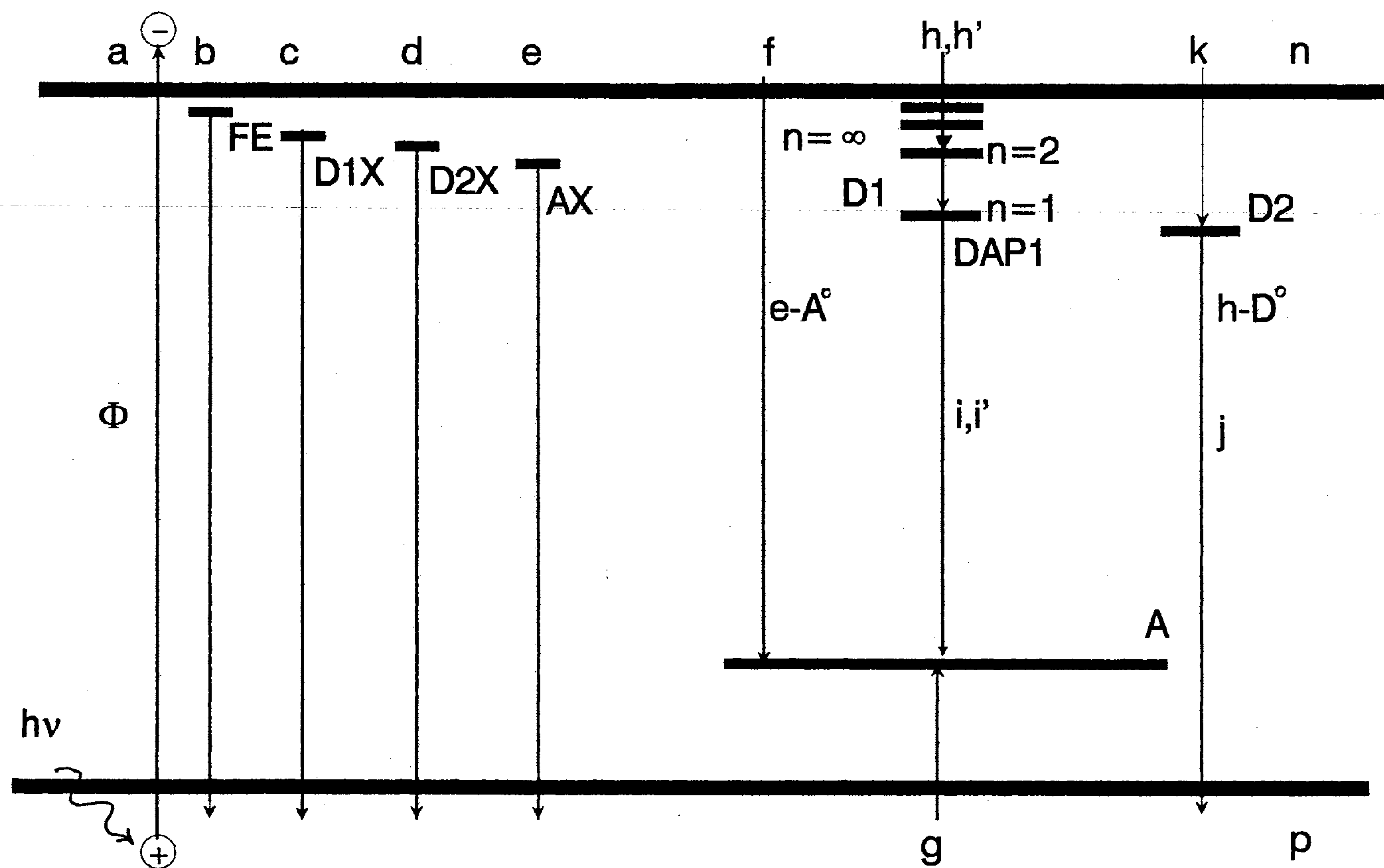

Figure 20. PL transitions used in the model of the rate equation analysis.

$$\frac{dn}{dt} = a\Phi - n^2 b - nfN_{A^o} - nh(N_{D1} - N_{D1^o}) - nk(N_{D2} - N_{D2^o}), \tag{11}$$

$$\frac{dN_{A^o}}{dt} = -nfN_{A^o} + ng(N_A - N_{A^o}) - n_{FE}eN_{A^o} + \frac{N_{A^oX}}{\tau_A} - iN_{D1^o}N_{A^o}, \tag{12}$$

$$\frac{dN_{D1^o}}{dt} = -n_{FE}cN_{D1^o} + \frac{N_{D1^oX}}{\tau_{D1}} + nh(N_{D1} - N_{D1^o}) - iN_{D1^o}N_{A^o} - i'N_{D1^o}N_{A^o} \tag{13}$$

$$\frac{dN_{D2^o}}{dt} = -n_{FE}dN_{D2^o} + \frac{N_{D2^oX}}{\tau_{D2}} + nk(N_{D2} - N_{D2^o}), \tag{14}$$

$$\frac{dN_{D1^oX}}{dt} = n_{FE}cN_{D1^o} - \frac{N_{D1^oX}}{\tau_{D1}}, \tag{15}$$

$$\frac{dN_{D2^oX}}{dt} = n_{FE}dN_{D2^o} - \frac{N_{D2^oX}}{\tau_{D2}}, \tag{16}$$

$$\frac{dN_{A^oX}}{dt} = n_{FE}eN_{A^o} - \frac{N_{A^oX}}{\tau_A}, \tag{17}$$

$$\frac{dn_{FE}}{dt} = bn^2 - \frac{n_{FE}}{\tau_{FE}} - n_{FE}cN_{D1^o} - n_{FE}dN_{D2^o} - n_{FE}eN_{A^o}. \tag{18}$$

In the above equations, n is the electron concentration (p is the hole concentration and np $= n^2$), N_A, N_{D1} and N_{D2} are the total acceptor and donor (of species D1 and D2) concentrations, respectively; N_{A^o} , N_{D1^o} and N_{D2^o} are the neutral acceptor and donor concentrations; N_{A^oX}, N_{D1^oX} and N_{D2^oX} are the concentrations of acceptor- and donor-bound excitons, n_{FE} is the concentration of free excitons and $1/\tau_i = 1/\tau_i + 1/\tau_i^{nr}$ (i = FE, A, D1 or D2) is the total lifetime including radiative and nonradiative terms. The nonradiative recombination processes could be any one of the following: Auger effect, surface recombination, or phonon emission. From the quenching data in Fig. 11, it already

has been explained that the dissociation mechanism for bound excitons results in the generation of free excitons and neutral donors and acceptors. This type of pathway is the one employed and is represented in Eqs. (12)-(18) for each term containing the total lifetime. If free excitons are created directly (i.e., when the excitation energy hν is in resonance with E_g), then a term composed of the transition rate times Φ would be added in Eq. (18). In this work hν > E_g and this term will be neglected. Also, DAP transitions will be ignored for the moment.

Given the many unknowns in Eqs. (11)-(18), it is impossible to solve these equations analytically or numerically, so certain approximations must be made. Since for the excitation power measurements the sample is continuously illuminated creating a steady-state condition for each transition in Fig. 20, then all d/dt's = 0. Thus Eq. (11) gives

$$a\Phi = n^2 b + nfN_{A^\circ} + nh(N_{D1} - N_{D1^\circ}) + nk(N_{D2} - N_{D2^\circ}). \qquad (19)$$

Two power regimes can be considered, one at high Φ and the other at low Φ. It will be assumed that the concentrations of N_{A°, N_{D1° and N_{D2° are independent of Φ at low Φ. The first term in Eq. (19) describes free exciton recombination, the second term describes the e-A^o transition, and the third and fourth terms represent trapping of the electron by the ionized donors D1 and D2.

At low Φ, nN_{A° is small with respect to n^2 and the e-A^o transition along with the trapping terms become dominant, and Eq. (19) becomes $\Phi \approx nfN_{A^\circ} + nh(N_{D1} - N_{D1^\circ}) + nk(N_{D2} - N_{D2^\circ})$ or

$$n \propto \Phi \qquad (20)$$

At high Φ, n^2 is large with respect to nN_{A° and the free exciton term in Eq. (19)

survives while the e-A° and the trapping terms are neglected. Eq. (19) takes the form $\Phi \approx n^2 b$ or

$$n \propto \Phi^{1/2}. \tag{21}$$

Eqs. (20) and (21) simply show the dependence of the free carrier concentration on the generation rate. The intensities of the exciton and edge emissions are described below provided they are proportional to the transition rates, *viz*

$$I_{FE} = \frac{n_{FE}}{\tau_{FE}} = bn^2 + n_{FE}cN_{D1^o} - n_{FE}dN_{D2^o} - n_{FE}eN_{A^o}, \tag{22}$$

$$I_{D1^o X} = \frac{N_{D1^o X}}{\tau_{D1}} = n_{FE}cN_{D1^o}, \tag{23}$$

$$I_{D2^o X} = \frac{N_{D2^o X}}{\tau_{D2}} = n_{FE}dN_{D2^o}, \tag{24}$$

$$I_{A^o X} = \frac{N_{A^o X}}{\tau_{A}} = n_{FE}eN_{A^o}, \tag{25}$$

$$I_{e-D^o} = nfN_{A^o}, \tag{26}$$

$$I_{DAP1} = iN_{D1^o}N_{A^o}, \tag{27}$$

$$I_{DAP1_{n=2}} = i'N_{D1_{n=2}^o}N_{A^o}. \tag{28}$$

In order for Eqs. (23)-(28) to be useful in the data analysis, they must be written in terms of the natural logarithm with respect to Φ because we are interested in the slope of the ln-ln plots. Assuming that the transition rates are weakly dependent on Φ, and using Eq. (22)

$$\frac{d\ln I_{D1^oX}}{d\ln \Phi} = \frac{d\ln I_{FE}}{d\ln \Phi} + \frac{d\ln N_{D1^o}}{d\ln \Phi}, \tag{29}$$

$$\frac{d\ln I_{D2^oX}}{d\ln \Phi} = \frac{d\ln I_{FE}}{d\ln \Phi} + \frac{d\ln N_{D2^o}}{d\ln \Phi}, \tag{30}$$

$$\frac{d\ln I_{A^oX}}{d\ln \Phi} = \frac{d\ln I_{FE}}{d\ln \Phi} + \frac{d\ln N_{A^o}}{d\ln \Phi}, \tag{31}$$

$$\frac{d\ln I_{e-A^o}}{d\ln \Phi} = \frac{d\ln n}{d\ln \Phi} + \frac{d\ln N_{A^o}}{d\ln \Phi}, \tag{32}$$

$$\frac{d\ln I_{DAP1}}{d\ln \Phi} = \frac{d\ln N_{D1^o}}{d\ln \Phi} + \frac{d\ln N_{A^o}}{d\ln \Phi}, \tag{33}$$

$$\frac{d\ln I_{DAP1_{n=2}}}{d\ln \Phi} = \frac{d\ln N_{D1^o_{n=2}}}{d\ln \Phi} + \frac{d\ln N_{A^o}}{d\ln \Phi}. \tag{34}$$

In deriving the results shown in Eqs. (33) and (34), it has been assumed that i and i' are independent of Φ. In steady-state, $dN_{D1^o}/dt = dN_{D2^o}/dt = dN_{A^o}/dt = 0$ which implies that N_{D1^o}, N_{D2^o} and N_{A^o} are all constants. From Eq. (22)

$$bn^2 = n_{FE}\left(\frac{1}{\tau_{FE}} - cN_{D1^o} - dN_{D2^o} - eN_{A^o}\right) \tag{35}$$

and

$$n \propto n_{FE}^{1/2} \propto I_{FE}^{1/2} \tag{36}$$

where the second proportionality relation comes from Eq. (22). Given $I_{FE}(\Phi)$, $I_{D1^oX}(\Phi)$, $I_{D2^oX}(\Phi)$, $I_{A^oX}(\Phi)$, $I_{e\text{-}A^o}(\Phi)$, $I_{DAP1}(\Phi)$ and $I_{DAP1n=2}(\Phi)$, from a set of excitation power measurements, Eqs. (29)-(34) can be used in conjunction with Eqs. (20)-(22) and Eq. (36) to check whether there is agreement between experiment and the model. Since the

rate of charge carrier traffic changes as the laser power is varied, N_{D1^o}, N_{D2^o} and N_{A^o} change as well. Two assumptions can be made regarding the dependence of impurity concentration on Φ. The first one is that at low powers N_{D1^o}, N_{D2^o} and N_{A^o} are independent of Φ; and at high powers N_{D1^o}, N_{D2^o} and N_{A^o} depend on Φ.

At low Φ, N_{D1^o}, N_{D2^o} and N_{A^o} are all constant with respect to Φ and the slopes from the power dependence of Eqs. (29)-(31) all follow that of I_{FE} (i.e., $d\ln I_{FE}/d\ln\Phi \approx 1$). Furthermore, in this regime, Eqs. (32), (33) and (34) take on the form with the help of Eq. (20)

$$\frac{d\ln I_{e-A^o}}{d\ln\Phi} = 1, \tag{37}$$

$$\frac{d\ln I_{DAP1}}{d\ln\Phi} = \frac{d\ln I_{DAP1_{n=2}}}{d\ln\Phi} = 0. \tag{38}$$

At high Φ, however, N_{D1^o}, N_{D2^o} and N_{A^o} all depend on Φ. This can be viewed easily by considering the following reactions:

$$D1^o \leftrightarrow D1^+ + e^-, \tag{39}$$

$$D2^o \leftrightarrow D2^+ + e^-, \tag{40}$$

$$A^o \leftrightarrow A^- + h^+, \tag{41}$$

where $D1^o$ and $D2^o$ are neutral donor atoms, $D1^+$ and $D2^+$ are ionized donors, A^o is a neutral acceptor and A^- is an ionized acceptor. As the e^- and h^+ concentrations (i.e., n and p) increase due to the excitation source, the above chemical equilibria are pushed to the left. As a result, N_{D1^o}, N_{D2^o} and N_{A^o} all increase with Φ; and $d\ln N_{D1^o}/d\ln\Phi$, $d\ln N_{D2^o}/d\ln\Phi$ and $d\ln N_{A^o}/d\ln\Phi$ are greater than zero. This means that $d\ln N_{D1^oX}/d\ln\Phi$, $d\ln N_{D2^oX}/d\ln\Phi$ and $d\ln N_{A^oX}/d\ln\Phi$ are greater than $d\ln I_{FE}/d\ln\Phi$ as described by Eqs. (29)-(31). At high Φ, $n \propto \Phi^{1/2}$, then

$$\frac{d\ln I_{e-A^o}}{d\ln \Phi} = 0.5 + \frac{d\ln I_{A^oX}}{d\ln \Phi} - \frac{d\ln I_{FE}}{d\ln \Phi}, \tag{42}$$

$$\frac{d\ln I_{DAP1}}{d\ln \Phi} = \frac{d\ln I_{A^oX}}{d\ln \Phi} + \frac{d\ln I_{D1^oX}}{d\ln \Phi} - 2\frac{d\ln I_{FE}}{d\ln \Phi}, \tag{43}$$

$$\frac{d\ln I_{DAP1_{n=2}}}{d\ln \Phi} = \frac{d\ln I_{A^oX}}{d\ln \Phi} + \frac{d\ln I_{D1^o_{n=2}X}}{d\ln \Phi} - 2\frac{d\ln I_{FE}}{d\ln \Phi}. \tag{44}$$

In order to use Eq. (44), information for a transition of an exciton bound to the first excited state of the donor would be needed however, this line is lacking from the PL measurements. For the case of h-D^{o} (bound-to-free) transitions, the equation has the same form as Eq. (42), *viz*

$$\frac{d\ln I_{h-D^o}}{d\ln \Phi} = 0.5 + \frac{d\ln I_{D2^o}}{d\ln \Phi} - \frac{d\ln I_{FE}}{d\ln \Phi}. \tag{45}$$

Not included in the above rate equation analysis is recombination of an exciton bound to an ionized donor. The equation for such a process would be represented by

$$\frac{dN_{D^+X}}{dt} = n_{FE} l N_{D^+} - \frac{N_{D^+X}}{\tau_{D^+}} \tag{46}$$

and

$$I_{D^+X} = \frac{N_{D^+X}}{\tau_{D^+}} = n_{FE} l N_{D^+} \tag{47}$$

where Eq. (47) is based on steady-state conditions. In the second term of Eq. (46), it has been implicitly assumed that an ionized donor and a free exciton are produced after dissociation of the bound exciton complex. Proceeding further with Eq. (47),

$$\frac{d\ln I_{D^+X}}{d\ln \Phi} = \frac{d\ln n_{FE}}{d\ln \Phi} + \frac{d\ln N_{D^+}}{d\ln \Phi}, \tag{48}$$

$$\frac{d\ln I_{D^+X}}{d\ln\Phi}=\frac{d\ln I_{FE}}{d\ln\Phi}+\frac{d\ln N_{D^+}}{d\ln\Phi}. \quad (49)$$

Considering either equilibrium reaction from Eq. (39) or (40), it can be seen that by increasing Φ the reaction is favored to occur to the left, that is, the concentration of D^+ decreases. Thus, $d\ln N_{D^+}/d\ln\Phi < 0$, and the end result for excitons bound to ionized donors is

$$\frac{d\ln I_{D^+X}}{d\ln\Phi}<\frac{d\ln I_{FE}}{d\ln\Phi} \quad (50)$$

according to Eq. (49) whereas for excitons bound to neutral donors

$$\frac{d\ln I_{D^oX}}{d\ln\Phi}>\frac{d\ln I_{FE}}{d\ln\Phi}. \quad (51)$$

For each ionized donor neutralized, a neutral donor is gained from each neutralization process and

$$\frac{d\ln_{D^o}}{d\ln\Phi}=-\frac{d\ln N_{D^+}}{d\ln\Phi} \quad (52)$$

from $N_D = N_{D^o} + N_{D^+}$ where as mentioned above, N_D is the total concentration of donors. The inequalities given in Eqs. (50) and (51) provide a valuable tool for identification of exciton lines.

Discussion

The model developed above predicts that the e-A^o transition will have a slope of approximately 1 for low Φ. At high Φ, the slopes of e-A^o, DAP1 and $DAP1_{n=2}$ (not calculated) from a low resistivity Zn-extracted sample (.i.e., 30.1 Ω cm) are represented by Eqs. (42)-(44) which are all in terms of measurable quantities. Table II shows a

TABLE II

SLOPE VALUES FOR VARIOUS PL LINES IN A ZN-EXTRACTED SAMPLE

Temp	Φ	Line	Observed	Calculated	Identity
13 K	High	DAP1	0.74	0.17	
	High	$e\text{-}A^o$	0.61	0.62	
	High	ABE	1.26	≥ FE	
	High	DBE	1.19	≥ FE	
	High	FE	1.14	---	
	High	I_x	1.28	≥ FE	D^oX
	High	I_V	1.28	---	A^oX?
45 K	High	$e\text{-}A^o$	0.65	0.70	
	High	ABE	1.49	≥ FE	
	High	DBE	1.32	≥ FE	D^oX
	High	FE	1.29	---	
	High	I_x	1.55	---	D^oX
	High	I_V	1.49	---	A^oX?

comparison between theory and experiment for the 30.1 Ω cm Zn-extracted specimen. First of all, since the DAP1 and the exciton emission intensities are comparable at the lowest power, it is believed that all emissions occur in the high excitation extreme, thus HIGH in the table. As can be seen, it appears that all slope values for exciton emission exhibit only one power-dependent regime at 13 and 45 K. The e-A^o transition on the other hand, has two slopes, one occurring at low powers with a value of 1.06 and the other occurring at high powers with a value of 0.61, and agrees well with the model. However, disagreement is found for DAP1 emission between the observed value of 0.74 and the calculated value of 0.17. The reason for this discrepancy is thought to be due to the radiative recombination rate for DAP1 which seems to have a pronounced power dependence. In retrospect, the Φ-dependence of i (and i' in Eq. (28)) in Eq. (27) can not be ignored for even the weakest excitation power. The magnitude of error involved when i is neglected can be estimated by the following expression for the transition probability, W, for DAP1 recombination,[54]

$$W = W_o e^{-2r_{DA} / a_B^*} \tag{53}$$

or

$$i = BW \tag{54}$$

where B and W_o are constants, r_{DA} is the mean donor-acceptor separation as defined before and a_B* is the effective Bohr radius of the impurity with the larger radius. Combining Eqs. (53) and (54), taking the natural logarithm and differentiating with respect to Φ gives

$$\frac{d \ln i}{d \ln \Phi} = -\frac{2}{a_B^*} \frac{d(r_{DA})}{d \ln \Phi} \tag{55}$$

The left-hand side of Eq. (55) indicates that the transition rate increases with an increase in Φ. $dr_{DA}/d\ln\Phi$ is negative because r_{DA} is a decreasing function with respect to Φ, and the right-hand side of Eq. (55) becomes positive. For a random distribution of pairs in the lattice, r_{DA} can be considered as the radius of a spherical shell containing N_A acceptor impurities of volume $1/N_A = (4\pi/3)r_{DA}^3$. Making use of this relation, and after some mathematical manipulation, and using Eq. (31), Eq. (55) becomes

$$\frac{d\ln i}{d\ln \Phi}=\frac{2}{9N_A^{1/3}a_B^*}\left(\frac{3}{4\pi}\right)^{1/3}\left[\frac{d\ln I_{A^\circ X}}{d\ln \Phi}-\frac{d\ln I_{FE}}{d\ln \Phi}\right] \qquad (56)$$

To see if the above equation gives Eq. (43) a correction in the right order of magnitude, assume $N_A \sim 10^{15}$ cm^{-3} (obtained from the electrical data in the next chapter) and $a_B^* \sim 30$ Å (radius of shallow donor in ZnSe), and with use of Table II, $d\ln i/d\ln\Phi \sim 0.55$ from which Eq. (43) now gives a value of 0.72 for the slope of the DAP1 line versus Φ. In reference to the results of Schmidt *et al.*,[44] and the results quoted therein on other published work, it can be concluded that the transition rate should not be ignored when the DAP1 emission intensity is strongly dependent on the excitation power as is the case in the present study. If the intensity is weakly dependent on the power, then the transition rate can be ignored since the concentration of neutralized impurities increases slowly, thus having a negligible effect on *i*. Justification for these arguments is further supported by the plot of the DAP1 peak position as function of Φ for a Zn-extracted sample shown in Fig. 21. An increase in the DAP1 peak position with Φ is observed due to the increase of the Coulomb interaction between the donor-acceptor pair (or the decrease of r_{DA}). At high Φ, the peak energy seems to decrease possibly due to heat generated at the sample surface.

An odd feature in the Zn-extracted PL spectrum is the presence of the strong bound exciton line, I_x, which was briefly introduced in the Thermal Quenching Section along with I_V. This line has been associated with an exciton bound to an ionized donor in

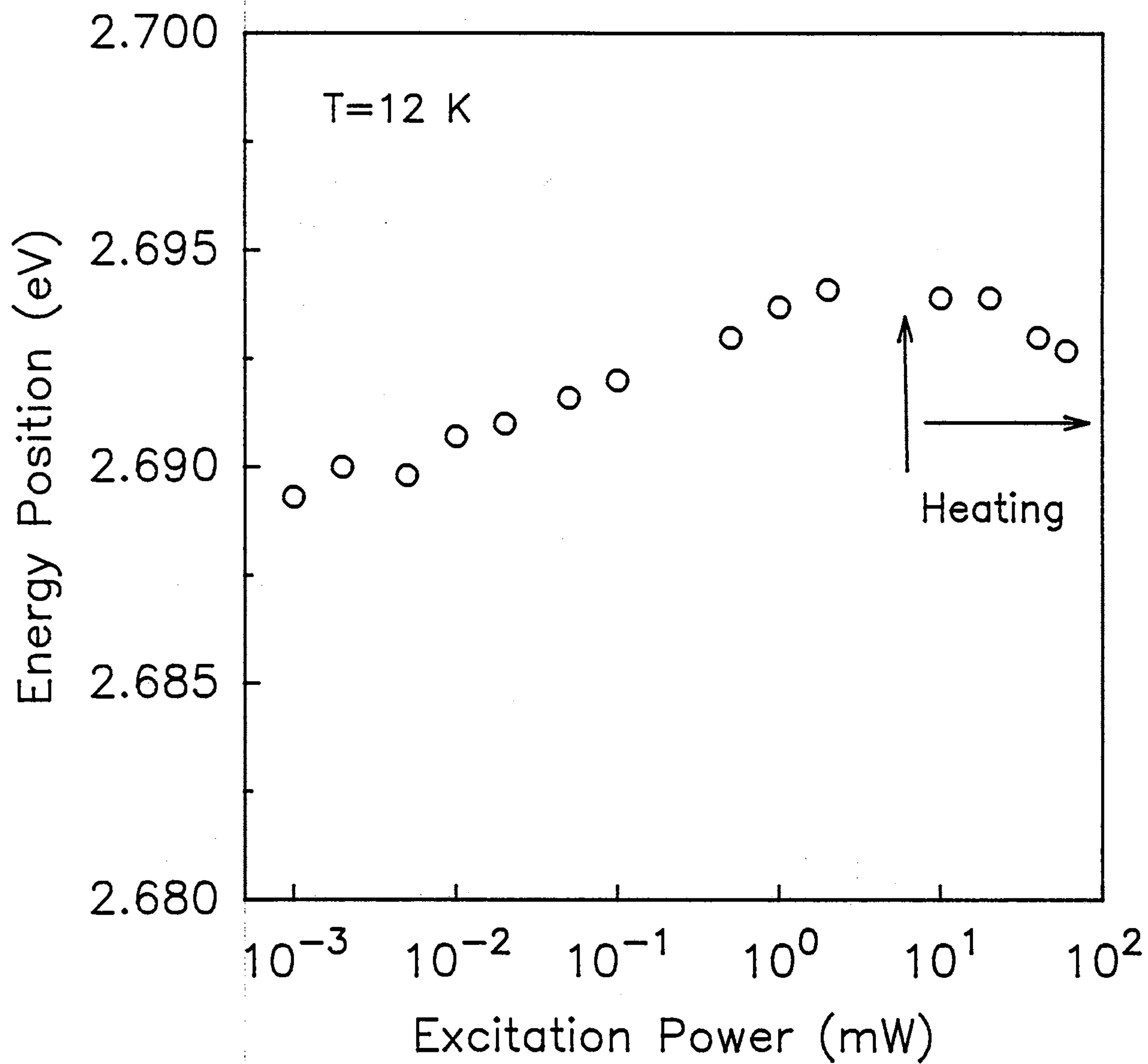

Figure 21. Energy position of the DAP1 emission line versus the excitation power at 12 K from a Zn-dipped sample with ρ = 30.1 Ω cm. The downward shift in energy at high powers is believed to be due to heating from the intense laser beam.

the past. The difficulty with this assignment is that at low temperatures most donors should be neutral since the thermal energy of the lattice is many times lower than the effective-mass donor binding energy (~ 29 meV) despite the material being highly compensated. If this situation is manifested in our samples, then the emission intensity of I_2 should be larger than I_x. Since this is not the case, it seems that recombination leading to the emergence of I_x is due to something other than an ionized donor.

To clarify this, Eq. (50) shows that if the slope of I_x is less than that of I_{FE}, then it is due to an ionized DBE. If I_x involves neutral donors, then the slope of I_{D^oX} should be greater than I_{FE} as indicated by Eq. (51). Examination of the values at 13 K in Table II suggest that I_x is due to a neutral DBE, and the same conclusion is arrived at 45 K. The question whether this donor state is shallow or deep is also a matter of some debate. The temperature variation of the intensity of the DAP1 line illustrates that the donor state involved in this emission quenches at about 20 K as seen in Fig. 11(b). So the existence of I_x above this temperature should not be possible if I_x were due to an exciton bound to the donor giving rise to DAP1 which has been ionized above 20 K.. Since I_x is still observed at 45 K, this line must be due to a neutral DBE of a different specie—maybe a deeper donor. Again, this could be the same donor responsible for the h-D^o transition. Further results on I_x will be presented in the Stress Dependence section.

Referring to Table II, the slope of I_V is in the range of values for exciton emission at 13 and 45 K. This immediately points to the possibility of the line attributed to exciton-related luminescence. It is worthwhile mentioning that the slope of I_V is nearly equal to the slope of ABE at 13 and 45 K which seems to support the idea that an ABE transition is the mechanism responsible for this line. Also worthy of mention is the considerable difference between the values of the slopes for FE and I_V which suggests that I_V is not FE-1LO.

At very low powers, the spectra show a peak at 2.7049 eV along with its phonon replicas. The energy separation between this line and the DAP1 emission line is 13.9 meV. As stated earlier, the binding energy for the donor involved in DAP1 luminescence is 18.5 meV which gives a difference between its ground state energy and the first excited state energy of 13.8 meV. Based solely on this, and the fact that the 2.7049 eV line is accompanied by phonon emission as is the case with the ground state DAP1 emission line, the 2.7049 eV peak is attributed to the first excited state of the donor giving rise to DAP1 and is labeled as $DAP1_{n=2}$. Similar observations have been reported by Zhang *et al.*[52] on MBE-grown materials. It has been suggested that $DAP_{n=2}$ is due to the R-series DAP emission involving a Li_i as the donor.[110] However, this cannot be the case because then an additional DBE line would be observed besides the I_2 peak typically seen in our Zn-extracted samples. The PL spectra always showed this line.

Uniaxial Stress Effects on Exciton Emission

The effects of strain on exciton luminescence can yield much insight into electronic band structure-related parameters such as deformation potential constants (i.e., the energy shift per unit strain in solids) and information about radiative recombination mechanisms. This should be particularly useful for identifying some of the controversial transitions occurring in the exciton-emission region of ZnSe. Before getting into the discussion of experimental results, the theory of stress-induced splitting of valence band states observed in optical spectra will be covered first. An attempt to "reinvent the wheel" regarding mathematical derivations will not be made here. However, the theory will be attacked from a qualitative perspective in moderate detail. A detailed derivation beginning with the total strain Hamiltonian can be found in the literature.[60-63]

Theory

It was shown in Fig. 2 of Chapter I that the valence band is four-fold degenerate for the J = 3/2 band and two-fold degenerate for the J = 1/2 band at k = 0 for unstrained material, and are separated by the spin-orbit splitting energy, $E_{s\text{-}o}$. Application of stress splits the J = 3/2 orbitals into two doubly degenerate bands with J = 3/2, $m_j = \pm 1/2$ as the light-hole band and J = 3/2, $m_j = \pm 3/2$ as the heavy-hole band. The band structure for unstrained and strained material at k = 0 is shown in Fig. 22 for a zincblende type crystal. For an unstrained crystal with wurtzite structure, the bands look like that shown for the strained case of the zincblende structure where the J = 3/2 and J = 1/2 valence bands are split by the crystal field, and the J = 3/2, $m_j = \pm 1/2$ and J = 3/2, $m_j = \pm 3/2$ states are split by the spin-orbit interaction.[43] It is generally observed that under compressive stress, the light-hole band moves "up" and the heavy-hole band moves "down" with respect to the "center of gravity" of the energy diagram.[64-67] Although observed rarely, for tensile stress the light-hole band moves "down" and the heavy-hole band seems to move "up" slowly. In isotropic crystals, uniaxial compressive stress is equivalent to biaxial stress which occurs in a plane perpendicular to the uniaxial direction and thus the material parameters in the uniaxial case mimic the effects of the parameters caused by biaxial strain resulting from the lattice mismatch in heteroepitaxial layers.

Characteristic of stressed samples is the polarization dependence of optical transitions. Shown in the inset of Fig. 22(b) are polarized transitions that take place when the valence band is split. The polarization or electric dipole selection rules $\Delta m = 0$ and $\Delta m = \pm 1$ predict that emission due to the J = 1/2, $m_j = \pm 1/2$ state in the valence band will have π- and σ-polarized components whereas the same state from the conduction band to the J = 3/2, $m_j = \pm 3/2$ state in the valence band will only be σ-polarized.[74]

At low stresses, the shift of the light-hole band toward low energy and the movement of the heavy-hole band toward high energy are linear in stress. However, at

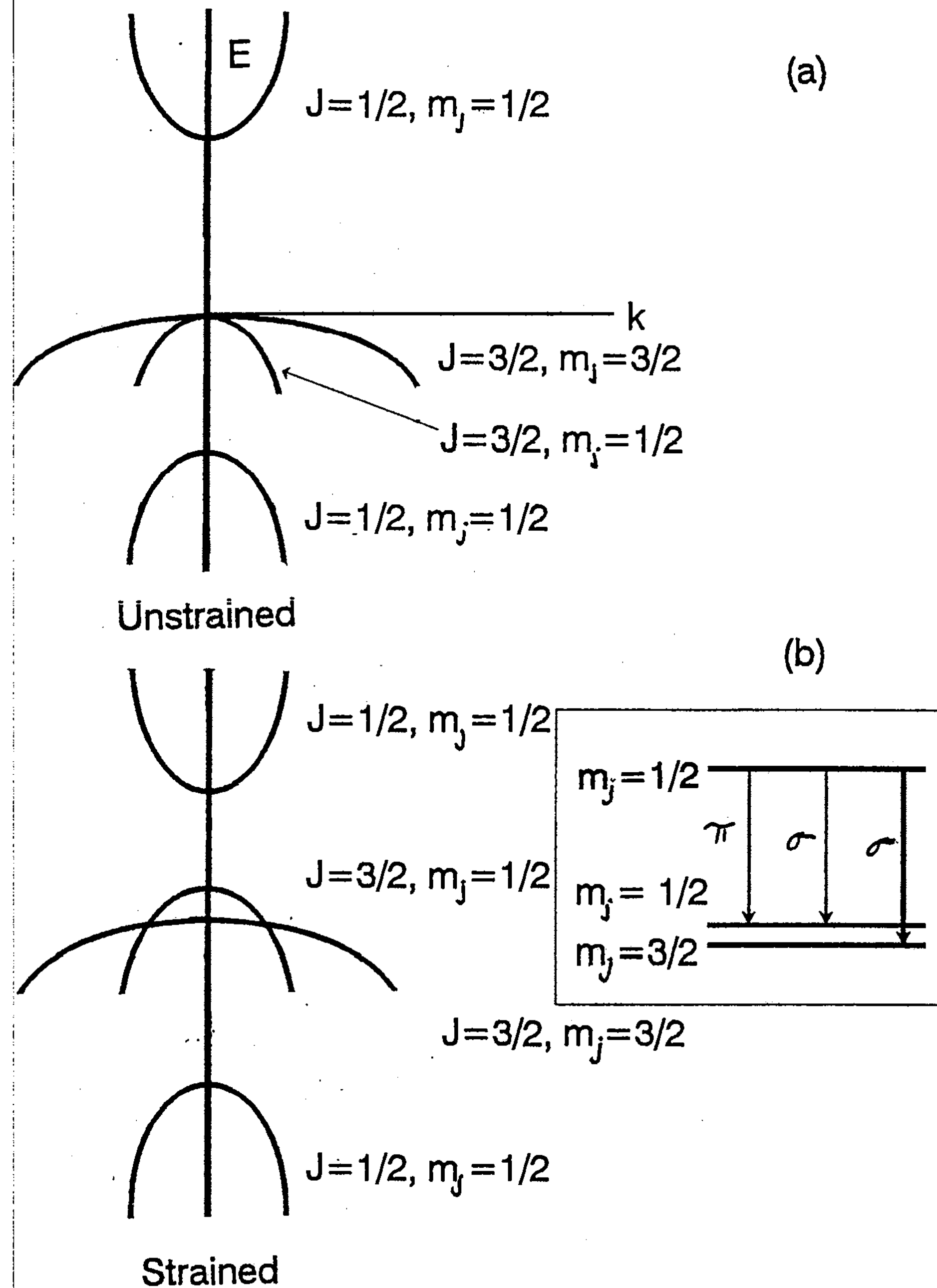

Figure 22. Schematic diagram of the band structure at the Γ point for (a) strained and (b) unstrained material. The inset shows the splitting of the valence band at J = 3/2, m_j = ±1/2 and corresponding π– and σ–polarized transitions. All m_j values have the ± symbol.

high stresses, the former band takes on a nonlinear stress dependence while the latter one generally stays linear. The linearity of the heavy- and light-hole components at low stress is a consequence of the stress-induced, linear splitting energy (E_s) being much smaller than E_{s-o} so that only the first order term in the perturbation calculation is retained. As a result of this, the stress-induced coupling between the J = 3/2 and J = 1/2 valence bands is very weak. When E_s is not << E_{s-o}, the second order term becomes significant and the coupling between the J = 3/2 and J = 1/2 states becomes dominant with the net effect that the light-hole band acquires a nonlinear stress dependence.[60,61,67]

The equations governing the type of stress behavior described above for heavy- and light-holes are given by[67]

$$\Delta E_{m_j=\pm 3/2} = a(S_{11} + 2S_{12})\chi + \frac{1}{2}E_s, \tag{57}$$

$$\Delta E_{m_j=\pm 1/2} = a(S_{11} + 2S_{12})\chi - \frac{1}{2}E_s\left(1 + \frac{E_s}{E_{s-o}}\right), \tag{58}$$

where the ΔEs are the fractional change in energy for each band and E_s is defined above. For the (100), (110) and (111) crystal planes it has the following forms,

$$E_s^{(100)} = 2b(S_{11} - S_{12})\chi, \tag{59}$$

$$E_s^{(110)} = \left[b^2(S_{11} - S_{12})^2 + \frac{1}{4}d^2 S_{44}^2\right]^{1/2} \chi, \tag{60}$$

$$E_s^{(111)} = d\frac{S_{44}}{\sqrt{3}}\chi. \tag{61}$$

In Eqs. (57)-(61), *a* is the hydrostatic deformation potential constant of the bandgap which represents the shift of the orbital bands (strain from the contribution of spin is neglected since its effect is small), *b* and *d* are the orbital shear (or uniaxial) deformation potential constants pertaining to strains in tetragonal and rhombohedral symmetries, respectively, S_{11}, S_{12} and S_{44} are the elastic compliance coefficients (Table I). In this

study, only Eqs. (57)-(59) are important and it will be assumed that the stress dependence on the exciton binding is small so that it can be ignored.

Discussion

Depicted in Fig. 23 are the stress-induced splitting of exciton states. The π- and σ-luminescence spectra for the zero stress case (Fig. 15 and 16) illustrate the same number of peaks and structure. The σ-emission spectrum exhibits an overall decrease in luminescence intensity by about a factor of 4 compared to the π-polarization case. Two conclusions can be drawn from these remarks: (1) the so-called "zero stress" spectrum show signs of residual strain perhaps due to the manner in which the crystals are grown, and (2) since both π- and σ-emission spectra at "zero stress" have equal numbers of lines, the luminescence transitions appear to terminate at the light-hole band because of the polarization dependence of these lines and their energies. An upward linear shift is observed for those emissions due to the heavy-hole band and a downward shift is seen for transitions due to the light-hole band at low stress, as shown in the figure. Based on the increase in energy for rising stress, FE^{hh} and I_2^{hh} are assigned to the heavy-hole component of FE and I_2, respectively. Likewise, FE^{lh} and I_2^{lh} are the light-hole components because of their decrease in energy. At high stresses, all lines decrease in energy and become nonlinear. The downward shift of the heavy-hole transitions could be due to the increased coupling with the light-hole emissions with stress because of the mixing between the J = 3/2, $m_j = \pm 1/2$ and J = 1/2, $m_j = \pm 1/2$ bands. The range of splitting between FE^{hh} and FE^{lh} is between 2.6 and 1.3 meV whereas I_2^{hh} and I_2^{lh} is between 1.2 and 0.6 meV. It should be emphasized that the splitting of the former is larger than that of the latter, and is consistent with reported values of 2.4 and 1.6 meV, respectively by Giapis *et al.*[68] and with other values determined elsewhere.[69-70]

A peculiar feature of the stress data in Fig. 15 is a high energy peak at 2.8032 eV for the zero stress spectrum with π-polarization. This has been labeled as FE^{LP} (lower

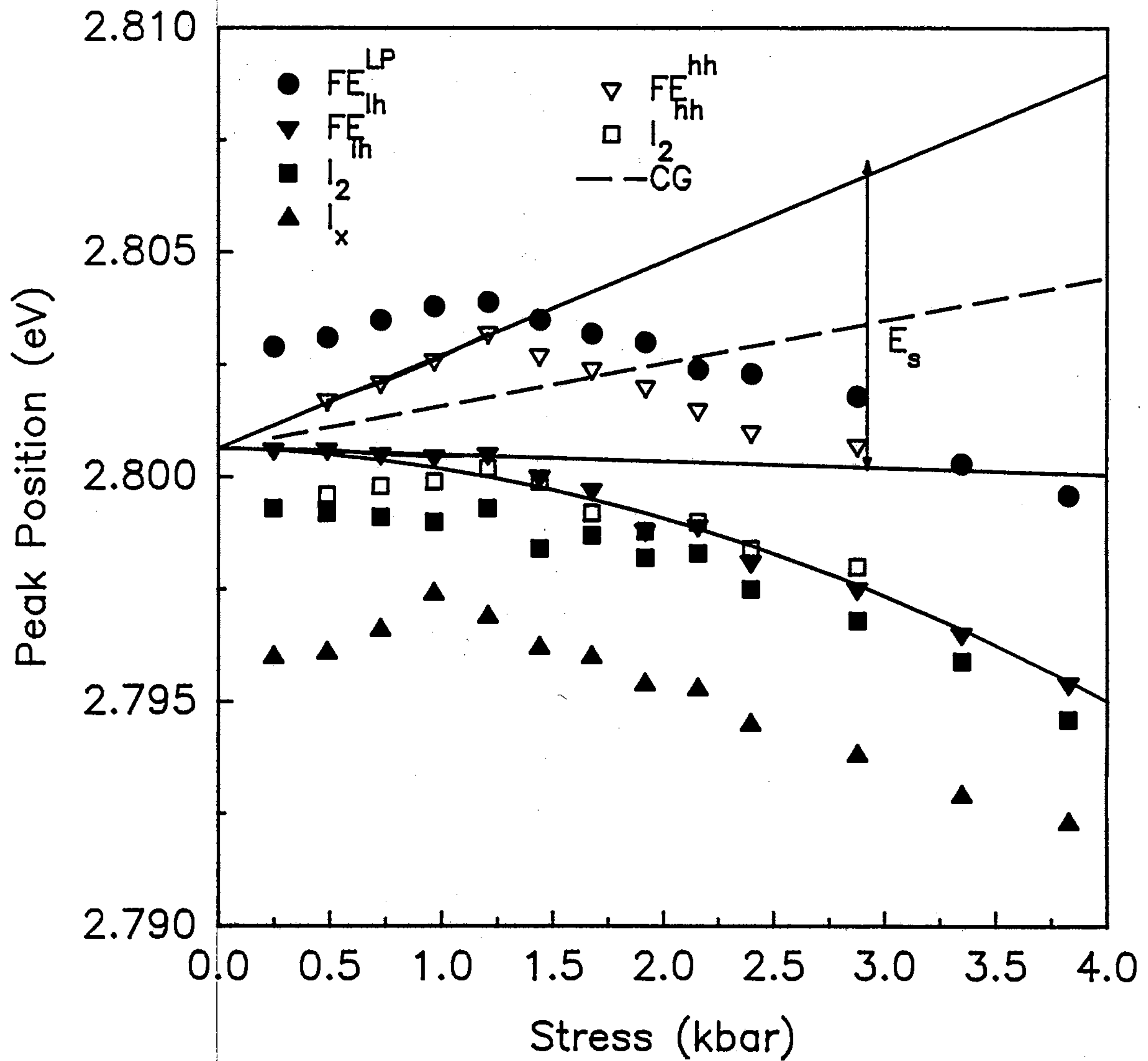

Figure 23. Splitting of the FE and I_2 transitions from a Zn-extracted, SPVT ZnSe sample. The graph has been corrected for the built-in strain for the sample unintentionally stressed. E_s shows the amount of splitting with stress, and the curved fit was accomplished using Eq. (58).

polariton branch of FE) in reference to a paper on polaritons in ZnSe; with FE^{LP} and the upper polariton branch, FE^{UP}, seen in π-polarization studies.[71,72] Also, evidence confirming the existence of polaritons demands that at least the lower branch be present.[81] Although the polariton is not the main topic of this thesis, a short discussion is presented for the sake of completeness. When photons with $h\nu > E_g$ are absorbed in a sample, they generate e-h pairs which are free to migrate in the crystal. Eventually, they diffuse to the band edges after loosing some energy by thermalization, defects and/or other scattering processes. If their net energy is lower than E_g—that is in resonance with excitons—then they form polaritons which are dipole-active excitons coupled to photons.[81] When the polariton is formed, the E vs k dispersion diagram of the exciton and photon give rise to upper and lower polariton branches for the polarization (i.e., the electric polarization of a medium) and electric field vectors of the exciton parallel (thus longitudinal exciton) and perpendicular (transverse exciton) to the wavevector, respectively. The two branches are separated by what is called the longitudinal-transverse splitting energy, ΔE_{LT}, which is about 1.45 meV in ZnSe. This means that when $k_B T \geq \Delta E_{LT}$, polaritons cease to exist and excitons remain in the crystal. Proceeding with the data analysis, it is possible that the lower polariton branch is overlapping with FE^{lh} however. Furthermore, it is likely that FE^{LP} could exist alone since mixing of other bands can occur with stress. It is interesting to note that Taguchi and Yao[57] assigned the 2.8051 and 2.8009 eV lines as lower polariton branch and exciton, respectively with no clear explanation.

The assignment of the DBE line at 2.7950 eV as I_x is often mixed in the literature with I_3 (an ionized DBE) or with I_2^{lh} (the light-hole component of I_2). These latter two assignments are refuted within the framework of this study for two reasons. Firstly, the stress-dependent spectra in Fig. 16 show the introduction of two additional lines for σ-polarization rather than three. Both FE^{lh} and I_2^{lh} become paired with their heavy-hole counterparts, FE^{hh} and I_2^{hh}, respectively but no additional peak is observed for I_x. This latter feature is consistent with deep levels since the impurity wavefunction is spread out

over a large region in k-space (or localized in r-space according to the Heisenberg uncertainty principle: $\Delta x \Delta p \approx \hbar$), allowing the electron to "see" more of the conduction band structure than just than just its minimum at the Γ point. Secondly, the variation of the I_x peak position with stress is different than the other peaks plotted in Fig. 23. All lines show initially a linear stress dependence while I_x varies nonlinearly. Also, in the regime at high stress, the shape of the I_x curve is in the form of an upward parabola whereas for the rest of the lines it points downward. Taken altogether, the origin of the I_x emission is that of recombination of an exciton bound to a deep neutral donor. As a consequence of this assignment, the line at 2.7949 eV in Fig. 14 has been labeled as I_x and the one at 2.7965 eV as I_2^{Ga} in view of the above analysis and from PL studies of Ga dip-treated samples which showed a line at 2.7967 eV. This peak corresponds to a neutral Ga DBE and has been previously observed in Ga-related materials.[75-77]

The linear hydrostatic deformation potential constant obtained in this work represents the shift of the conduction band relative to the average of the valence bands, and is calculated by fitting the first term in Eq. (57) to the shift of the center of gravity (CG) of the bandgap. This type of analysis using the CG has been employed before.[62] In a similar manner, the hydrostatic deformation potential constant for the conduction band relative to either the heavy- or light-hole band can be found reliably by fitting Eq. (57) or (58) to FE^{hh} or FE^{lh} since exciton states are pinned to the band edge and should follow the bandgap. To get the shear deformation potential constant of the bandgap, the linear splitting energy E_s defined in Eq. (59) is used. (That is, the emission energy of FE^{lh} is subtracted from the emission energy of FE^{hh} and the resulting line is then fit with the use Eq. (59).) Before fitting CG, it is necessary to find the point where FE^{hh} and FE^{lh} intersect which will be somewhere along the negative stress axis. Doing this gives an extrapolated value of -0.247 kbar, and as implied above, this means that the crystal is slightly stressed. Since this value is not small compared to the range of stress applied to the samples in this study, it will not be ignored. Thus this correction factor has been added to all data points

graph. In the absence of residual stress, all of the unstrained FE emission appears to come from the light-hole component since the calculated recombination energy is 2.8012 eV. With $E_{s\text{-}o}$ = 0.41 eV (Ref. 43), the best fit obtained is shown in Table III for compressive stress taken as negative. Here a_c and a_v are the linear hydrostatic deformation potentials for the conduction band and the average of the valence bands, respectively; $a = a_c - a_v$ and α and β are the linear and quadratic pressure coefficients representative of hydrostatic pressure measurements. Several remarks can be made regarding Table III. The values of *a* reported in the literature range from -3.0 to -5.8 eV. However, the calculated value of *a* from this work is smaller than these values. This could be due to the weak stress dependence of the conduction band as observed from the table (i.e., a_c is small in the SPVT samples). The value of b from FE^{lh} seems to be in agreement with only one value in the table but the value most frequently quoted in the literature is -1.2 eV, and may indicate that the deformation potentials are unique from sample to sample. Furthermore, fitting Eq. (58) to the FE^{lh} line (shown in the graph) gives a value for *a* and *b* of -13.7 and -2.5 eV, respectively. Converting the first term in Eq. (58) to the linear pressure coefficient, α, gives a value of -7.7 meV\kbar and is in the same order of magnitude as that for the band gap as calculated from Shan et al[78] by hydrostatic pressure measurements on similar SPVT materials. If the discrepancies of the values in the table are due to experimental error, then it is possible that the sample experienced a nonuniform distribution of stress. Otherwise, the deformation potentials can be taken as being characteristic of our SPVT materials.

TABLE III

DEFORMATION POTENTIAL AND PRESSURE COEFFICIENTS OF ZNSE

	a_v (eV)	a_c (eV)	a (eV)	b (eV)	α (meV/kbar)	β (meV/kbar)^2
E_g	----	----	-1.8	-0.37	1	----
FE^{hh}	----	----	0.12	-0.67	----	----
FE^{lh}	----	----	-13.7	-2.5	-7.7*	----
Van de Walle[82]	1.65	-4.17	-5.82	-1.2	----	----
Langer et al[43]	----	----	-3.0	-1.2	----	----
Tuchman et al[83]	----	----	-4.3**	-2.23**	6.7 (I_{20})†	-0.014
Shan et al[78]	----	----	----	----	7.3 (E_g)†	-0.015

*Pressure defined as negative

**Range of values exist for a and b based on different analyses

†Pressure defined as positive

CHAPTER III

HALL EFFECT

Introduction

PL provides a very sensitive means of detecting and identifying certain impurities in semiconductors. Of interest, however, is the concentration of impurities but these are difficult to obtain because it is not a simple matter to draw a correlation between the PL intensity and the concentration of a given impurity although some attempts have been made in the past to do this.[79] Nevertheless, the impurity concentration along with its ionization energy, mobility and free carrier density can be determined by electronic transport studies from using data from Hall effect measurements. This work reports some peculiar features of the activation energy, E, and electron mobility. For example, analysis of Hall data for a Zn-extracted sample reveals that E is much smaller that the effective-mass donor ionization energy and that the low-temperature mobility values are much higher than anticipated for the calculated impurity concentrations.

Experimental Details

Sample Preparation

The samples used for the Hall experiments were SPVT, Zn-extracted n-type ZnSe single crystals. Details of the SPVT method and other Zn-dip treatment process have already been described in Chapter II. Prior to attaching contacts the samples were etched in a bromine-methanol solution as outlined earlier in this thesis by Eagle-Picher (EP)

Laboratories. The ohmic contact material was formed by soldering In beads in a van der Pauw configuration and typically, the overall sample size was less than 1 cm x 1 cm x 1mm in volume. After performing PL measurements, some samples were sent back to EP for Hall effect testing, but problems with contact formation were encountered because a thin residual film of Si grease had remained on the crystal surface after cleaning with acetone. (Recall that Si grease is used in PL experiments to attach samples to the cold stage of the cryostat.) However, the film was painstakingly removed with bromine-methanol. For the C-V measurements, a Schottky diode configuration was formed using a Schottky contact and an ohmic contact on the same (111) face of a sample. Formation of the diode was performed with successive layers of Au and Pt while evaporated Au was used for the ohmic electrode. The latter contacts remained ohmic down to liquid nitrogen temperatures.

Cryogenic Hall Effect Procedure

The Hall measurements were performed by staff at Eagle-Picher Laboratories in Miami, OK and the raw data sent to OSU for analysis. Low-temperature electrical testing of ZnSe was carried out by using a closed loop cryogenic cold head and an automated electrical test station. The test station was set up to perform resistivity and Hall mobility measurements described by the van der Pauw technique and ASTM F76 (lamellar specimens.) Data acquisition and control was accomplished using an IEEE-488 control interface connected to a microcomputer. Connected to IEEE bus are relay switching and magnet controls, Hall voltage and magnetic field meters. The relay control outputs are used to control shielded reed relays which route the excitation current and voltage output connections from and to the sample. Some of these relays are switched so that a constant current can be applied to two of the four sample contacts with the voltmeter connected to the remaining contacts to measure the electric field or Hall voltage.

During the portion of the experiments which take data for calculating the Hall mobility, the current from the magnet power supply is controlled via the interface bus. The output of a calibrated Hall probe is amplified and directed to another voltmeter connected to the interface for feedback control of the magnet. Current is applied to the magnet through a set of wired, relay-controlled contractors to allow reversing of the magnet current.

The sample is attached to the cold stage of the cryogenic system by a teflon clip and isolated from the stage by a strip of teflon tape. Contact to the sample is made by four wires which exit the cold head through a teflon compression fitting. A radiation shield is placed over the cold finger and sample, and a vacuum shroud that is compatible with the magnet gap is secured to the cryo head. Once the head reaches a vacuum of approximately 10 millitorr, the vacuum shroud is centered in the magnet gap and the cryogenic system started. At this time, the desired temperature is input to the cryo head controller.

When the automated testing begins, a bias current is applied to two adjacent contacts of the specimen and the resultant voltage is measured at the remaining two. This voltage is compared at 30 second intervals, and when the change is below a predetermined limit, the actual testing begins. In this way, the sample itself determines when it is at the temperature setpoint. Subsequent test temperatures are entered manually at the cryo head controller and sample testing proceeds as above.

Analysis of Data

Electrical Data

Information about free carrier concentrations in n-type material is generally obtained from the Hall coefficient (R_H) by the expression $n = -1/(eR_H)$ where e is the electronic charge. Usually, information about impurities is desired as well since their

presence in the lattice can either enhance or cause adverse effects on the electrical conductivity. An approximate relation can be developed to calculate their densities in compensated materials with the use of Fermi statistics. The most common approach is to assume that the density of donors is described by a single donor level in the presence of compensating acceptor states with the additional condition that all acceptor levels are fully ionized. Justification of this condition applies to n-type material. Since the donors are less than 100% compensated regardless of how small the density of compensating impurities even at T = 0 K, the Fermi level starts at the donor ionization energy and decreases with an increase in temperature for highly compensated samples. The assumption is even valid in the presence of several donor states as long as the concentration of this single donor level is much higher than the other donor impurities. It was shown in Chapter II that the transition giving rise to the h-D^o PL line involved a relatively deep donor level. However, to adhere to the assumption of a single donor, the concentration of the deep donor will be assumed small compared to the assumed single donor level. This is justified by the fact that the low temperature PL does not show a transition involving the deep donor state, and the room temperature emission is many orders of magnitude smaller than the emissions observed at low temperature. The expression obtained for this case is the widely known compensation equation,

$$\frac{n_o(N_A + n_o)}{N_D - N_A - n_o} = \frac{N_c}{g} e^{-E/k_B T} \tag{62}$$

where n_o is the equilibrium free carrier concentration, N_D is the density of donor states, N_A the density of acceptors, E is the ionization energy of the donor, g is the ground-state degeneracy factor of the donor level and N_c is the effective density of states in the conduction band,

$$N_c = 2\left(\frac{2\pi m_e^* k_B T}{h^2}\right)^{3/2} . \tag{63}$$

Equation (62) is valid at any temperature provided n_o is not large enough to invoke complications of degeneracy that is, exp $(E_F - E_c) = n_o/N_c$. To avoid this, it is required that E_F be several kT below E_c so that Eq. (62) can be applicable. In order to use this equation to fit the data, n_o is solved from a quadratic expression with only the positive root having physical significance. Then N_D and N_A are used as fitting parameters and their values are thus determined. Usually of concern are errors in the values of N_D and N_A due to contributions to the free carrier concentration from intrinsic carriers and from deep lying levels at high temperatures. However, these are not a factor here because n_i(296 K) ~ 10^{10} cm^{-3} and the density of deep level impurities have been substantially reduced by the Zn-dip process.

In the case when the density of donor atoms is very high—and thus closely spaced—the carrier wave functions between neighboring atoms begin to overlap. Although the effect of overlap is small, this causes the formation of impurity bands to occur and consequently an impurity band conduction process becomes possible. Here, for example, the electron from a donor tunnels (or hops) through an adjacent donor without activation into the conduction band. Such impurity conductivity will have a measurable effect at low temperatures and will be characterized by a small activation energy (denoted ε_2 or ε_3) from the E term in Eq. (62).[80,84]

Hall mobility measurements can provide valuable insight into the electronic transport characteristics of crystals when different types of scattering mechanisms are analyzed. In the II-VI compounds, it appears that a number of reports included different combinations of several mechanisms to describe the mobility. From previous studies of the mobility in ZnSe, scattering by ionized impurities, polar optical-phonons, acoustic

deformation potential and piezoelectric phonons have been found to be dominant.[85-87] Before examining the temperature dependence of the mobility, it is convenient to estimate at this point, what the possible scattering mechanisms would be by checking whether their mobility values are in the right order of magnitudes as that from the experimental data. For example, it has been suggested that the acoustic and piezoelectric terms do not have an appreciable effect on the scattering because their theoretical values are 40 (acoustic term) and 100 (piezoelectric term) times smaller than the measured values.[88] Applying the same argument to this study gives a mobility that is 37 and 401 times larger than that measured, respectively. Notwithstanding this, the acoustic term will still be taken into account in the present analysis. PL measurements have revealed the presence of DAP transitions as noted in Chapter II. It is worth emphasizing that crystals which exhibit high mobility have been known to contain defect pairs or DAP. Defect pairs have a tendency to scatter carriers inefficiently since the Coulomb field of an isolated charged center is reduced when paired with an oppositely charged center.

The mobility data from the samples in this study are examined with the above scattering mechanisms taken into consideration and the use of Mathiessen's rule. This is based on the assumption that for different types of scattering centers, the reciprocal of the total time of a carrier between collisions is equal to the sum of the reciprocal of the independent scattering time from each center.[89] The rule applies to the mobility since it is directly related to the scattering time, thus:

$$\frac{1}{\mu} = \frac{1}{\mu_{i\ or\ pair}} + \frac{1}{\mu_N} + \frac{1}{\mu_{pol}} + \frac{1}{\mu_{adp}} \tag{64}$$

where $\mu_{i\ or\ pair}$ is the mobility due to either ionized impurity scattering or pair scattering as will be discussed later in the analysis; and μ_N, μ_{adp} and μ_{pol} are the mobilities for neutral impurity, acoustic phonon deformation potential and polar optical phonon scattering, respectively. The mobility equation for ionized impurity scattering is known as the

Brooks-Herring formula.[90] The expression describing this type of scattering is based on electrons interacting with the Coulomb field of ionized impurity atoms which are arranged randomly in the lattice and thus scatter independently. In MKS units,

$$\mu_i = \frac{2^{7/2}(4\pi\varepsilon\varepsilon_o)^2(k_B T)^{3/2}}{\pi^{3/2}Z^2 e^3 m_e^{*1/2} N_I\left[ln(1+\beta) - \beta/(1+\beta)\right]} \tag{65}$$

where ε and ε_o are the dielectric constant and permitivity of free space, respectively; Z is the effective charge and N_I (= $N_D^+ + N_A^-$) is the total ionized impurity concentration and

$$\beta = 6m_e^*(kT)^2\,\varepsilon / \pi\hbar e^2 n. \tag{66}$$

Here n (= N_D^+ - N_A^-) is the total number of carriers and all other terms have their usual meaning. Substituting all relevant parameters for ZnSe into Eqs. (65) and (66), and converting to CGS units give

$$\mu_i = \frac{3.2816x10^5(T/300\ K)^{3/2}}{\left(N_I/10^{16}\ cm^{-3}\right)\left[ln(1+\beta) - \beta/(1+\beta)\right]} \quad cm^2/Vs \tag{67}$$

and

$$\beta = 1.903x10^{14}T^2/n \tag{68}$$

Conwell and Weisskopf[91] have also derived a similar relation for ionized impurity scattering where they arbitrarily "cut off" the scattering cross section to half the mean distance between neighboring impurities. This is unlike considering the screened Coulomb potential of each ion as calculated quantum mechanically by Brooks and Herring, which gives a more accurate result.

Considering the mobility due to pair scattering instead of μ_i in Eq. (64),[92]

$$\mu_{pair} = \frac{\sqrt{2}\hbar^2 \varepsilon^2 (k_B T)^{1/2}}{\pi^{3/2} Z^2 e^3 m_e^{*3/2} N_p R^2} f(\gamma^2) \tag{69}$$

where R is the dipole distance (or donor-to-acceptor separation), N_p is the concentration of pairs and

$$f(\gamma^2) = \left[2\left(\frac{1 + 1/\gamma^2}{1 + 2/\gamma^2} \right) - \gamma^2 \ln\left(1 + 2/\gamma^2\right) \right]^{-1} \tag{70}$$

with the dimensionless parameter

$$\gamma^2 = \left(\frac{\pi \hbar^2 e^2}{2 m_e^* \varepsilon k_B^2} \right) \left(\frac{n}{T^2} \right). \tag{71}$$

n (= N_D^+ - N_A^-) is the free carrier concentration. In numerical form, and in CGS units, Eq. (69) becomes

$$\mu_{pair} = \frac{2.1283 x 10^6 (T/300\ K)^{1/2}}{Z^2 (N_p / 10^{16}\ cm^{-3})(R/10^{-6}\ cm)^2} f(\gamma^2) \quad cm^2/Vs \tag{72}$$

and

$$\gamma^2 = 1.5357 x 10^{-14} n / T^2. \tag{73}$$

The derivation of Eq. (69) is based on the theory of ionized impurity scattering by Brooks and Herring except that the screened coulomb potential is that of a dipole. The second term in Eq. (64) occurs predominantly at very low temperatures since the

concentration of ionized impurities is reduced by carrier freeze-out and scattering due to phonons is reduced by phonon freeze-out. Scattering caused by neutral impurities is analogous to the problem of scattering of low-energy electrons by a gas and can be expanded to the case of that in crystals.[93] In MKS units,

$$\mu_N = \frac{e}{20 a_B^* \hbar N_N} \tag{74}$$

where a_B^* (= $\varepsilon a_B/(m_e^*/m_o)$) is the effective Bohr radius of the impurity and N_N is the concentration of neutral impurities. After substituting the appropriate parameters in Eq. (74) and in CGS units,

$$\mu_N = \frac{2.8174 x 10^4}{N_N / 10^{16} cm^{-3}} \quad cm^2 / Vs \tag{75}$$

Polar optical phonon scattering, the third term in Eq. (64), is due to scattering of free carriers by the induced electric polarization setup from vibrations of optical modes with a large dipole moment. The polar coupling constant which describes the strength of interaction between the electron and phonon (i.e., it represents twice the number of virtual phonons interacting with a carrier moving slowly in its band) is given by

$$\alpha = e^2 \left(\frac{1}{\varepsilon_\infty} - \frac{1}{\varepsilon} \right) \left(\frac{m_e^*}{2 \omega_{LO} \hbar^3} \right)^{1/2} . \tag{76}$$

where ε_∞ is the high-frequency dielectric constant and ω_{LO} is the LO phonon frequency. The conductivity due to optical modes in polar semiconductors has been calculated with use of the variational method.[94] Using a similar approach, Ziman[95] has derived an expression for the mobility. Written here in a slightly different form to conform to the notation of Ref. 91, this expression becomes,

$$\mu_{pol} = \frac{0.871}{\alpha\hbar\omega_{LO}\left(m_e^*/m\right)} \frac{e^z - 1}{z^{1/2}} G(z) e^{-\xi} \quad cm^2/Vs \tag{77}$$

where α (=0.54) is the coupling constant introduced above, $\hbar\omega_{LO}$ is the energy of the LO phonon in eV, z = $\hbar\omega_{LO}/k_BT$, and $G(z)e^{-\xi}$ is a slowly varying function which is tabulated in Ref. 94. The degree of accuracy of Eq. (75) can be obtained for any desired order of $G(z)e^{-\xi}$. In the non-degenerate limit low temperature regime (i.e., z large), and neglecting $G(z)e^{-\xi}$, the mobility takes the form

$$\mu_{pol} = \frac{0.868}{\alpha\hbar\omega_{LO}\left(m_e^*/m\right)} \frac{e^z - 1}{z^{1/2}} \quad cm^2/Vs \tag{78}$$

The fourth term in Eq. (64) is due to scattering by acoustic phonons which is based on deformation potential theory.[90] The effect of this scattering term on the mobility is not as large as that for polar optical phonons since the electron-phonon interaction is due to the smaller dipole moment resulting from the acoustic lattice vibrations. The mobility expression in this case is

$$\mu_{adp} = \frac{2(2\pi)^{1/2} e\hbar^4 D u_l^2}{3 m_e^{5/2} (k_B T)^{3/2} E_1^2} \tag{79}$$

Here D is the material density, u_l is the longitudinal sound velocity and E_1 (or a_c from Chapter II) is the deformation potential of the conduction band. The value of Du_l^2 has been calculated to be 8.59×10^{11} and 8.88×10^{11} dyn/cm^2 at 300 and 12 K, respectively.[59] Since the temperature dependence is small, the average value of 8.735×10^{11} dyn/cm^2 will be used. Regarding E_1, several values of the deformation potential were presented in Chapter II along with some calculated values from this work. However, only values for the band gap (i.e., *a*) were obtained. This value could be obtained as a curve fitting

parameter but the value of -4.17 eV will be employed.[82] Substituting the appropriate constants, this relation becomes

$$\mu_{adp} = 2.434x10^4 (300\ K/T)^{3/2} \quad cm^2/Vs \tag{80}$$

Results and Discussion

Figure 24 shows the temperature dependence of the free carrier density for three low resistivity, Zn-extracted n-type samples ranging from 4.16 to 30.1 Ω cm. The carrier concentration for each sample shows two temperature regimes, one at low temperatures denoted as the "freeze-out" region and the other at higher temperatures termed the "exhaustion" region. The former region occurs when the thermal energy of the lattice is not sufficient to ionize any donors (or acceptors). As the temperature rises, the donors ionize and the carrier concentration becomes independent of temperature as shown in the later region. Barely noticeable in the figure is a slight increase of carrier concentration near room temperature, which is typically characteristic of intrinsic effects. While donor ionization is taking place, some bonds begin to break as a result of the increased kinetic energy of electrons in the valence band with temperature, and are subsequently excited into the conduction band (thus intrinsic). At elevated temperatures, many bonds are broken and the intrinsic carrier concentration becomes larger than the density of donated electrons making n increase. After letting g=2 for donor states, all three sets of data were fit by Eq. (62) and the parameters extracted from the analysis are shown in Table IV.

Several features are worthy of mention. (1) As the resistivity increases from sample to sample, N_D and N_A (or N_A^-) increase, but $N_D - N_A$ decreases. (2) The compensation ratio, K (= N_A/N_D) which defines how many donor electrons become electrically inactive (do not take part in the conductivity) as a result of the presence of

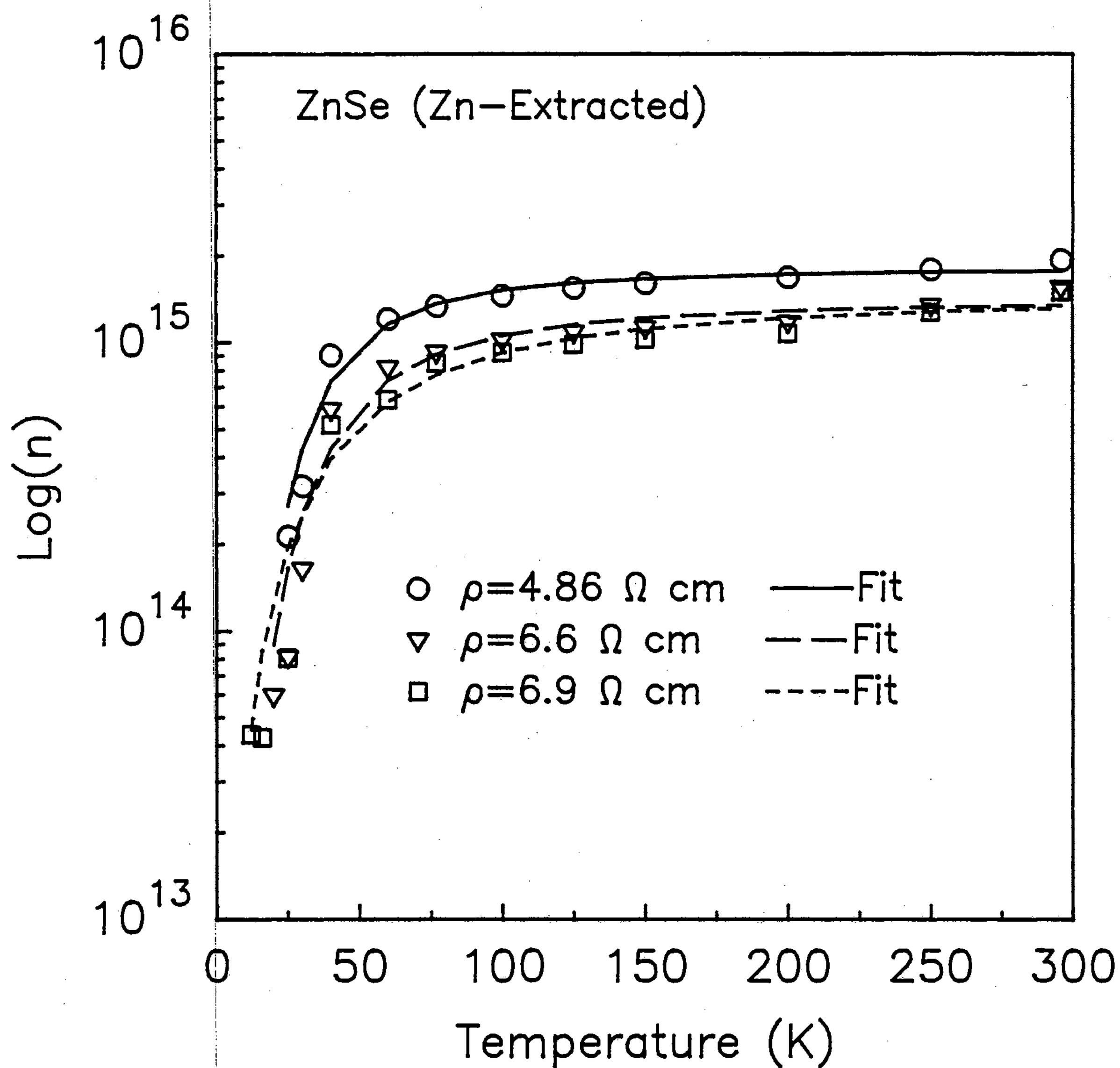

Figure 24. Free carrier concentration as a function of temperature for three Zn-dipped SPVT samples with $\rho = 4.86$, 6.6 and 6.9 Ω cm. The corresponding fits are shown as well.

TABLE IV

PARAMETERS OBTAINED FROM HALL MEASUREMENTS FOR THREE SAMPLES

ρ	N_D	N_A	N_D-N_A	$K=N_A/N_D$	E	n_o (295 K)
(Ω cm)	(10^{16} cm^{-3})	(10^{16} cm^{-3})	(10^{15} cm^{-3})	(%)	(meV)	(10^{15} cm^{-3})
4.86	2.25	2.06	1.9	92.0	3.81	1.94
6.60	4.17	4.02	1.5	96.4	2.97	1.56
6.90	8.85	8.71	1.4	98.4	0.96	1.51

holes, goes up from 92% to 98% and the large values clearly show that the samples are all highly compensated. (3) The free carrier concentration at room temperature is seen to agree well with the calculated $N_D - N_A$ values and suggests that the single donor level assumed in Eq. (62) is justifiable. (4) A peculiar point to be made from the table is the lowering of E as the impurity concentration increases. The donor binding energies calculated from Eq. (62) do not conform to the effective-mass donor ionization energy of approximately 29 meV. Results of this type from other compensated materials have been observed in MBE,[96] MOCVD[97] and other bulk crystals.[98] (The behavior of E will be explained in the Further Discussion Section).

Capacitance-voltage (C-V) measurements can provide information on the free carrier concentration in the region of the junction. In Fig. 25 is shown a $1/C^2$ vs. V plot of a Schottky diode formed from a Zn-extracted, SPVT ZnSe sample of resistivity slightly higher than those shown in Table IV. For a material with a uniform distribution of doped impurities, the $1/C^2$ against V gives the doping density N (= $N_D - N_A$) which is the concentration of shallow-level impurities compensated by any deep level states present. The expression to calculate the doping density or for that matter the carrier concentration in the region of the junction is[99]

$$\frac{1}{C^2} = \frac{2(V_D - V)}{e\varepsilon N} \tag{81}$$

where C is the capacitance in the depletion region, ε is the dielectric constant, e is the electronic charge, V is the applied voltage and V_D is the built-in potential (or contact potential) at the junction. The Schottky diode along with other diodes from similarly treated specimens gave N_D-N_A values of approximately 1.5×10^{15} cm^{-3} in very good agreement with Hall measurements.

Depicted in Fig. 26 is the temperature dependence of the electron mobility for the three specimens presented in Fig. 24. The mobility of the samples is very high for bulk

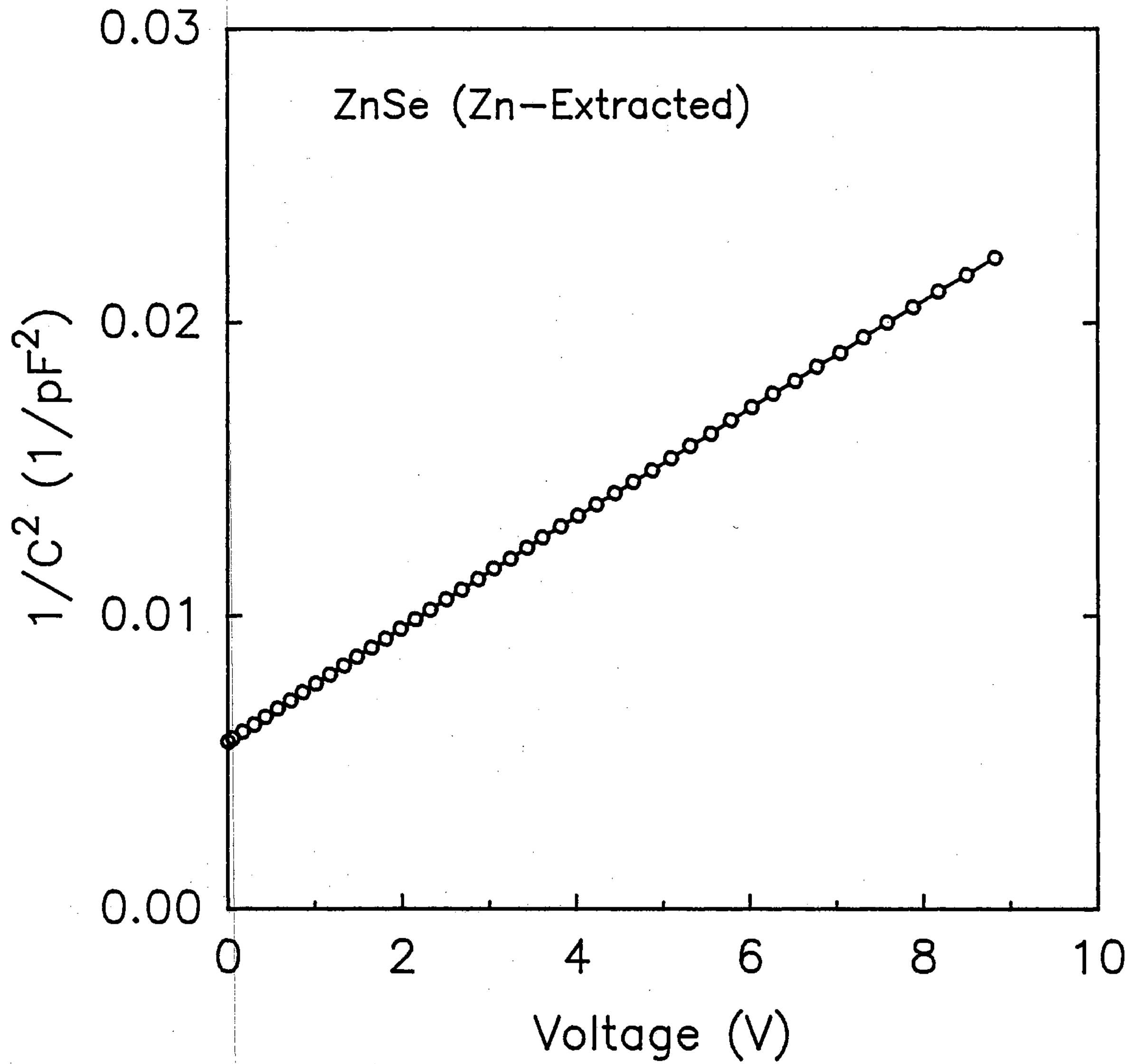

Figure 25. $1/C^2$ versus V plot from a Schottky diode formed on a Zn-extracted, SPVT ZnSe crystal. The slope of the line yielded free carrier concentrations in the order of 10^{15} cm^{-3}.

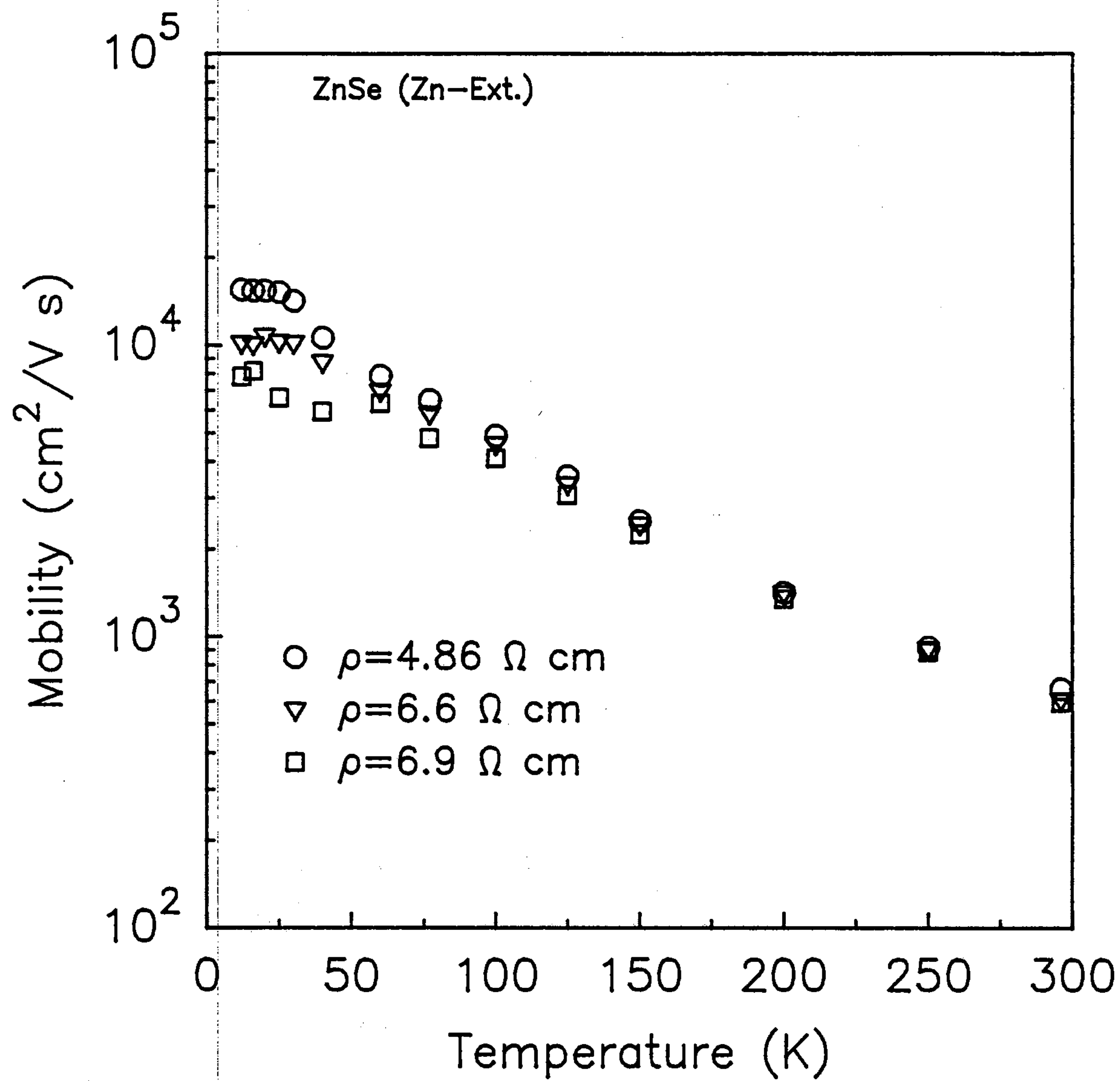

Figure 26. The change of carrier mobility with temperature for the three samples shown in Fig. 24. The mobilities are high for bulk material.

ZnSe and the mobility maximum appears at very low temperatures. The maximum value for the mobility is approximately 1.5×10^4 cm^2/Vs at about 20 K for the lowest resistivity material and from that point it decreases with temperature. Slightly lower mobility values were reported by Aven[100], but with the maximum occurring at 50 K, for samples which had been repeatedly Zn-dipped. Aven attributed the high mobility to the removal of deep acceptor states during the Zn-extraction process. Another feature noted in our samples is that the room temperature mobility range from 596-662 cm^2/Vs, and just for comparison purposes only, these are higher than measured values of 430-550 cm^2/Vs from MBE-grown samples.[101] The temperature dependence of the electron mobility encountered in the literature typically increases until it peaks (typically between 40 and 60 K) followed by a decrease, all along with rising temperature. This is in contrast to the results presented in Fig. 26 where the mobility begins at a high value and then decreases with an increase in temperature. A similar trend in the mobility data has been observed in CdS single crystals supplied by Eagle-Picher laboratories which were grown by a vapor technique.[102] A final point to be made is that the mobility maximum at very low temperatures is reduced as the sample resistivity goes up because of the increase in scattering centers due to a corresponding increase in impurity concentration.

Figure 27 shows plots of the mobility versus temperature for different scattering mechanisms with some plots calculated using Eqs. (65)-(80). The expressions governing the other scattering processes have been used with parameters appropriate to bulk ZnSe as reported in the literature. As can be seen, in order for acoustic deformation potential and piezoelectric scattering to have a substantial contribution to the mobility, the measured mobility data must be in a range between 10^6 and 10^8 cm^2/Vs at high temperatures as shown in the figure. But as argued earlier, only the acoustic term will be included in the analysis of the mobility since its room temperature value is nearer to that of the measured data than the piezoelectric term. The decrease in mobility as the temperature is raised is due to the increase in acoustic lattice vibrations. Pair (or dipole) scattering displays a

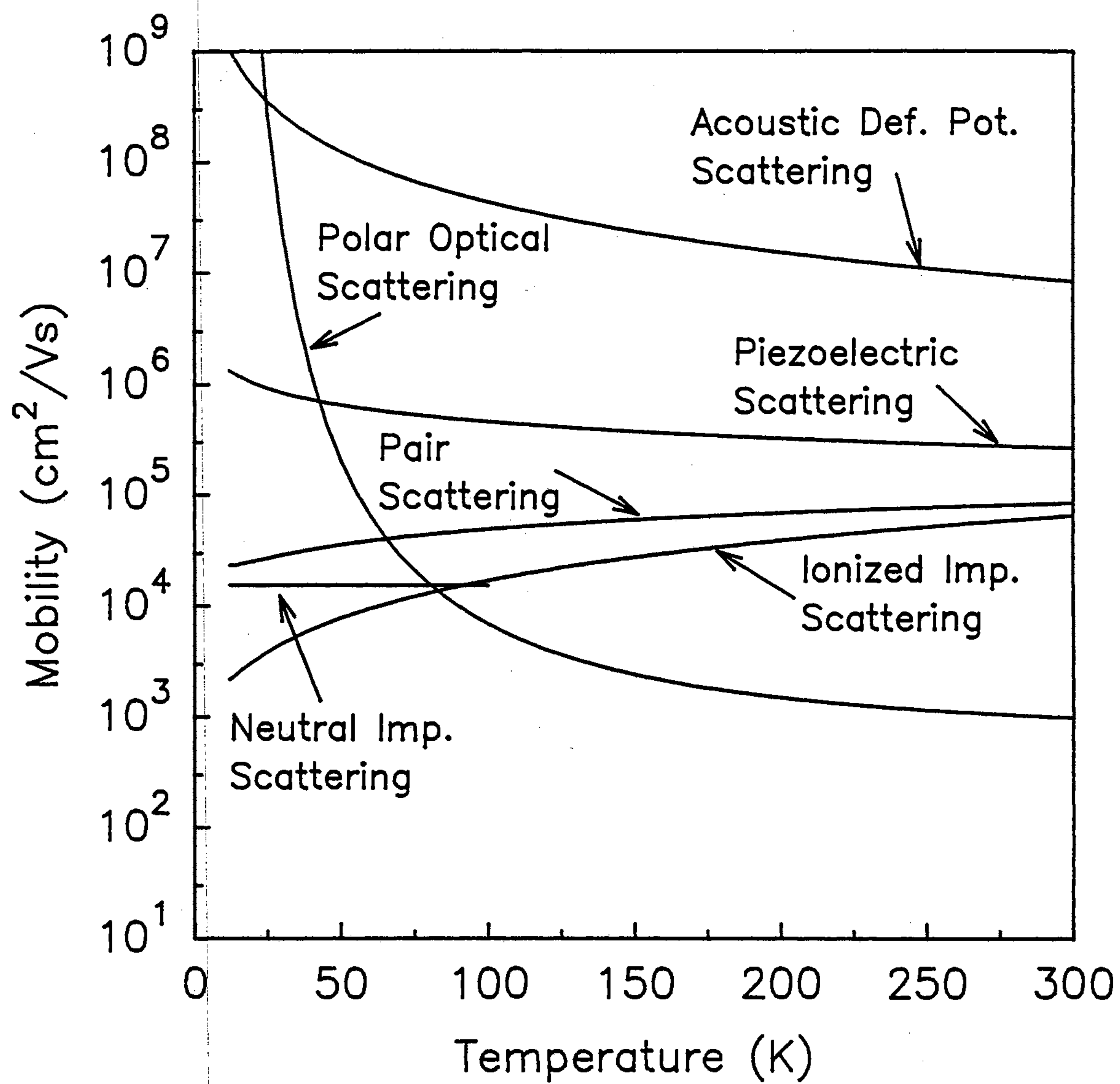

Figure 27. Theoretical plots of the mobility showing the range of values for each scattering mechanism.

dominant portion of the low-temperature mobility over the ionized impurity term because of the reduction in the Coulomb field for the latter process when paired with an oppositely charged center, as explained earlier. The mobility due to both pair and ionized impurity scattering increases with an increase in temperature due to the gain in kinetic energy of the faster electrons. Scattering due to neutral impurities is temperature-independent at very low temperatures as represented by the straight line. The line has been extended to 100 K for clarity but the impurities in the samples currently under study are neutral up to 25 K, as shown in Fig. 26 by the straight line portion of the data points.

Attempts to fit the mobility using Eq. (64) with the pair and ionized impurity terms used separately, each in conjunction with all the other scattering terms resulted in poor fits. Besides the poor fits is the difficulty of fitting the data with a small set of parameters. Also, some of the scattering terms have been derived with approximations which makes it difficult to obtain a decent fit. To circumvent this, some authors combine the polar optical phonon and acoustic deformation potential terms in Eq. (64) into a single empirical expression given by[102]

$$\mu_{pol/adp} = AT^{-m} \tag{82}$$

where A and m are fitting parameters. Now the last two terms in Eq. (64) have been reduced to one term so that three total terms (the other two described in the data analysis section) are used to represent Eq. (64). A fit to the temperature dependence of the electron mobility for the lowest resistivity sample is shown in Fig. 28. Although the fit is good for a particular set of parameters, it was found that other parameters gave good fits as well. For example, the concentration of pairs ranged beween 10^{15} and 10^{16} cm^{-3}. The concentration of neutral impurities was typically in the order of 10^{16} cm^{-3}. The concentration of ionized impurities ranged from 10^{13} to 10^{16} cm^{-3} with the former concentration obtained only for ionized impurity scattering in Eq. (64) along with the other terms (except pairs). The latter value was obtained only for pair scattering (no

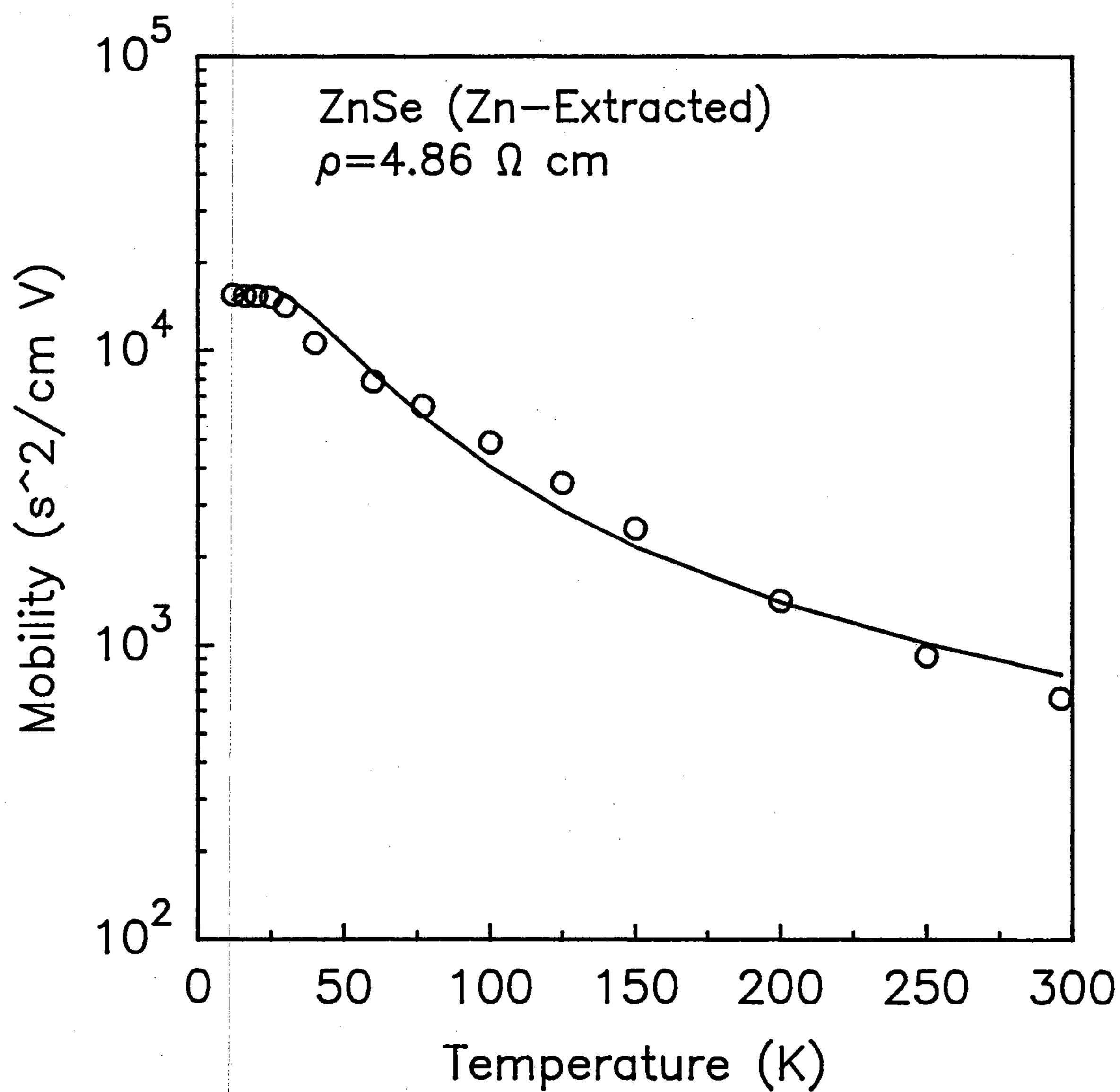

Figure 28. Fit of the mobility using pair, neutral, polar optical phonon and acoustic deformation potential scattering for the lowest resistivity sample shown in Fig. 26.

term) It should be noted that incorporated in the pair term is $n = N_D^+ - N_A^-$. It is interesting to note that by including ionized impurity scattering only in Eq. (64), the concentration of ionized impurities which are acting as scattering centers seems to be low. By including pair scattering we find that the value of N_P for the 4.86 Ω cm sample is approximately in the same order of magnitude required to correct the discrepancy observed for the slope of the DAP emission intensity dependence on laser power discussed in the previous chapter. Thus, if one only takes the results from ionized impurity scattering, it may be concluded that ionized impurities do not from effective scattering sites because of the tendency to form pairs.

Further Discussion

Results from photoconductivity and thermally stimulated conductivity in SPVT ZnSe samples (refer to Markey (1993)[103]) show that the concentration of deep, mid-gap states is high. These are neutral at the temperatures of this study and are probably the source of the neutral scattering sites observed in the experiments.

The activation energies extracted from the free carrier concentration fit reveal that they are very small compared to the hydrogenic effective mass value (Table I) for donor states. There are a number of possibilities which could explain this. Firstly, it has been suggested that the impurity level moves toward the conduction band (or more accurately, its binding energy decreases) due to one or a combination of the following effects: (i) the variation of the dielectric constant as a result of polarizable neutral donors, (ii) screening between the bound electron on the donor and the donor ionic core due to electrons in the conduction band and (iii) the attraction between electrons in the conduction band and the positively charged donor ions.[104] Secondly, conduction band edge tailing effects is believed to cause a reduction in the donor binding energy,[104] and thirdly, impurity band conduction has been known to give small values of the activation energy.[105-107] Whether each of these factors contributes to the reduction in the activation energy from the SPVT

ZnSe samples will be briefly discussed below. It should be pointed out that the mathematical expressions that follow will be used only to help determine qualitatively the various mechanisms responsible for the decrease in E_d. Detailed derivations of such equations can be found in Ref. 101 and the references therein.

For an arrangement of neutral donors, its polarization can be produced in such a way that the applied field (i.e., the E-field to drive the electrons in the Hall effect) distorts the charge distributions and consequently generates an induced dipole moment in each donor.[108] In silicon, $\varepsilon = 11.9$ and for donor concentrations in the order of 10^{18} cm^{-3}, the shift of the donor state with respect to the edge of the conduction band is less than 1 meV which is small compared to the average energy of 40 meV for most shallow donors. In ZnSe, the smaller value of $\varepsilon = 8.9$ and the difficulty in obtaining high impurity concentrations are expected to give an even smaller contribution to the shift. Thus, the dependence of ε on the impurity concentration is weak and can be ignored.

Screening between the bound electron in the ground state of the donor level and the donor ion is due to the presence of electrons in the conduction band. The effect this has on the donor impurity level is to lower the binding energy by shifting the ground state energy closer to the band edge. An expression has been obtained to estimate the degree of shift. In MKS units, this is given by[104]

$$\Delta E_B = \frac{e^2}{4\pi\varepsilon\varepsilon_o}\left(\frac{3}{8} - 2\xi\lambda_e\left[\frac{sin(1/2\xi\lambda_e) + 2\,tan^{-1}(1/8\xi\lambda_e)}{4 + 1/16\xi^2\lambda_e^2}\right]\right) \qquad (83)$$

where ξ (= 1/30 Å) is the reciprocal of the effective Bohr radius in ZnSe, and λ_e is the electron screening length which is (MKS)

$$\lambda_e = \left(\frac{\varepsilon\varepsilon_o k_B T}{e^2 n}\right)^{1/2} \qquad (84)$$

An upper limit for ΔE_B is obtained by selecting the lowest temperature in the exhaustion region with corresponding n = 1.5 X $10^{15}cm^{-3}$. These values define the smallest λ_e for the calculated upper limit of $\Delta E_B \leq 7$ meV. Subtracting ΔE_B from the donor binding of 29.2 meV does not account for the calculated low energies in Table IV. Hence, the effect of screening can be neglected.

The attractive interaction between the electrons in the conduction band and the ionized donors in the presence of compensating acceptors causes the position of the band edge to change. It is believed that the random spatial distribution of the ionized impurities gives rise to the average shift of the band edge. An expression has been derived to account for the variation of the position of the band edge with donor concentration, denoted as ΔE_c.[104] For ZnSe, this gives ΔE_c=3.9 meV. The parameters used in calculating ΔE_c correspond to the circumstances of interest here (i.e., T=100 K and n=1.5x10^{15} cm^{-3}). Since the band edge shift is small, it does not influence the binding energy by much, so it is ignored as well.

The second possibility deals with band edge tailing effects. As stated above, the random spatial distribution of ionized donors and acceptors gives rise to a shift of the band edge. The result of this also produces spatial fluctuations in the potential because of the non periodicity of the lattice. The net effect due to the potential fluctuation is to create a tail on the density of states in the conduction band by spreading out the conduction band edge. The amount of spreading in ZnSe is estimated as 4.85 meV. Again, this is not large enough to significantly influence the binding energy. Even if all of the above effects contributed together, the expected change in the binding energy would still be too small to account for a significant shift.

Thirdly, the conduction mechanism of a particular semiconductor moderately doped (i.e., greater than 10^{16} cm^{-3}) often exhibits two conduction regimes both of which are competing processes. One regime occurs at high temperatures and is due to conduction of electrons in the conduction band that have been thermally activated from

donors with a binding energy, E_d (= $E_c - E_D$, where the first and second terms are the energy separations of the conduction band and donor level relative to the valence band, respectively) The other regime takes place at very low temperatures and is a property of impurity band conduction which occurs with a characteristic low activation energy. This process is due to the small but finite overlap of the wave function between adjacent donor neighbors where the electron hops (i.e., thermally assisted tunneling) from an occupied to an unoccupied donor state without activation into the conduction band. Conductivity in an impurity band mainly occurs in a compensated semiconductor unless the donor wave functions strongly overlap thus allowing the electrons to flow in the absence of compensation. This is because when a portion of donors loose electrons to the compensating acceptors, the unoccupied donor levels left behind facilitate the motion of the remaining electrons to these empty states.

Impurity band conduction had been realized for some time but it was Fritzsche[105] who first distinguished three types of conduction mechanisms each with a unique energy denoted as ε_1, ε_2 and ε_3. ε_1 is the ionization energy of the donor state and is the same as that described by E_d. ε_1 is present at concentrations with $N_D < 10^{18}cm^{-3}$ (as demonstrated by Jones and Woods[98]) and decreases as N_D increases thus causing the lowering of ε_1 by an assortment of possible effects as described at the beginning of this section. It is generally accepted that ε_2 is the energy needed to transfer an electron from an occupied to another *occupied* donor state with the exchange of an absorbed or an emitted phonon in the process to conserve energy. ε_2 is important in a region where $2x10^{16} < N_D < 2x10^{17}$ cm^{-3} (Ref. 98) and as seen from Table IV, the results from this study fit this region. However, ε_2 conductivity is typically seen in crystals with high impurity concentrations and low compensation[84] whereas concentrations in Table IV are moderately high , and the compensation is very high. Furthermore, Jones and Woods[98] find an energy to 7 meV for ε_2 conductivity in bulk ZnSe. In general, $\varepsilon_1 > \varepsilon_2 > \varepsilon_3$ which implies (after taking into consideration the results of Jones and Woods) that the low energies observed in the SPVT

samples are due to conduction in the ε_3 band. Figure 29 illustrates a diagram showing the density of states of the impurity bands as function of the energies mentioned above relative to the conduction band edge. ε_F represents the position of the Fermi energy when a material is compensated. For a compensated semiconductor, the Fermi level lies in the lower band, and conduction proceeds via hopping with an activation energy ε_3. In other words, the electron tunnels through neighboring donor levels within the ε_3 band with the cooperation of phonons. The calculated concentration at which ε_3 is seen, occurs at $N_D < 10^{16}$ cm^{-3}.

It was mentioned above that hopping can occur in the absence of compensation as long as the donor wave function overlap is quite strong. Such an overlap will take place when N_D reaches a critical concentration, n_c.[106] At this stage, a different type of conductivity originates and the electrons behave like a degenerate electron gas. This is termed as metallic impurity conduction—analogous to the electronic conductivity in metals. The transition for which the conductivity goes from metallic to non-metallic is called the metal-non-metal (MNM) transition. It is generally observed that impurity conduction occurs for concentrations on the insulator side of MNM for which the material is required to be compensated. The total concentration of impurities at the MNM transition (i.e., n_c) has been estimated as[106]

$$n_c^{1/3} a_B^* \approx 0.25 \tag{85}$$

For impurities in ZnSe, $n_c \approx 6 \times 10^{17}$ cm^{-3}. The concentrations shown in Table IV are below n_c. Experiments show that as $N_D + N_A$ approaches the MNM transition, ε_2 and ε_3 begin to go to zero. However, according to a phenomenological expression developed by Debye and Conwell,[109] the ionization energy, E, as a function of N_D^+ follows

$$E = E_o - \alpha \left(N_D^+\right)^{1/3} \tag{86}$$

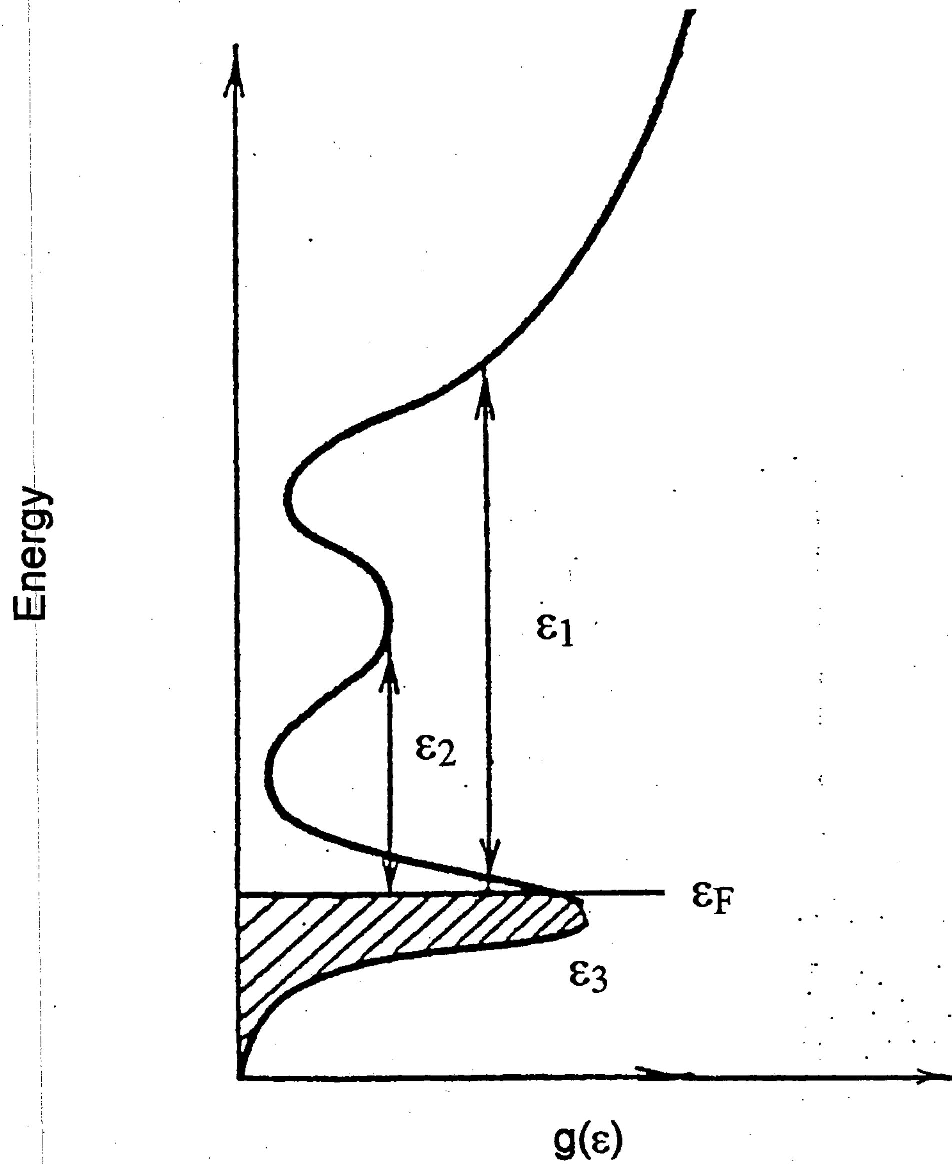

Figure 29. Schematic energy level diagram showing the density of states as a function of energy. The energies of the ε_2 and ε_3 impurity bands are shown relative to the conduction band. ε_1 is the ionization energy of the donor.

where E_o is the value for E as $N_D \rightarrow 0$, and α is a proportionality parameter. Fitting Eq. (86) to the data points in Fig. 30 gives $E_o = 8.92$ meV and $\alpha = 1.769 \times 10^{-5}$ meV cm. When E (here now ε_3) reaches zero, N_D is approximately 1.25×10^{17} cm^{-3}. This means that ε_3 conductivity will be similar to that of a metal with zero activation energy for hopping. It is interesting to note that ε_3 does not reach the effective-mass donor binding energy of approximately 29 meV for ZnSe when N_D goes to zero as might be expected.

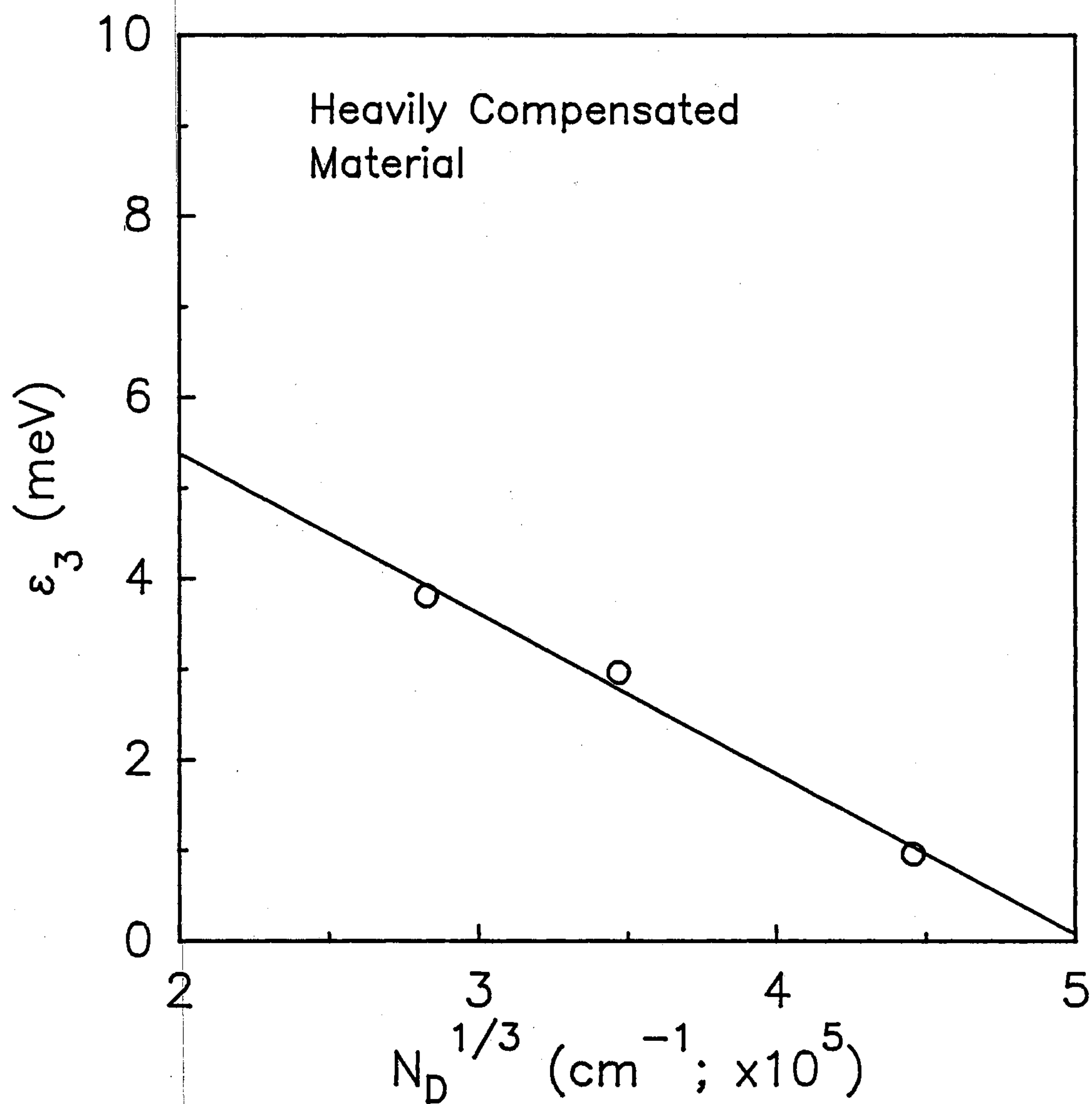

Figure 30. Plot of ε_3 versus $(N_D)^{1/3}$ from the values in Table IV. The concentration of N_D for which $\varepsilon_3 = 0$ is 1.25×10^{17} cm^{-3}.

CHAPTER IV

SUMMARY AND CONCLUSIONS

An extensive study dealing with PL and Hall effect analysis was achieved for a variety of as-grown and Zn-extracted, SPVT ZnSe samples in a temperature range from 4.2 K to room temperature. Although not explicitly stated in the thesis, this work can be classified in three parts: Crystal quality comparison from spectra, optical and electrical characterization of shallow-level defects.

Comparison between PL spectra show a progression in crystal quality from melt-grown to as-grown SPVT to Zn-Extracted SPVT material (refer to Figs. 6-8). Characteristic of the melt-grown sample is the strong DAP emission with a zero-phonon line at 2.6813 eV which is associated with a Na_{Zn} acceptor and a donor, believed to be Al_{Zn}, as suggested by Merz *et al.*[6] from luminescence work. Weak exciton emission is also observed along with the deep level Cu_g and Cu_r emissions, and as noted before, these features together with the intense DAP emission line makes the crystals semi-insulating, and is indicative of highly compensated material. With improvements on crystal preparation, EP can fine-tune the quality of bulk material by the SPVT technique. This shows in the PL spectrum which is comprised of strong exciton emission with I_1^d (at 2.7827 eV) dominating the entire spectrum and with weak Cu_g and Cu_r emissions along with SA emission also present. It is not certain whether I_1^d is an ABE due to Cu or V_{Zn}, although Isshiki *et al.*[29] suggest that I_1^d is due to V_{Zn}. To date efforts to dope the crystal during growth in order to promote n-type conductivity have proved unsuccessful. However, post-growth Zn-extraction techniques have produced samples of low resistivity (as low as 3.82 Ω cm) without compromising crystal quality. These samples display

strong exciton emission (with I_1^d and associated deep Cu or V_{Zn} levels absent) with I_x dominant at 2.7950 eV, and with weak DAP luminescence which are properties of a sample with a low concentration of defects. PL evidence from this latter class of specimens makes the idea of a ZnSe substrate more appealing.

Several PL techniques were employed to study the thermal, excitation power and stress behavior of the exciton and edge emission regions. Quenching of all bound exciton lines first seems to result in the thermally-assisted generation of FEs as a consequence of the liberation of FEs from associated defects followed by the dissociation of FEs which gave a binding energy of 20.2 meV, with the band gap subsequently calculated as 2.8225 eV at 12 K. With increasing temperature FE, I_2, I_x and I_V all merge to form a single peak with a FWHM exhibiting a linear temperature dependence from 150 to 225 K. With further temperature increase, the linear temperature dependence of FWHM changed from 225 K to room temperature and acquired a steeper slope as a result of perhaps the h-D^o transition coming in. Similar results have only shown one value for the slope of FWHM as demonstrated by Shirakawa and Kukimoto[47], and by Zheng and Allen.[56] The room temperature emission appears to originate from an h-D^o transition with a relatively deep donor at 38 meV. Quenching studies by Taguchi and Yao[57] reveal a donor state at 36 meV—possibly due to a V_{Se} (maybe in its singly charged state) or a V_{Se}-related complex defect as suggested by them. The variation of the h-D^o peak energy with temperature does not closely follow the band gap which may be due to the nature of the deep donor involved in such a transition.

Quenching of the edge emission showed that the donor state at 18.5 meV involved in DAP gave an anomalous low activation energy of 6 meV at low temperatures and is thought to be due to the thermal release of electrons in the conduction band with a temperature dependent capture cross of the donor.[27,53] As the DAP emission quenched, the e-A^o transition is seen to increase and then decreases with an activation energy of E_A=114 meV corresponding to the thermal release of holes from the Li acceptor state (at

E_A) to the valence band. The existence of such a state is verified with use of Eagles'[51] formula which yields a value of approximately 114 meV after fitting the peak position of e-A^o versus temperature.

Studies of the excitation power dependence on the exciton and edge emission intensities illustrate that all slopes for the former case are linear with laser power and are slightly greater than 1, whereas for the latter case, the DAP emission is linear and the e-A^o line curved with this latter emission apparently showing two power regimes. The fact that the PL data (see Fig. 11) show that the intensities of the exciton and edge emissions are comparable with each other at the lowest laser power may indicate that all emissions occur in the high power regime. The rate equations predict that the edge emission intensity should be greater than the exciton emission intensity for the emissions to fall in the low power category. The higher value of the two slopes of e-A^o could mean that the low power regime is close to the low power limit (i.e. 2.88 μW) attained in the excitation power study. All values of the slopes for the luminescence peaks of interest to this work agreed with the rate equation model except for the DAP emission line as noted in Table II. The disagreement is shown to be due to the disregard of the excitation power dependence on the transition rate, *i*, but then after considering this term the low value of the slope was corrected and gave 0.72 compared to 0.74 obtained experimentally. At the lowest excitation power, the presence of a peak at 2.7049 eV in the PL spectrum was clearly seen. This was assigned to the first excited state of the shallow donor at 18.5 meV taking part in the DAP1 emission (labeled $DAP1_{n=2}$) since the peak energy is 13.88 meV (= 18.5 meV - 18.5 meV/n^2, for n = 2) higher than ground-state emission energy of DAP1 at 2.6908 eV. It has been suggested that the 2.7049 eV-peak is due to the R-series DAP luminescence involving Li_i (E_d = 17 meV) as the shallow donor and Li_{Zn} as the shallow acceptor.[110] However, the results from this study along with results reported elsewhere indicate that the 2.7049 eV line does not seem to involve a Li_i from the so-called R-series DAP transition.[52] It has also been suggested that the I_x line is the I_3 line which is an

latter line seen in unstrained bulk material.[6,7,45] Furthermore, the emission line at 2.7701 eV is typically attributed to FE-1LO because it is approximately 31.1 meV below the FE emission peak. Analysis of the thermal quenching and the excitation power-dependent data reveal that I_x is due to a neutral DBE, and that I_V is not FE-1LO but is exciton-related—perhaps dealing with a Se-related defect.[57]

Uniaxial stress analysis of the exciton emission lines was performed on several Zn-extracted samples. The PL spectrum of a stressed Zn-extracted sample showed a collection of peaks with one or more of the various emission energies observed in a number of reports on ZnSe/GaAs heteroepitaxial materials. It is interesting to note that any two of the three lines: FE^{LP}, FE^{hh} and FE^{lh} observed here have been reported as FE^{hh} and FE^{lh}, as FE^{UP} and FE^{LP},and as FE^{LP} and FE for samples possibly illuminated in various ways. Our results imply that the emission lines in strained material are strongly polarization-dependent and can be easily overlooked when exciting with unpolarized light. Stress dependence on I_x suggested that this line is due to an exciton bound to a deep neutral donor level—possibly the same donor level responsible for the h-D^o transition. The assignment of I_2^{Ga} and I_x in Fig. 13 is in accordance with the stress results from this study and the published literature and are not the I_2^{hh} and I_2^{lh} components of I_2. The calculated linear hydrostatic and shear deformation potential constants for the band gap in SPVT material resulted in values of -1.8 eV and -0.37 eV, respectively. These values are smaller than those found in the literature (see Table III), and may indicate that the conduction band does not shift as fast as that observed in other samples reported elsewhere.[82] Converting the hydrostatic deformation potential constant obtained from the fit of the FE^{lh} curve to pressure coefficient (i.e., 7.7 meV/kbar) showed very good agreement with the value for the band gap of 7.3 meV/kbar as measured by Shan *et al.*[78] in SPVT ZnSe. PL measurements in some samples show a residual built-in strain in agreement with recent crystal growth results from Eagle-Picher laboratories on strain due

to long range defects. In fact, they believe that the crystallinity of the SPVT materials is actually improving due to the presence of fewer defects to relieve the strain.

Analysis of the free carrier concentration as a function of temperature for three Zn-dipped SPVT ZnSe specimens with p = 4.86, 6.6 and 6.9 Ω cm clearly displayed some interesting features. Impurity concentrations ranged from 2.25 to 8.85 X 10^{16} cm^{-3} for N_D and 2.06 to 8.71 X 10^{16} cm^{-3} for N_A with compensation ratios from 92 to 98.4% which indicate that the samples are highly compensated. Free carrier concentrations were in the order of 10^{15} cm^{-3} and gradually decreased as the resistivity and the compensation ratio increased, and the calculated free carrier concentration agreed well with the measured values. Of particular interest are the unusually small values of the binding energies which decreased as the impurity concentration increased. Several mechanisms for reducing the activation energy (ε_1) have been proposed:[104] (i) Polarization effects due to neutral donors, (ii) screening between the bound electron and the donor level due to conduction electrons, (iii) electrostatic attraction between conduction electrons and ionized donors and (iv) conduction band tailing effects of which none had an appreciable contribution to ε_1. However, impurity band conduction in the ε_3-band with the electron moving from an empty to a filled donor state via thermally-assisted tunneling and with a characteristic activation energy, ε_3, accounted for the data satisfactorily. The Hall mobility data was described in terms of scattering by impurity pairs, ionized and neutral impurities; and by polar optical phonons and acoustic phonons due to the deformation potential. The concentration of ionized impurities was found to vary between 10^{13} and 10^{16} cm^{-3}, and the concentration of pairs was in the range between 10^{15} and 10^{16} cm^{-3}. The concentration of neutral impurities was near 10^{16} cm^{-3} and high mobilities slightly above 10^4 cm^2/Vs were obtained at 20 K. This latter value is among the highest ever reported in the literature.

The major thrust of this project is to eventually develop a ZnSe substrate for the deposition of epitaxial layers. Presently, the center of attention has been directed on producing n-type wafers because these can be grown more readily than p-type, and n-type

conductivity can be promoted with less difficulty than p-type conductivity. Despite the difficulty in producing p-type bulk material, p-type epitaxial layers can now be grown relatively easy with high hole concentrations by means of MBE, for example, and radical doping techniques.[21] Once a reliable wafer is produced for homoepitaxy, a blue emitter based on a p-n junction will be developed consisting of epitaxial p- and n-type layers on an n-type substrate. This would be a milestone for an emitter operating at low temperatures but the biggest challenge would be to achieve efficient operation at room temperature. The availability of a practical device emitting in the blue is currently lacking but the extensive use of GaAs wafers puts them in the lead over ZnSe for potentially attaining a useful device.

Before an SPVT (or any other ZnSe substrate for that matter) ZnSe homostructure material can be fully developed and integrated into a practical device, some problems must be overcome to achieve such a goal. At present, extensive doping studies have not been performed to its fullest potential in order to get successful impurity incorporation (mainly donor incorporation), and subsequently, high impurity and free carrier concentrations despite the relatively high, unintentional impurity concentration observed from Hall effect studies. A clear knowledge on the chemical identity of defects is lacking for SPVT material—as is the case in the open literature for other ZnSe crystals—which is imperative so that one can understand and control the effects of doping on optical and electrical properties. Experiments which can be done to help attain such knowledge are: (1) excitation power dependence of the h-D^{o} transition at room temperature to determine whether the slope is less than or greater than 1, (2) selective excitation and excitation spectroscopy of PL to monitor resonance states, (3) time-resolved spectroscopy to separate processes with different time evolution in the exciton and edge emission regions, and to measure lifetimes of transitions, (4) low temperature DLTS to see if the relatively deep donor level at E_c - 38 meV really exists, and of course, (5) doping studies. After this, the next task is to make a p-n junction on the wafer for immediate testing of blue light.

REFERENCES

1. Shrader, R.E., S. Lasof, and H.W. Leverenz, *Solid Luminescent Materials*, Cornell University Symposium (Wiley, New York, 1946), p. 215.

2. Bube, R.H., and E.L. Lind, Phys. Rev. **110**, 1040 (1958).

3. Marple, D.T.F., B. Segall, and M. Aven, Bull. Am. Phys. Soc. **6**, 19 (1961).

4. Aven, M. and H.H. Woodbury, Appl. Phys. Lett. 1, 53 (1962).

5. Henry, C.H. and K. Nassau, Phys. Rev. B**2**, 997 (1970).

6. Merz, J.L., H. Kukimoto, K. Nassau, and J.W. Shiever, Phys. Rev. **6**, 545 (1972).

7. Merz, J.L., K. Nassau, and J.W. Shiever, Phys Rev. **8**, 1444 (1973).

8. Yao, T., Y. Makita, and S. Maekawa, Appl. Phys. Lett. **35**, 97 (1979).

9. Bhargava, R.N., J. Cryst. Growth **86**, 873 (1988).

10. Laks, D.B., C.G. Van de Walle, G.F. Neumard, and S.T. Pantelides, Phys. Rev. Lett. **66**, 648 (1991).

11. Neumark, G.F., J. Appl. Phys. **51**, 3383 (1980).

12. Neumark, G.F., Phys. Rev. Lett. **62**, 1800 (1989).

13. Park, Y.S., and B.K. Shin, in *Electoluminescence* ed by J.I. Pankove, *Topics in Applied Physics* (Springer, Berlin, 1977), V.7, p. 133.

14. Haase, M.A., J. Qiu, J.M. DePuydt, and H. Cheng, Appl. Phys. Lett. **59**, 1272 (1991).

15. Jean, H., J. Ding, W. Patterson, A. Nurmikko, W. Xie, D. Grillo, M. Kobayashi and R.L. Gunshor, Appl. Phys. Lett. **59**, 3619 (1191).

16. Jean, H., H. Ding, A.V. Nurmikko, H. Luo, N. Samarth and J.K. Furdyna, Appl. Phys. Lett. **59**, 1293 (1991).

17. Nurmikko, A.V., R.L. Gunshor and M. Kobayashi, J. Cryst. Growth **117**, 432 (1992).

18. See for example, Chung, C., F. Jain and G. Drake, J. Cryst. Growth **117**, 1062 (1992).

19. Williams, J.O., A.C. Wright and H.M. Yates, J. Cryst. Growth 117, 441 (1992).

20. Cantwell, G., W.C. Harsh, H.L. Cotal, B.G. Markey, S.W.S. McKeever, and J.E. Thomas, J. Appl. Phys. **71**, 2931 (1992).

21. Sokolov, V.I., T.P. Sukova, M.V. Chukichev, and Vu Zoan M'en, Sov. Phys. Solid State **26**, 2215 (1984).

22. Sturge, M.D., in *Excitons*, ed. E.I. Rashba and M.D. Sturge (North-Holland, Amsterdam, 1982) Vol. 2, p. 1.

23. Adachi, S. and T. Taguchi, Phys. Rev. B 43, 9569 (1991).

24. Segall, B. and D.T.F. Marple, *Physics and Chemistry of II-VI Compounds*, ed. by M. Aven and J.S. Prener (North-Holland, Amsterdam, 1967), p. 319.

25. Sermage, B., and G. Fishman, Phys. Rev. **B23**, 5107 (1981).

26. Belincourt, I., H. Jaffe, and L.R. Shiazawa, Phys. Rev. **129**, 1009 (1963).

27. Dean, P.J. and J.L. Merz, Phys. Rev. **178**, 1310 (1969).

28. Shibata, N., A. Ohki, S. Zembutsu, and A. Kutsui, Jpn. J. appl. Phys.**27**, L441 (1988).

29. Isshiki, M., T. Kyotani, and K. Masumoto, Phys. Rev. **B36**, 2568 (1987).

30. Shahzad, Khalid, Diego J. Olego, and David A. Cammack, Phys. Rev. **B39**, 13016 (1989).

31. Bebb, H.B., and E.W. Williams, *Semiconductors and Semimetals*, ed. by R.K. Willardson and A.C. Beers (Academic, New York, 1972), V.8, p.181.

32. Sermage, B., and G. Fishman, Phys. Rev. **B23**, 5107 (1981).

33. Watts, R.K., *Point Defects in Crystals* (Wiley, New York, 1977), p. 235.

34. Neumark, G.F. and S.P. Herko, J. Cryst. Growth **59**, 189 (1982).

35. Haase, M.A., H. Cheng, J.M. DePuydt, and J.E. Potts, J. Appl. Phys. **67**, 448 (1990).

36. Ohkawa, K. T. Karasawa, and T. Mitsuyu, Jap. J. Appl. Phys. **30**, L152 (1991).

37. Harrison, W.A., *Electronic Structure and the Properties of Solids, The Physics of the Chemical Bond* (Dover, New York, 1989), p. 61.

38. See for example Fig. 5, H.L. Cotal, Master's Thesis (OSU, 1990).

39. Merz, J.L., K. Nassau, and J.W. Shiever, Phys. Rev. B 8, 1444 (1973).

40. Robbins, O.J., P.J. Dean, P.E. Simmonds, and H. Tews, *Deep Centers in Semiconductors*, ed. by S.T. Pantelides (Gordon and Breach, New York, 1986), p. 717.

41. Mitsuyu, T., K. Ohkawa and O. Yamazaki, Appl. Phys. Lett. **49**, 1348 (1986).

42. Dean, P.J., Phys. Stat. Sol. (a) **81**, 625 (1984).

43. Langer, D.W., R.N. Euwema, K. Era and T. Koda, Phys. Rev. **B 2**, 4005 (1970).

44. Schmidt, T., G. Daniel and K. Lischka, J. Cryst. Growth **117**, 748 (1992).

45. See for example, M. Vaziri, R. Reifenberger, R.L. Gunshor, L.A. Kolodziejski, S. Venkatesan, and R.F. Pierret, J. Vac. Sci. Technol. **B7**, 253 (1989); J. Gutowski, N. Presser, and G. Kudlek, Phys. Stat. Sol. (a) **120**, 11 (1990).

46. Gribkouskii, V.P., L.G. Zimin, S.V. Gaponenko, I.E. Malinovskii, P.I. Kuzetsov, and G.G. Yakusheheva, Phys. Stat. Sol. (b) **158**, 359 (1990).

47. Shirakawa, Y. and H. Kukimoto, J. Appl. Phys. **51**, 2014 (1980).

48. Casey, H.C., and M.B. Panish, *Heterostructure Lasers, Part B*, (Academic, New York, 1978), p.1.

49. Varshni, Y.P., Physica **34**, 149 (1967).

50. Manoogian, A., and J.C. Wooley, Can. J. Phys. **62**, 285 (1984).

51. Eagles, D.M., J. Phys. Chem. Solids **16**, 76 (1960).

52. Zhang, Y., B.J. Skromme, and H. Cheng, Phys. Rev. **B47**, 2107 (1993).

53. Maeda, K., J. Phys. Chem. Solids **26**, 595 (1965).

54. Pankove, J.I., *Optical Processes in Semiconductors* (Dover, New York, 1971).

55. Hite, G.E., D.T.F. Marple, M. Aven, and B. Segall, Phys. Rev. **156**, 850 (1967).

56. Zheng, Jia Zhen, and J.W. Allen, J. Appl. Phys. **67**, 2060 (1990).

57. Taguchi, T., and T. Yao, J. Appl. Phys. **56**, 3002 (1984).

58. Taguchi, T., J. Shirafuji and Y. Inuishi, Phys. Status Sol. (b) **68**, 727 (1975).

59. Lee, B.H., J. Appl. Phys. **41**, 2984 (1970).

60. Laude, L.D., F. Pollak, and M. Cardona, Phys. Rev. **B3**, 2623 (1971).

61. Pollak, F.H., Surf. Sci. **37**, 863 (1973).

62. Chandrasekhar, M., and F. Pollak, Phys. Rev. **B15**, 2127 (1977).

63. Bir, G.L., E.I. Butikov, and G.E. Pikus, J. Phys. Chem. Solids **24**, 1467 (1963).

64. Thomas, D.G., J. Appl. Phys. Suppl. **32**, 2298 (1961).

65. Cho, K., *Excitons: Topics in Current Physics* (Springer, Berlin, 1979), V. 14.

66. Bir, G.L., and G.E. Pikus, *Symmetry and Strained-Induced Effects in Semiconductors* (Wiley, New York, 1979).

67. Bhargava, R.N., and M.I. Nathan, Phys. Rev. **161**, 695 (1967).

68. Grapis, K.P., and K.F. Jensen, J. Cryst. Growth **101**, 111 (1990).

69. Potts, J.E., H. Cheng, S. Mohapatra, and T.L. Smith, J. Appl. Phys. **61**, 333 (1987).

70. Tokura, Y., T. Koda, I. Hirabayashi, and S. Nakada, J. Phys. Soc. Jpn. **50**, 145 (1981).

71. Sermage, B., and G. Fishman, Phys. Rev. B **23**, 5107 (1981).

72. Lee, J., E.S. Koteles, M.O. Vassell and J.P. Salerno, J. Lumin. **34**, 63 (1985).

73. Saito, H., M. Ohishi, A. Watanabe, and K. Ohmori, J. Cryst. Growth **101**, 727 (1990).

74. Bailey, P.T., Phys. Rev **B1**, 588 (1970).

75. Mar, H.A., and R.M. Park, J. Appl. Phys. **60**, 1229 (1986).

76. Maung, N., and J.O. Williams, J. Cryst. Growth **86**, 629 (1988).

77. Park, R.M., H.A. Mar, and N.M. Salansky, Apply Phys. Lett. **46**, 386 (1985).

78. Shan, W., J.M. Hays, X.H. Yang, and J.J. Song, Appl. Phys. Lett. **60**, 736 (1992).

79. Tajima, M., Appl. Phys. Lett. **32**, 719 (1978).

80. Mott, N.F. and W.D. Twose, *Advances in Physics*, ed. by B.H. Flowers (Taylor and Francis, London, 1961), Vol. 10, p. 107.

81. Koteles, E.S., in *Excitons*, ed. by E.I. Rashba and M.D. Sturge (North-Holland, Amsterdam, 1982) V.2, p. 83.

82. Van de Walle, C.G., Phys. Rev. **39**, 1871 (1989).

83. Tachman, J.A., S. Kim, Z. Sui, and I.P. Herman, Phys. Rev. **46**, 1337, (1992).

84. Shklovskii, B.I. and A.L. Efros, *Electronic Properties of Doped Semiconductors* (Springer-Verlag, Berlin, 1984).

85. Rode, D.L., *Semiconductors and Semimetals*, ed. by R.K. Willardson and Albert C. Beer (Academic, New York, 1975), Vol. 10, p. 1.

86. Ruda, H.E., J. Appl. Phys. **59**, 1220 (1986).

87. Briot, O., N. Briot, T. Cloitre, R. Sauvezon, and R.L. Aulombard, Semicond. Sci. Technol. **6**, A24 (1991).

88. Aven, M. and B. Segall, Phys. Rev. **130**, 81 (1963).

89. Boer, K.W., *Survey of Semiconductor Physics* (Van Nostrand, New York, 1990).

90. Brooks, H., *Advances in Electronics and Election Physics*, ed. by L. Marton (Academic, New York, 1955), Vol. 7, p. 87.

91. Canwell, E., and V.F. Weisskopf, Phys, Rev. 77, 388 (1950).

92. Boardman, A. D., Proc. Phys. Soc. **85**, 141 (1965).

93. Erginsoy, C., Phys. Rev. **79**, 1013 (1950).

94. Howarth, D.J., and E.H. Sondheimer, Proc. Roy. Soc. **A219**, 53 (1953).

95. Ziman, J.M., *Electrons and Phonons* (Oxford University, Amen House, London, 1960), p. 421.

96. Yao, T., Y. Okada, S. Matsui, K. Ishida and I. Fujimoto, J. Cryst. Growth **81**, 518 (1987).

97. Stutius, W., J. Appl. Phys. **53**, 284 (1982).

98. Jones, G. and J. Woods, J. Phys. D: Appl. Phys. **9**, 799 (1976).

99. Sze, S.M., *Physics of Semiconductor Devices* (Wiley, New York, 1981).

100. Aven, M.J., J. Appl. Phys. **42**, 1204 (1971).

101. Yao, T., J. Cryst. Growth **72**, 31 (1985).

102. Boone, J.L., and G. Cantwell, J. Appl. Phys. **57**, 1171 (1985).

103. Markey, B., Ph.D. Thesis, (1993).

104. Lee, T.F., and T.C. McGill, J. Appl. Phys. **46**, 373 (1975).

105. Fritzche, H., Phys. Rev. **125**, 1552 (1962).

106. Mott, N.F., and W.D. Twose, *Advances in Physics*, ed. by B.H. Flowers (Taylor & Francis, London, 1961), V. 10, p. 107.

107. Mott, N.F. and E.A. Davis, *Electronic Processes in Non-Crystalline Materials* (Clarendon Press, Oxford, 1971), p. 152.

108. Jackson, J.D., *Classical Electrodynamics* (Wiley, New York, 1975), p. 136.

109. Debye, P.D., and E.M. Conwell, Phys. Rev. **93**, 693 (1954).

110. Neumark, Phys. Rev. B **37**, 4778 (1988).

111. Kohn, W., *Solic State Physics*, ed. by F. Seitz and D. Turnbull (Academic Press, New York, 1957), V. 5, p. 258.

112. Chelikowsky, J.R., and M.L. Cohen Phys. Rev. **B14**, 556 (1976).

2

VITA

Hector Luis Cotal

Candidate for the Degree of

Doctor of Philosophy

Thesis: OPTICAL AND ELECTRICAL CHARACTERIZATION OF SEEDED PHYSICAL VAPOR TRANSPORT ZINC SELENIDE

Major Field: Physics

Biographical:

Personal Data: Born in Aguadilla, Puerto Rico, February 12, 1959, the son of Pete Cotal and Elba Zapata. Married to Sharon Ann Isbell on June 21, 1986. Father of two children.

Education: Graduated from Dr. Pila High School, Ponce, Puerto Rico, in May 1979; received the Bachelor of Science degree in Physics from Oklahoma State University in July, 1986; completed the requirements for the Master of Science degree at Oklahoma State University in July, 1990; fulfilled the requirements for the Doctor of Philosophy degree at Oklahoma State University in July, 1993.

Professional Experience: Graduate Teaching Assistant, Oklahoma State University, August, 1987 to May, 1988; Graduate Research Assistant, Oklahoma State University, June, 1988 to present; Member of the American Physical Society and the Optical Society of America.